University of Arkansas, Fayetteville
ScholarWorks@UARK

Theses and Dissertations

12-2014

GeSn Light-Emitting Devices

Yiyin Zhou
University of Arkansas, Fayetteville

Follow this and additional works at: http://scholarworks.uark.edu/etd

Part of the Electrical and Electronics Commons, and the Semiconductor and Optical Materials Commons

Recommended Citation
Zhou, Yiyin, "GeSn Light-Emitting Devices" (2014). *Theses and Dissertations*. 2055.
http://scholarworks.uark.edu/etd/2055

This Thesis is brought to you for free and open access by ScholarWorks@UARK. It has been accepted for inclusion in Theses and Dissertations by an authorized administrator of ScholarWorks@UARK. For more information, please contact scholar@uark.edu, ccmiddle@uark.edu.

GeSn Light-Emitting Devices

GeSn Light-Emitting Devices

A thesis submitted in partial fulfillment
of the requirements for the degree of
Master of Science in Microelectronics-Photonics

By

Yiyin Zhou
Tianjin University of Technology
Bachelor of Science in Applied Physics, 2011
University of Arkansas – Fort Smith
Bachelor of Science in Organizational Leadership, 2012

December 2014
University of Arkansas

This thesis is approved for recommendation to the Graduate Council.

Dr. Shui-Qing Yu Thesis Director	Dr. Hameed Naseem Committee Member
Dr. Gregory Salamo Committee Member	Prof. Ken Vickers Ex-Officio Member

The following signatories attest that all software used in this thesis was legally licensed for use by Yiyin Zhou for research purposes and publication.

______________________________	______________________________
Mr. Yiyin Zhou, Student	Dr. Shui-Qing Yu, Thesis Director

This thesis was submitted to http://www.turnitin.com for plagiarism review by the TurnItIn company's software. The signatories have examined the report on this thesis that was returned by TurnItIn and attest that, in their opinion, the items highlighted by the software are incidental to common usage and are not plagiarized material.

______________________________	______________________________
Dr. Rick Wise, Program Director	Dr. Shui-Qing Yu, Thesis Director

Abstract

Silicon based optoelectronic devices have been investigated for decades [1]–[10]. However, due to the indirect band gap nature of Si and Ge, developing of efficient light-emitting source on Si is still a challenging topic. GeSn based optoelectronic devices have the great potential to overcome this deficiency for several reasons. By adding more fraction of Sn into Ge, GeSn band gap could be reduced. The narrowed band gap could be developed for near to mid infrared applications. The alloy can even become the direct band gap material with a large Sn composition (beyond 8%). This feature could enhance the light emission from the direct band gap transition. Due to the simple process of GeSn device fabrication, the cost of infrared optoelectronic devices could be reduced. Furthermore, the compatibility of GeSn based devices on complementary metal on semiconductor (CMOS) process enables further opportunities for Si photonic integrated circuits.

This thesis discusses the fabrication and characterization of GeSn optoelectronic devices to prove the great potential of this material. The discussion mainly covers the double hetrostructure (DHS) LED, following with an extension study on photodetector. The grown material was characterized and proved to be high quality using X-Ray diffraction (XRD) and photoluminescence (PL). The LED fabrication process and results are described in detail. Surface emitting LED characterization was studied using the current-voltage (I-V) measurement, electroluminescence (EL), as well as optical power. EL spectra of 6%, 8%, 9%, and 10% Sn LED was measured. Emission due to the direct band was observed. The wavelength of the EL spectrum peak of 2348 nm was achieved for measuring 10% Sn LED. Optical power with an average of 0.2 mW was measured under 100 mA current injection. Surface emitting LED design was developed into three generations serving for different research purposes. Edge emitting LED was fabricated and characterized with I-V and EL measurements. For light-detection, both

photoconductors and p-i-n photodiodes were characterized with I-V and the spectral response. The absorption spectral response was measured with different Sn composition devices, showing the extended detection range towards mid infrared. The characterizations of GeSn based optoelectronic devices in this thesis demonstrated the GeSn material is versatile and capable for optoelectronic devices.

Acknowledgements

First of all, I would like to express my sincere gratitude to my thesis adviser Prof. Shui-Qing Yu for his patience, motivation, support, and guidance. He has provided such an excellent opportunity for my master study. The guidance from Dr. Hameed Naseem was always helpful for me to understand the true nature of the problem. The expertise and experience of Dr. Gregory Salamo has enlighten my research direction.

I would like to thank Prof. Ken Vickers for his support on my academic study. He has created an excellent program, Microelectronics-Photonics, enable students to work collaboratively as a community. I have been benefiting from this program so much. I am also grateful to Dr. Rick Wise for his help on reviewing my thesis.

Special thanks to Dr. Wei Du for his continuous help on my research. He has guided and inspired me through the difficulties on the research. Thanks to Seyed Amir Ghetmiri for helping in measurements of PL and EL, Benjamin R. Conley for his guidance on Fourier transform infrared spectroscopy (FTIR) setup, Aboozar Moslec for his effort helping me on high resolution XRD (HRXRD), Dr. Liang Huang and Thach Pham for their help on the fabrication process, and all of my research group members for their wonderful team work and collaborative spirit.

I would like to thank all of the funding agencies in this work. This program is financially supported partially by the National Science Foundation under Grant No. EPS-1003970. Any opinions, findings, and conclusions or recommendations expressed in this material are those of the author and do not necessarily reflect the views of any of these funding agencies. Research possible through the use of the High Density Electronics Center at the University of Arkansas, Fayetteville campus. This work is also partially supported by the Arkansas Bioscience Institute, the Arktonics, LLC (Air Force SBIR, FA9550-14-C-0044, Dr. Gernot Pomrenke, Program

Manager) and the Defense Advanced Research Projects Agency (DARPA) (W911NF-13-1-0196, Dr. Dev Palmer, Program Manager).

Dedication

This thesis is dedicated to my dear parents. Their tremendous support and encouragement made all of these happened.

Table of Contents

Chapter 1: Introduction 1

1.1 Research Area 1

1.2 Problems and Objectives 7

1.3 Organization of Thesis 7

Chapter 2: Material Characterization 9

2.1 Introduction 9

2.2 X-ray Diffraction (XRD) 9

2.3 Photoluminescence (PL) 11

Chapter 3: Surface Emitting LEDs 17

3.1 Introduction 17

3.2 First Generation Device 17

3.3 Second Generation Device 38

3.4 Third Generation Device 43

Chapter 4: Edge-Emitting LEDs 46

4.1 Introduction 46

4.2 Device Fabrication 47

4.3 Device Characterization 50

Chapter 5: Light-Detection 55

5.1 Introduction 55

5.2 Device Fabrication 55

5.3 Device Characterization 56

Chapter 6: Conclusion and Future Work 62

References 65

Appendix A: Description of Research for Popular Publication 69

Appendix B: Executive Summary of Newly Created Intellectual Property 71

Appendix C: Potential Patent and Commercialization Aspects of Listed Intellectual Property Items 72
Appendix D: Broader Impact of Research 74
Appendix E: Microsoft Project for MS MicroEP Degree Plan 75
Appendix F: Identification of All Software Used in Research and Thesis Generation 76
Appendix G: All Publications Published, Submitted and Planned 77
Appendix H: First Generation Surface Emitting LED Fabrication Traveler 78

List of Figures

Figure 1: Statistics on GeSn and GeSn based LED publications.. 3

Figure 2: Schematic diagram of band structure for Si (left) and Ge (right). 5

Figure 3: $Ge_{1-x}Sn_x$ band gap energy as a function of Sn composition [41]. 6

Figure 4: Schematic diagram of XRD setup. 10

Figure 5: XRD 2theta-omega 2θ-ω scan for 6% and 8% Sn sample [17]. 11

Figure 6: Reciprocal space maps from (-2 -2 4) plane of $Ge_{1-x}Sn_x$ films with 6% (left) and 8% Sn (right) [17]. 11

Figure 7: Schematic diagram of PL setup. 12

Figure 8: Schematic diagram of PL mechanism in band structure with Sn composition of (a)3.2%, (b)8%, and (c)10%. 13

Figure 9: PL spectra for GeSn thin film with Sn composition of 0%, 3.2%, 8%, and 10% [16]. 14

Figure 10: PL spectra of Ge reference, DHS 6% Sn sample, and DHS 8% Sn. 15

Figure 11: Schematic diagram of cross section for the surface emitting LED. 17

Figure 12: Process flow of first generation LED fabrication. 18

Figure 13: (a) Dicing & cleaving wafer orientation, (b) and (c) wafer map for the sample cleaving. 19

Figure 14: Schematic diagram of sample structure before fabrication. 20

Figure 15: Schematic diagram of positive photolithography process. (a) Ultra violet (UV) light exposure (b) after development. 21

Figure 16: Schematic diagram of etched sample. 22

Figure 17: GeSn thin film etched mesa height (with initial photoresist thickness) as a function of etching time. 23

Figure 18: Ge/$Ge_{1-x}Sn_x$/Ge DHS etching rate in HCl:H_2O_2:H_2O=1:1:20 solution with various Sn composition. 23
Figure 19: Scanning electron microscope (SEM) image of the etching result from (a) chemical wet etching and (b) RIE. 24
Figure 20: (a) Positive photoresist, (b) metal deposited on positive photoresist, (c) negative photoresist, and (d) metal deposited on negative photoresist. 25
Figure 21: Schematic diagram of negative photolithography (left) and after development (right) 26
Figure 22: Schematic diagram of (left) metal deposition and (right) liftoff result. 26
Figure 23: (a) Schematic diagram of fabricated LED device, and (b) optical image of top view. 27
Figure 24: I-V measurement with various mesa sizes 29
Figure 25: I-V for 6% Sn and 8% Sn devices with 500 μm mesa at room temperature [17]. 29
Figure 26: Temperature dependent I-V for 8% Sn device with 500 μm mesa. 30
Figure 27: Fitting forward current for 8% Sn devices with 500 μm mesa. 31
Figure 28: Schematic diagram of current mechanism in p-i-n diode (a) BTB, TAT, and Shockley-Read-Hall recombination, and (b) diffusion, drift current, and radiative recombination. 31
Figure 29: Schematic diagram drawing of EL measurement setup. 33
Figure 30: EL spectra with various current injection 6% Sn 1st Generation LED [17]. 34
Figure 31: EL spectra with various current injection (a) 6% Sn; (b) 8% Sn composition [17]. 35
Figure 32: EL spectra of 9% and 10% Sn LEDs. 35
Figure 33: Spectra between PL and EL of 8% Sn sample. 37
Figure 34: Schematic diagram of optical power measurement. 37
Figure 35: Optical power of 6% and 8% 1st generation LED 38
Figure 36: Optical top image of second generation LED. 39

Figure 37: IV for 2nd generation 6% Sn LED. 40

Figure 38: IV for 2nd generation 8% Sn LED. 40

Figure 39: EL spectra of 6% Sn 2nd generation LED... 41

Figure 40: EL spectra of 8% Sn 2nd generation LED... 42

Figure 41: DC optical power for 8% Sn 2nd generation LED. 42

Figure 42: Optical image of bonded sample, top view. 43

Figure 43: EL spectra from 6% Sn LED with 1st and 3rd generations. 44

Figure 44: DC optical power for all fabricated LED devices. 45

Figure 45: Refractive index of GeSn layer along the ridge. 46

Figure 46: Calculated light profile for GeSn layer. 47

Figure 47: Process flow of edge-emitting LED fabrication. 49

Figure 48: Schematic diagram of lapping process 50

Figure 49: (a) Schematic diagram of cleaved n-i-p edge-emitting LED, and (b) SEM image. 50

Figure 50: I-V for 6% Sn edge-emitting LED. 51

Figure 51: I-V for 8% Sn edge-emitting LED. 51

Figure 52: EL spectra of 6% Sn edge-emitting LED. 52

Figure 53: EL spectra of 8% Sn edge-emitting LED. 53

Figure 54: EL spectra for 8% Sn edge-emitting LED with spike peaks. 54

Figure 55: (a) Schematic diagram of photoconductor, and (b) optical image of top view. 56

Figure 56: I-V for photoconductors with different Sn composition (2 mm mesa). 57

Figure 57: Band diagram of photoconductor operating under different electrical field direction.57

Figure 58: Spectral response of photoconductor with different Sn composition with different mesa size (length= 1 mm, 2 mm, and 0.5 mm). 58

Figure 59: Spectral response for photoconductors with different Sn compositions. 59

Figure 60: Temperature dependent spectral response for 7% Sn photoconductor. 60

Figure 61: Spectral response for p-i-n photodiode with different Sn composition....................... 61

Figure 62: Optical Image for LEDs bonded on a chip carrier. 70

List of Tables

Table I: Peak positions and FWHM of PL measurement. 16

Table II: Information of GeSn photoconductor layer structure. 55

Chapter 1: Introduction

1.1 Research Area

Germanium tin (GeSn) alloy, as a compound material in Group IV, has a large potential for optoelectronic devices [11], [12]. Initially, GeSn was used in high performance p-channel metal on semiconductor field effect transistor (pMOSFET) for logical applications [13]–[15]. The devices benefited from the tunable band gap and high mobility of the material. Adding more Sn into Ge would result in a band gap narrowing. The band gap of GeSn could be used for optoelectronic device applications in near and mid infrared range. Thereafter, GeSn with a Sn composition higher than 10% was turned out to be direct band gap material [16], which could improve the light emission efficiency of Group IV based optoelectronic devices. GeSn based LEDs [17]–[25] were demonstrated with direct band gap transition EL at room temperature. Besides, photodetectors with extended absorption range were also characterized [26]–[33]. From LEDs to photodetectors, GeSn based optoelectronic devices have several merits: tunable band gap by varying Sn composition, Group IV based direct band gap material, compatible with CMOS process, and low cost of device fabrication.

The band gap of GeSn alloy could be tuned by varying Sn composition. The band gap energy could range from 0.67 eV, which is has 0% Sn, i.e. Ge, to 0 eV, for Sn rich alloy, which is semimetal rather than semiconductor. This range of band gap energy enables multiple applications of band gap engineering. Confinment structures like DHS and quantum wells are desired for many the device designs. The great range of band gap energies could also lead to a wide light emission wavelength range for GeSn based light-emitting devices.

Furthermore, as Sn composition increase, the valence band of indirect band gap decreases slower than that of direct band gap. Consequently, the direct band gap could be attained with the

higher Sn composition. GeSn based direct band gap light-emitting devices could be light sources directly on Si, which can be widely used in Si photonics.

Due to the mature material growth technique of Group IV material, GeSn could be likely grown monolithically on Si substrate. In addition, due the low temperature (below 450 ˚C) growth, the whole GeSn based device process is fully CMOS compatible. This feature enables Gesn based optoelectronic devices integrating on conventional silicon based integrated circuits.

The low cost of fabrication process is also a great advantage for GeSn based optoelectronic devices. The low cost infrared light-emitting devices could be used for both optical gas sensing and communications.

As a result, GeSn based optoelectronic devices have attracted large attention in recent years. From recent years, investigations on GeSn alloys and related devices are prospering (shown in Figure 1. Several groups demonstrate the devices like photoconductor, photodiode, photodetector, and LEDs. These works started from primary simple material characterization and gradually developed into complicated device and analysis.

GeSn based LEDs have unique properties which enable a diversity of applications. Photon energy in the infrared range matches some of the bond energies between particles. Biological/chemical studies can use this feature to analysis the composition of the gases by looking for the “fingerprints absorption” from the absorption spectrum. Besides, infrared light could transmit through the atmosphere or certain medium with no optical loss. This virtue makes the infrared LEDs extensively applied for free space or fiber communications.

Biological/chemical studies are trying to analysis the bond between atoms component of gas. The absorption spectrum reflects the energy levels inside the molecule bonds. Bonds in molecules have distinct absorption energy. For example, substances such as methane [34] and carbon dioxide [35] have the absorption spectrum in the mid infrared range so that they could be

likely detected using infrared spectroscopy. Using this feature, chemical sensing could operate in a fast, inexpensive, remote way.

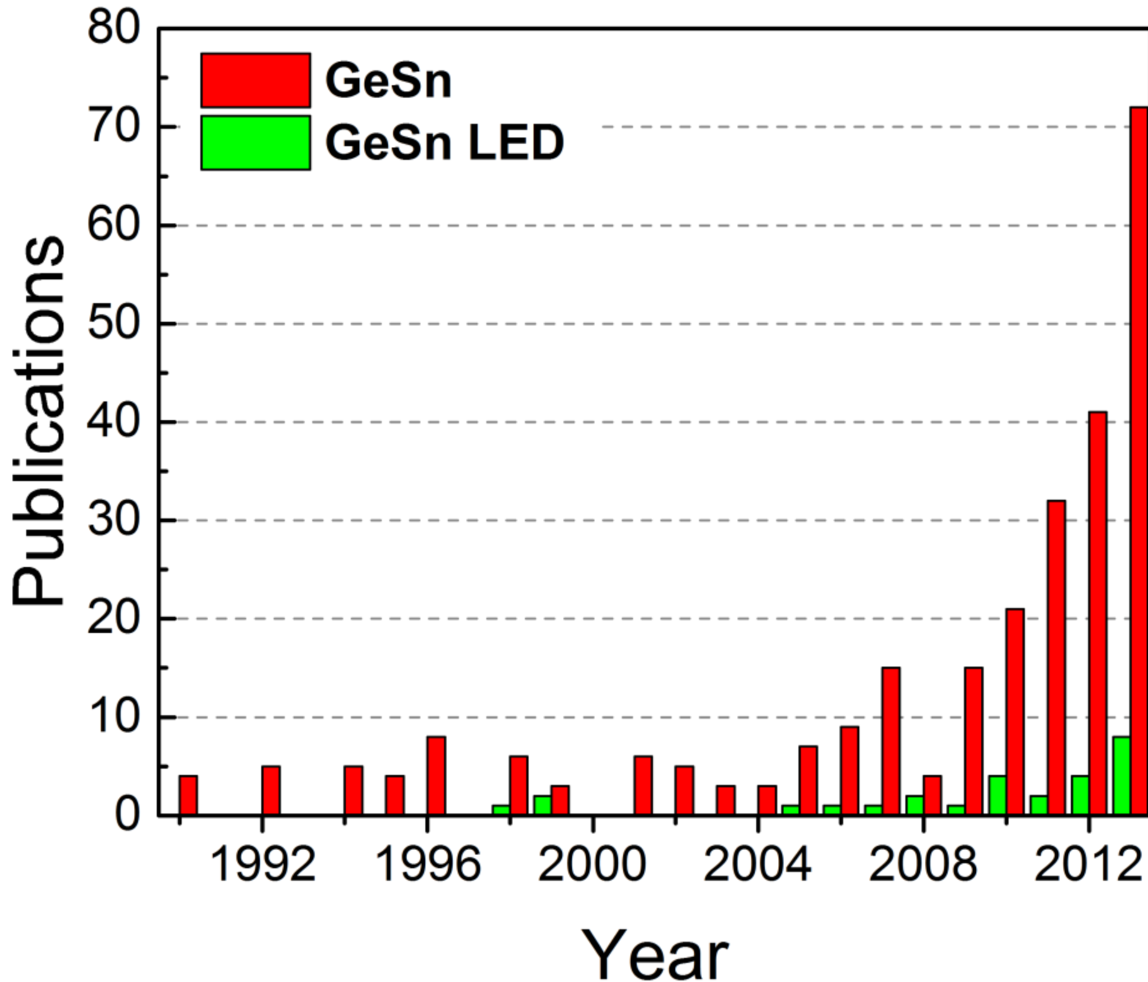

Figure 1: Statistics on GeSn and GeSn based LED publications.

Communication is necessary for every single individual nowadays. Electronic devices have enabled people share and exchange information worldwide within a blink. Enormous volume of data transfers among devices day by day. Telecommunications data rate increases exponentially every year. There are dramatic needs for the telecommunication on developing cost-effective, fast data transfer devices for communications. Previous efforts focused on shrinking the geometry of electronic IC. Moore's law predicts the growth of the electric

components in processors expands exponentially. This approach is now reaching its physical limit where the devices would no longer work properly in such a tiny scale. The difficulty of further developing communication capability has become more and more prominent.

Semiconductor optoelectronic devices have proceeded into a role which could solve this limit [36]. The transmitting rate of light is several orders faster than the electrons in the IC. In addition, techniques like wavelength-division multiplexing (WDM) enables multiple data transmit in various bands at the same time through a single channel (waveguide). This method dramatically increases the efficiency of data transfer. Furthermore, optoelectronic devices could shrink the size into nanoscale which compatible with the current IC technology. The combination of the optoelectronic devices and traditional IC could ingeniously improve the efficiency of data transfer.

Si is critical and fundamental for IC technology. And it is also an excellent material for passive devices such as waveguides and modulators [6][37]. Compare to recombination from the same k value (direct), the efficiency of radiative recombination is several orders lower than in an indirect band gap material according to the recombination theory [1]. Si and Ge are examples of indirect band gap materials. Their band structures are shown in Figure 2. Due to the indirect band gap, the light emission has few orders lower efficiency than III-V materials (mostly have direct band structure). Current optoelectronic IC technology compromise to find a way to bond the III-V devices onto the Si. Problems such as yield and uniformity of the bonding cause this process to be complicated and expensive. So there is a great demand for the efficient light source which could be grown directly on the Si substrate and fabricated in a cost effective manner.

Currently, there are several approaches on developing of laser devices, which is preferred as high efficient light-emitting devices. Si Raman laser was an optical pumping laser using the Raman Effect. Even though Si Raman laser could achieve low threshold, this type of laser

requires another pumping laser to provide the stimulus source. Ge/Si laser shows ability to have stimulated emission by electrical pumping. Researchers were trying to utilize the tensile strain and proper n-doping to achieve direct Ge band gap in order to have lasing [38]. This approach is sometimes problematic. To achieve direct band gap for Ge, the tensile strain should be as large as 2%. This strain level is difficult to achieve. The high doping results a high threshold, which is undesired for the laser. The recent adopted method was the Hybrid Si lasers. III-V lasers bonding onto the Si substrate provide a decent light source for optoelectronic IC [39]. However, the bonding III-V devices are still challenging in yield, uniformity and cost reduction.

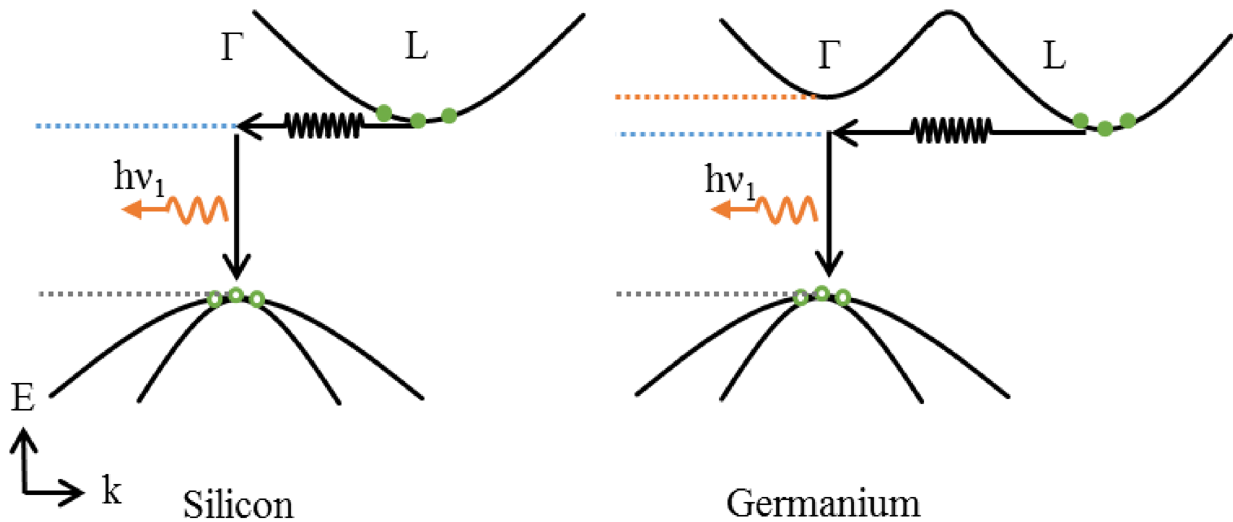

Figure 2: Schematic diagram of band structure for Si (left) and Ge (right).

All of these approaches appear to be exciting for being the candidates of next generation laser device integrated on Si. But they all have distinguished drawbacks. Thus, an efficient light source, with low cost, high reliability, and decent performance is needed.

GeSn alloy, a new branch of Group IV photonics, is seen as an excellent candidate material since this alloy could be grown monolithically on Si and its band gap can be tuned by incorporating of Sn [40]. Therefore, band gap engineering could be applied in Si based material.

Also, GeSn alloy has been proved to be direct band gap material [16]. By adding Sn composition, the direct band gap energy will drop faster than that of indirect band gap, shown in Figure 3. GeSn could be a direct band gap material. As a consequence, Group IV based optoelectronic devices with effective light-emitting sources are expected.

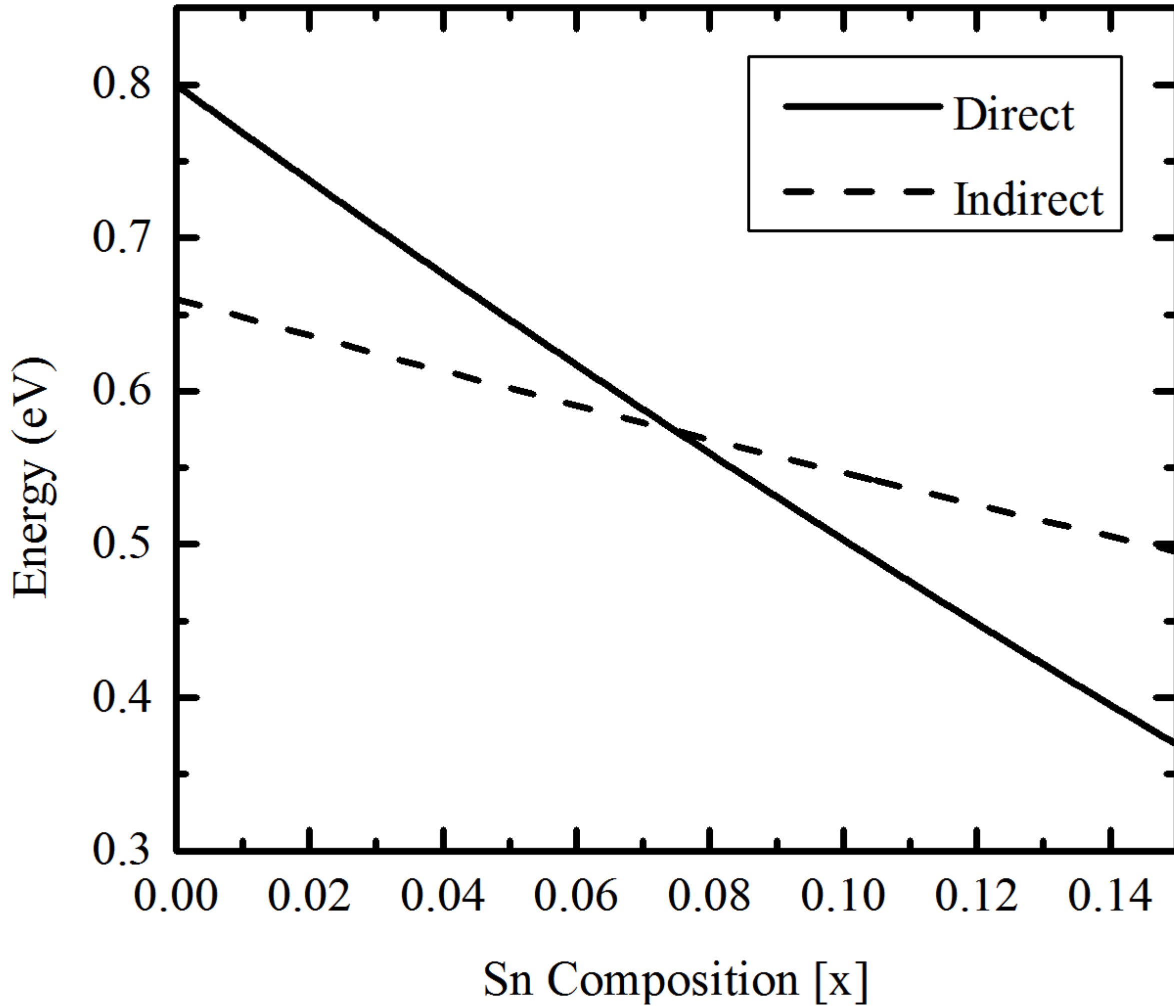

Figure 3: $Ge_{1-x}Sn_x$ band gap energy as a function of Sn composition [41].

1.2 Problems and Objectives

Studies in GeSn indirect to direct band gap transition had been investigated from various aspects. Although GeSn is promising for optoelectronic devices, further information should be investigated from the device perspective.

Direct band gap GeSn light-emitting devices should be investigated. GeSn based LED is a great platform to study the light-emission behavior. Furthermore, development of GeSn LED devices for advanced device study should be addressed. Electroluminescence study with Sn composition larger than 8% is desired.

To study the DHS LED behavior, different device design may serve for different research purpose. This development could help us understanding the device behavior with the change of geometry and designs.

Light-detection could also be studied for further information on GeSn based optoelectronic devices. Photodetector with extended detection range is expected to reach mid infrared.

To above concerns could further push the understanding of GeSn based optoelectronic devices for various applications.

1.3 Organization of Thesis

This thesis is a study of GeSn based optoelectronic devices. Starting with the study on Ge/GeSn/Ge DHS diode operating as LED, investigation included various aspects from material characterization, device fabrication, to device characterization. Light-detection with simple structures was also discussed. Six chapters of contents composite the entire thesis.

Chapter 1 is an introduction of the Si photonics and GeSn optoelectronic devices. It provides the opportunities and challenges in the current research area. Then the chapter leads to the current problems and objectives, and follows with the organization for this thesis.

Chapter 2 discusses the characterization results from the grown material using, XRD, PL, and transmission electron microscopy (TEM). These results evaluate the material quality for later device fabrication and characterization. And some material behaviors are going to compare with later device characterization.

Chapter 3 focuses on the fabrication process and characterization of the surface-emitting LED. GeSn material behaviors through the fabrication process will be shown and discussed. After fabrication, the chapter will discuss device characterization, including I-V measurement, EL, and optical power measurement. As the fabrication and characterization going through, new generations of devices with improving current injection level and uniformity are will also be described.

Chapter 4 starts the investigation on the edge-emitting LED. This type of device is mainly aimed at optical confinement and optical mode as the first attempt of lasing device. Process and preliminary characterization will be demonstrated and follow with further discussion on the outcomes.

Chapter 5 extends the material application to photodetectior. The light-detecting behavior of photoconductors as well as p-i-n diodes will be discussed.

The last chapter will summarize the results, review the current obstacles, and suggest the later research direction.

Chapter 2: Material Characterization

2.1 Introduction

The material used in this work was grown by ASM using Epsilon® reduce chemical vapor deposition (CVD) reactor. The material was grown on a 200 mm wafer under the temperature below 450˚C. The structure of GeSn LED was designed to be a DHS. This structure contains four sections. The Si (100) wafer was a low doped substrate with background doping of 1×10^{15} cm^{-3}. A 700 nm Ge buffer layer was doped by p-type dopant with concentration of 5×10^{18} cm^{-3}. A 200 nm $Ge_{1-x}Sn_x$ layer was then deposited with no intentional doping. Thereafter, a 50 nm Ge cap layer was deposited with n-type doping concentration of 1×10^{19} cm^{-3}. The film was then examined by TEM. Threading dislocations in $Ge_{1-x}Sn_x$ were found to be controlled within a reasonably low level.

2.2 X-ray Diffraction (XRD)

XRD is a method to portray the atomic structure of crystal. The crystal structure could be probed by recording the reflection X-ray intensity as a function of omega and/or 2theta (shown in Figure 4). The incident angle omega was the angle between the incident X-ray and the surface of the sample. The diffracted angle, 2theta, is the angle between the extended incident beam and the detector angle. When X-rays are incident in onto the atom place in periodic order (crystal), electrons will be scattered as periodic electromagnetic waves from the atoms. This wave forms the interference which could be detected in terms of intensity at a scanned angle. The plot of scanned intensity as function of angles is called rocking curve. This curve could provide the lattice constant from each layer of material as well as the material quality.

The DHS was characterized using HR-XRD. Rocking curves, shown in Figure 5, have the clear peaks for Ge and GeSn layers. The increasing of Sn composition caused GeSn layer

reflection peak shift away from the Ge peak, indicating the increasing of out of plane lattice constant. The Ge buffer layer was originally designed to be relaxed and confine the defect propagation from the Ge/Si interface. Due to the Ge cap layer, the Ge peak resulted an asymmetrical shoulder in a higher degree. This indicates the tensile strain existed in cap layer for higher Sn (8%) composition.

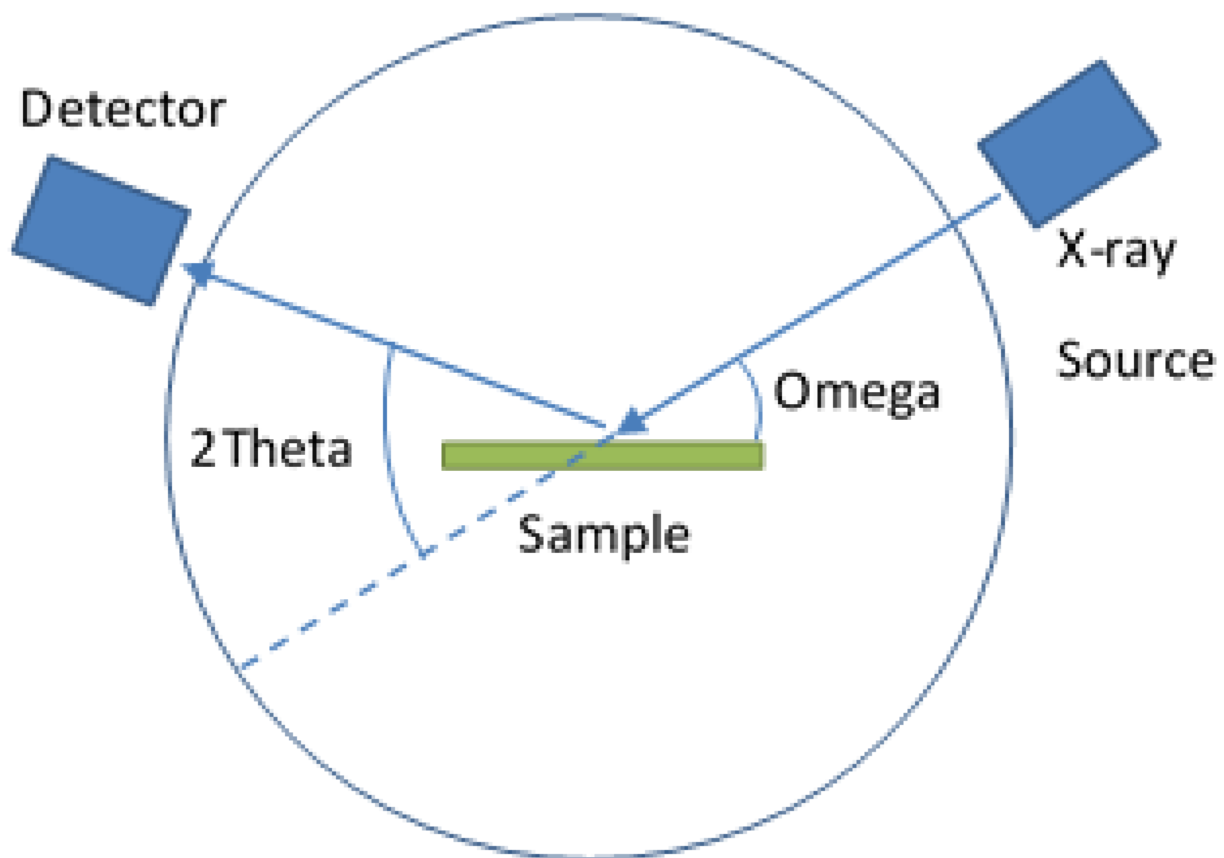

Figure 4: Schematic diagram of XRD setup.

.

Figure 6 shows the reciprocal space maps measured from (-2 -2 4) plane. It disclosed the in plane partially compressive strain was also existed in GeSn layer. The GeSn layer in the map fell to the right side of pseudomorphic line. This result confirmed that the grown GeSn layer was only partially strained.

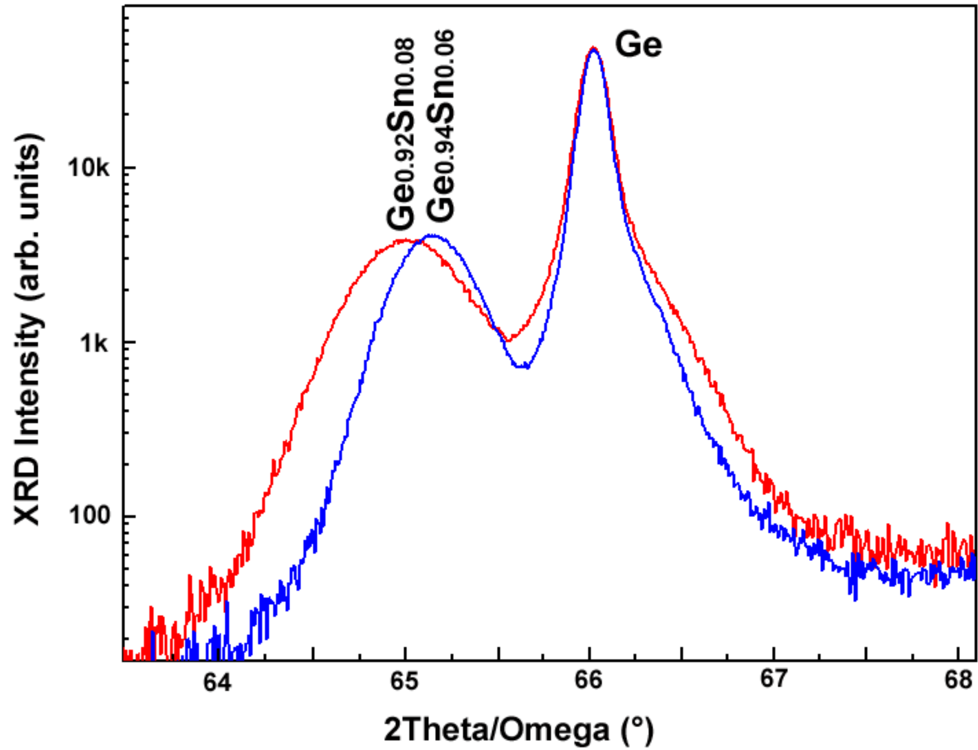

Figure 5: XRD 2theta-omega 2θ-ω scan for 6% and 8% Sn sample [17].

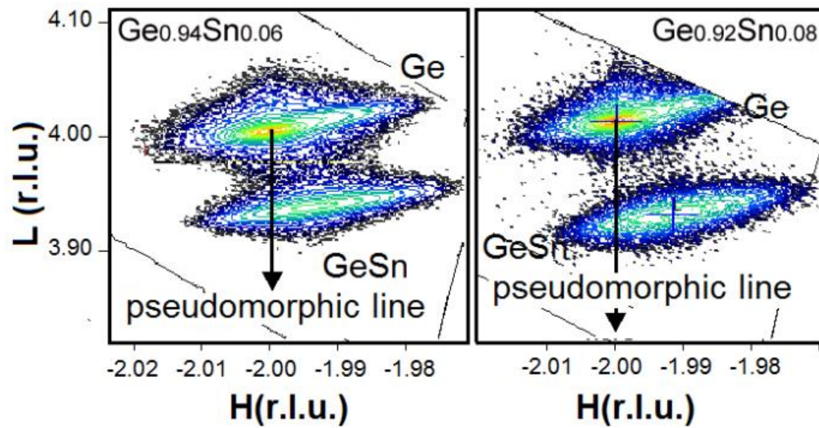

Figure 6: Reciprocal space maps from (-2 -2 4) plane of $Ge_{1-x}Sn_x$ films with 6% (left) and 8% Sn (right) [17].

2.3 Photoluminescence (PL)

The home built off-axis PL setup is shown in Figure 7. Laser beam was guided onto sample surface with a certain incident angle. The laser was operating with the wavelength of 532

nm and 100 μm diameter of spot size under the chopping frequency of 377Hz. The sample surface was therefore injected with holes to excite the radiative recombination. PL signal was scatter away from the sample surface. A CaF_2 concave lens was utilized to collect and collimate the scattering PL signal. A second CaF_2 lens focused the light into the slit of the spectrometer. A band pass filter was used to filter out the scattered laser light. And another low pass filter was used to block high order harmonic Chopper and lock-in amplifier was used to eliminate the noise for a decent signal to noise ratio.

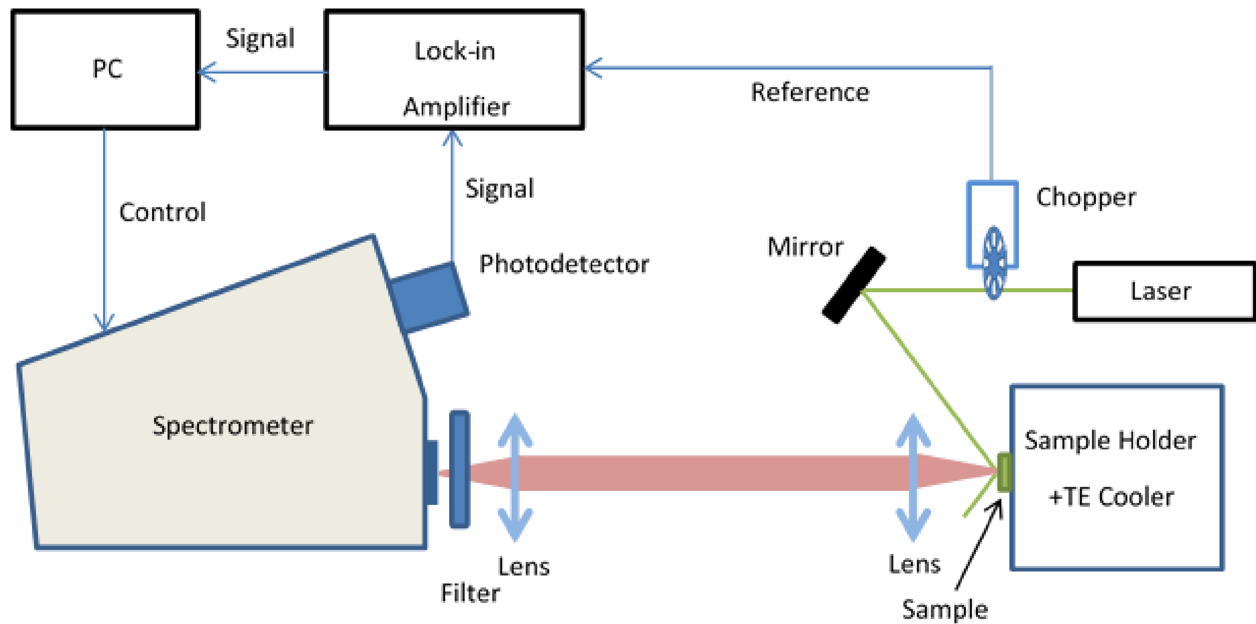

Figure 7: Schematic diagram of PL setup.

PL study was conducted for the material. This measurement could provide an emission spectrum under hole carriers inject by photon excitation. Radiative recombination contributed by hole injection reflected the band gap of the material in the emission spectrum. This spectrum would be used for comparison with electrical injection of both electrons and holes.

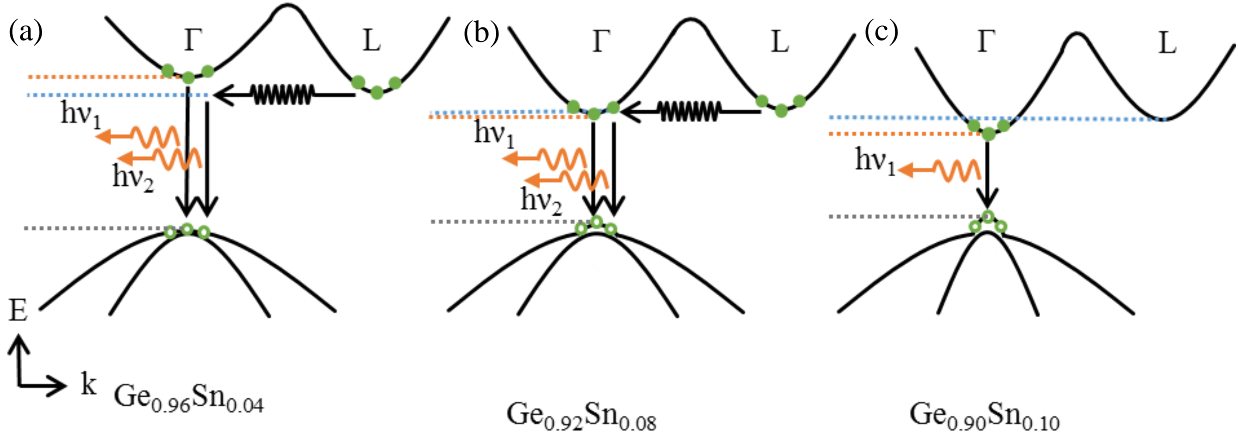

Figure 8: Schematic diagram of PL mechanism in band structure with Sn composition of (a)3.2%, (b)8%, and (c)10%.

Figure 8 demonstrates the PL mechanism for GeSn alloy studied. For lower Sn composition, in Figure 8 (a), most electrons fall into L valley and recombine with hole with the assistance of phonons. Only a small fraction of electrons falls into Γ valley and recombine with holes without any change of momentum. These two kinds of recombination result in two peaks in PL spectrum. For Sn composition around 8%, in Figure 8 (b), Γ and L valley are on the same energy level, transition from both valleys through the similar energy gap results in an overlap of two peaks with wide line width. When the Sn composition reaches to 10%, in Figure 8 (c), most electrons fall into the lower Γ valley and therefore recombine with holes with the direct band gap transition. The emission from the indirect band gap transition could be ignored because of the possibility of recombination in indirect band gap transition is several orders of magnitude lower than that of direct band gap transition. Thus, the PL spectrum of 10% Sn sample has a single peak with a narrow line width, which indicating its true direct band gap nature. This result testified the theoretical prediction and demonstrated the potential of GeSn material for light-emitting application.

Figure 9 demonstrates the PL spectra for GeSn thin film on Ge buffer. The Ge and 3.2% Sn sample was measured by extended InGaAs detector, while the 8% and 10% Sn film was measured using PbS detector. The Ge reference had the maximum intensity due to the bulk structure. PL of 3.2% thin film had multiple peaks contributed by GeSn direct, indirect band gap, and Ge direct and indirect band gap. For 8% Sn sample, PL spectrum had a single, broad peak, which could be the overlap of direct and indirect band gap transition from GeSn. The full width half max (FWHM) was wider than that of 10% Sn sample. For the 10% Sn sample, PL had only one narrow peak, which was contributed only by direct band gap transition. The direct band gap material resulting an enhancement on intensity compare to 8% Sn sample.

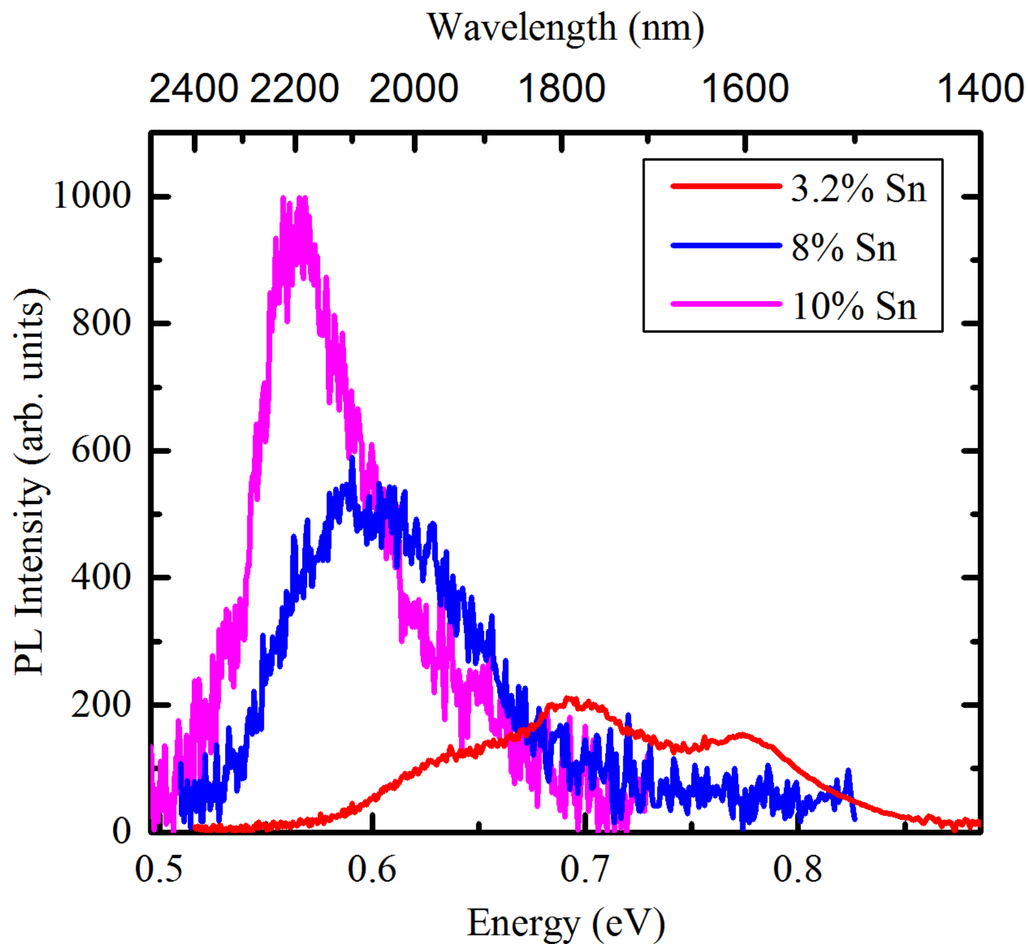

Figure 9: PL spectra for GeSn thin film with Sn composition of 0%, 3.2%, 8%, and 10% [16].

Figure 10 is the PL spectrum of the DHS with Sn composition of 6% and 8%, compared to bulk Ge reference. Emission peak and FWHM information with Sn composition is listed in Table I. The increasing of Sn composition made the band gap smaller, resulting a red shift of PL peak. The FWHM was used to determine the defect density in the material. As Sn increase, more Sn induced dislocation led to a wider FWHM. This was also the reason why the 8% Sn PL intensity was lower than 6% Sn sample. Once the material growth become mature and high quality GeSn can be grown, direct band gap emission is expected to have stronger emission than indirect band emission.

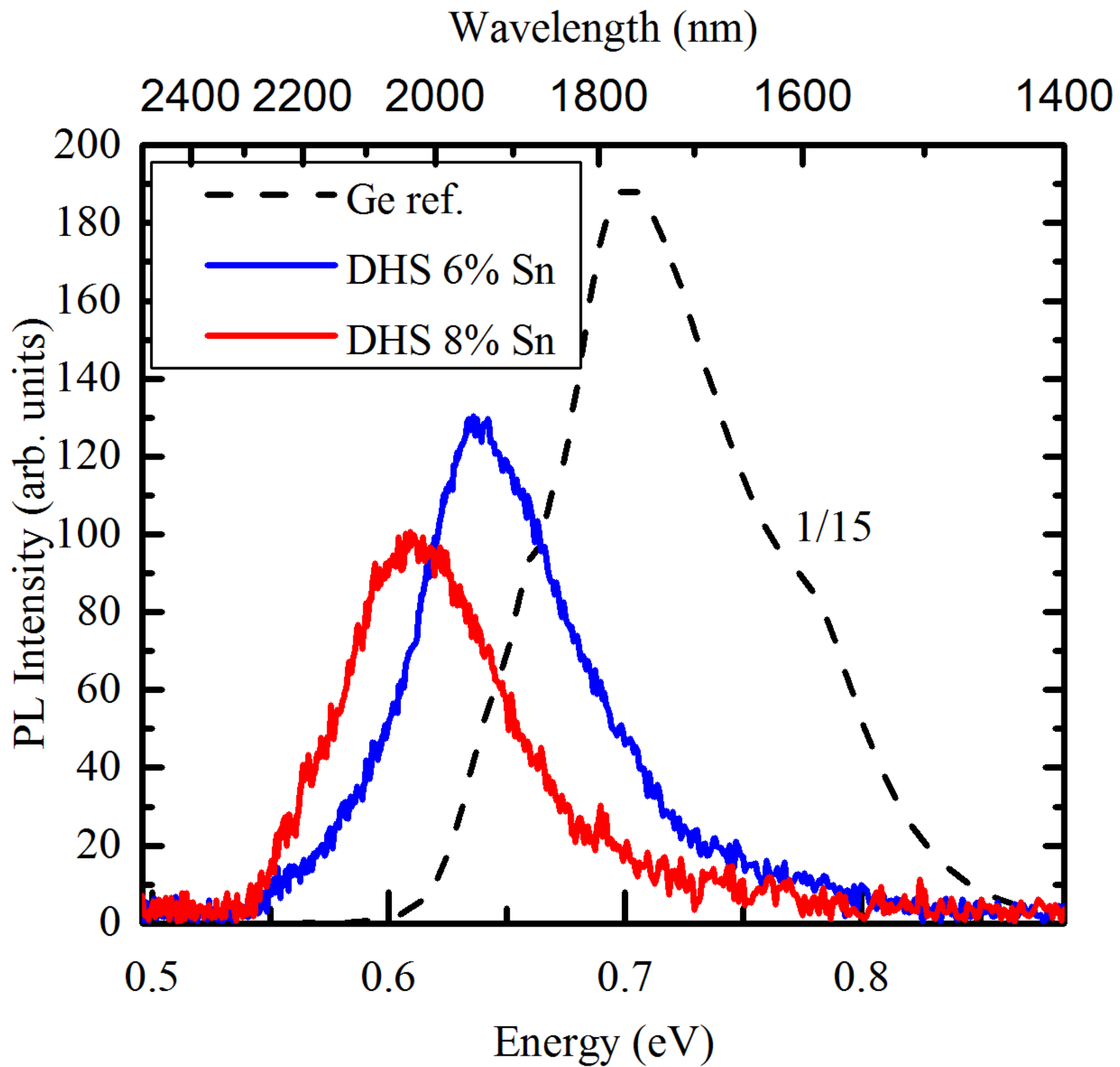

Figure 10: PL spectra of Ge reference, DHS 6% Sn sample, and DHS 8% Sn.

	PL Peak Energy (eV)	PL Peak Wavelength (nm)	FWHM (meV)
$Ge_{0.94}Sn_{0.06}$	0.642	1932	80
$Ge_{0.92}Sn_{0.08}$	0.607	2042	84

Table I: Peak positions and FWHM of PL measurement.

Chapter 3: Surface Emitting LEDs

3.1 Introduction

Surface emitting LED can be used into LED arrays for a uniform, optical power enhancing purpose. Single surface LED devices are discussed in this chapter. The fabricated devices was be characterized using I-V measurement, EL, and optical power measurement. The structure of the device is showing in Figure 11. The mesa was formed by chemical wet etching. Electrodes of Cr and Au were deposited using thermal evaporation. When the electrical field applied between the metal contacts on n and p-type Ge, current will flowing from p-type germanium, then through the intrinsic GeSn region, and eventually to the n-type germanium. The band alignment for DHS is expected to be type I alignment, which could confine carriers within the GeSn active layer.

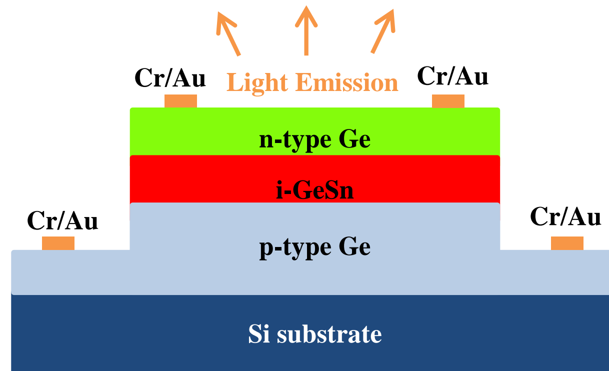

Figure 11: Schematic diagram of cross section for the surface emitting LED.

3.2 First Generation Device

Fabrication

All fabrication process was done in a class 100 cleanroom so that the particles in the ambient environment are under control and have the minimum contamination level. Process for the LED device fabrication from a grown wafer includes the major steps shown below in Figure 12.

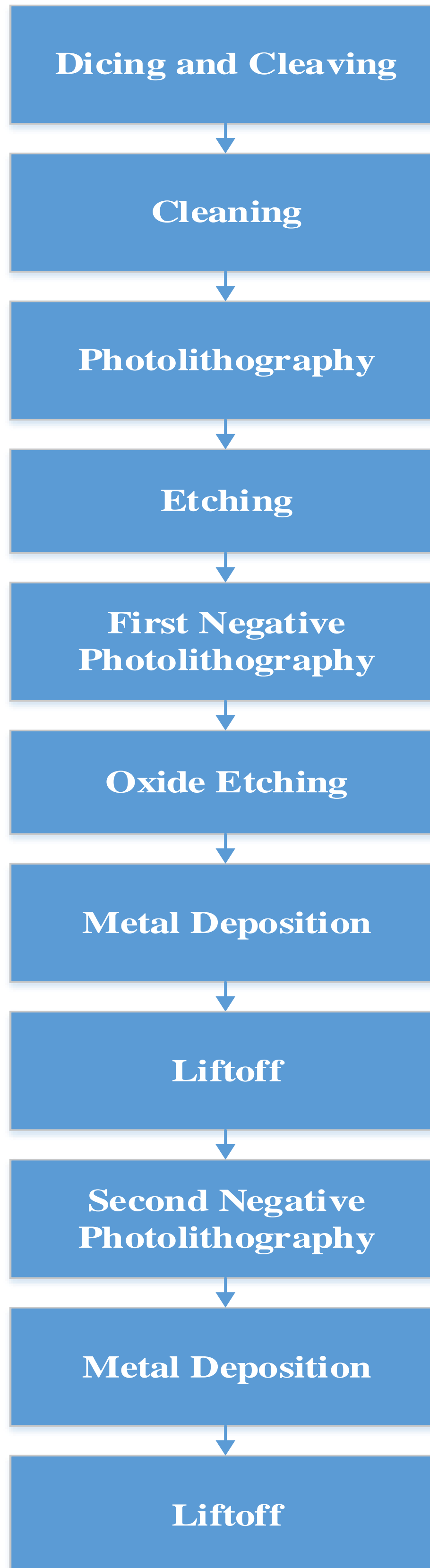

Figure 12: Process flow of first generation LED fabrication.

Dicing and Cleaving

The grown material was originally on a 200-mm (100) Si wafer. The wafer needs to be diced or cleaved into small pieces. For large wafer, dicing saw was used to cut wafer into medium squared samples (2 cm by 2 cm). Dicing saw has a rotating blade which composed of diamond and metal mixture. Programmed dicing saw could perform a straight, uniform, precise cutting. For cleaving small samples, it is preferred to use a diamond scribe. Diamond scribe could break the sample along the crystal orientation of <110> direction. The positions of small samples from the large wafer were recorded according to a wafer map demonstrated in Figure 13 (b) and (c). These locations information could be used to test the uniformity of the grown wafer. Also, all devices fabricated should choose the same region. For example, the most center piece of the wafer from B1 region is named as “B1E”, where samples from B1 are used for device fabrication purpose. After cleaving, pre-cleaned sample boxes with labeling were used for storing the sample.

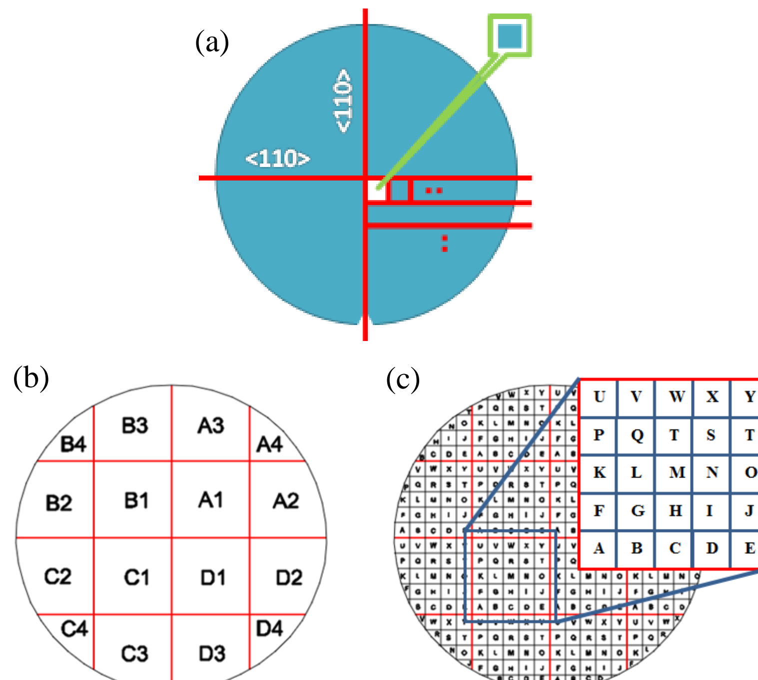

Figure 13: (a) Dicing & cleaving wafer orientation, (b) and (c) wafer map for the sample cleaving.

Cleaning

Defect free in the process is critical for the performance of the final devices. Due to the sample handling between the growth and fabrication, particles and chemical residues would stay on the sample surface. Solvent clean was performed to remove most of the contamination. The sample was first dipped into acetone under sonication for 5 minutes. Acetone will effectively remove the organic contaminations. Sonication helped to accelerate the reaction and also physically separate the particles from the sample surface. The sample was transferred into isopropyl alcohol (IPA), which can dissolve the contaminated acetone. Then deionized water (DI water) was used to rinse the IPA. The nitrogen gun flew the N_2 gas to dry the water along the sample. And sample was put on a hotplate and bake at 95 ℃ for 2min for a completely dry.

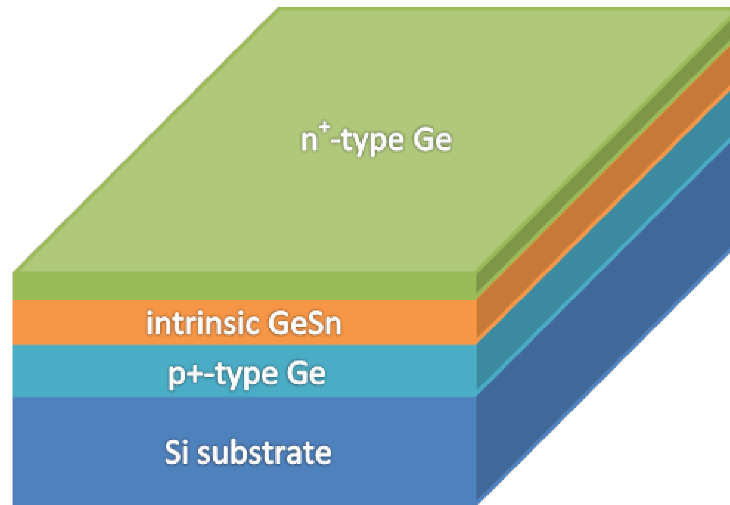

Figure 14: Schematic diagram of sample structure before fabrication.

Photolithography

For the surface-emitting LED device, with a sample with p-i-n thin films on Si substrate (shown in Figure 14), we would firstly to form isolated mesas which can subsequently use as devices. The pattern was predefined on a photo-mask, a glass substrate with Cr drawing on the

surface. Photolithography was used to transfer the pattern from the photo-mask onto the photoresist coated on the sample.

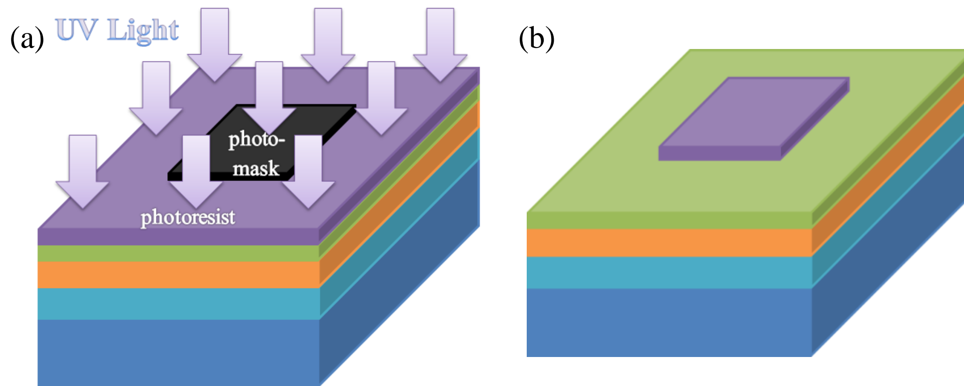

Figure 15: Schematic diagram of positive photolithography process. (a) Ultra violet (UV) light exposure (b) after development.

To define a pattern on sample, the positive photolithography process was performed (demonstrated in Figure 15). Photoresist was applied using spin coating. The photoresist is a light sensitive chemical substance. And it could work as a passive coating protecting the covered field. Radiating the light with high light energy (UV light) will change the property of the photoresist and make it soluble in certain chemical—developer. This special property is therefore applied to transfer the configuration from a pre-defined photo-mask onto the photoresist. The photo-mask blocks the light with the features so this area will survive in the developer. Yet the area exposed to the light will be dissolved. As a result, photoresist covered the area with designed patterns.

After the photolithography, a descum procedure was performed to clean up the possible photoresist residues in the opening window. In a vacuum chamber, oxygen was flowing through the chamber with a high power radio frequency wave added. The oxygen plasma will burn off the residue layer of photoresist into exhaust gas and eventually pump out.

Etching

Etching process is aimed at form mesas on the grown sample, shown in Figure 16, which later will be devices. In this work, both chemical wet etch and reactive ion etch (RIE) were performed. Chemical wet etch provides an isotropic result, while RIE ends for an anisotropy one. Chemical wet etch is the basic method for semiconductor process. For Ge etch, hydrochloride acid is a good reactant. Together with hydrogen peroxide, the solvent could etch Ge and GeSn effectively. A solution with $HCl:H_2O_2:H_2O=1:1:20$ was prepared and stabilized for 30 minutes. Before immersing the sample into the solvent, the sample surface should be pre-soaked with deionized water. This process was to prevent the air bubble forms on the small openings which could result in a non-etched or few-etched result. The etching thickness as a function of time is shown in Figure 17. And the etching rate for DHS is shown in Figure 18 as a function of time. For chemical wet etching, etching rate of the GeSn sample was slower with higher Sn composition. RIE is another technique which using both chemical and physical reaction to etch the sample surface. Florid tetrachloride and argon was used to selectively etch down the Ge and GeSn layer. And the etching will stop at Si substrate.

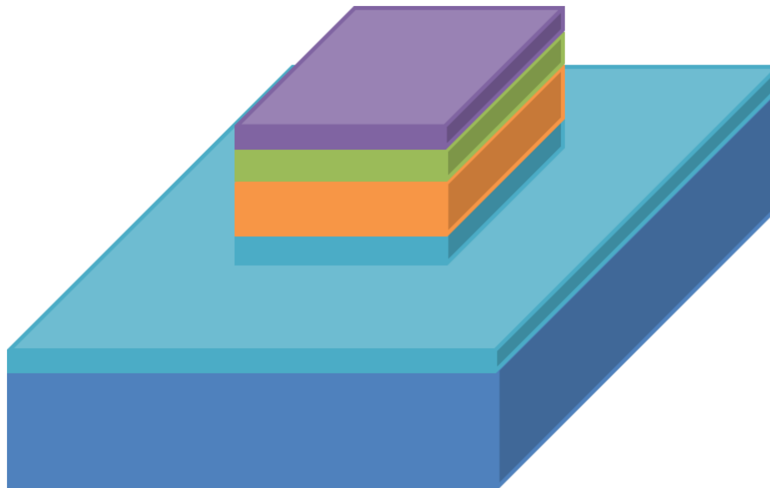

Figure 16: Schematic diagram of etched sample.

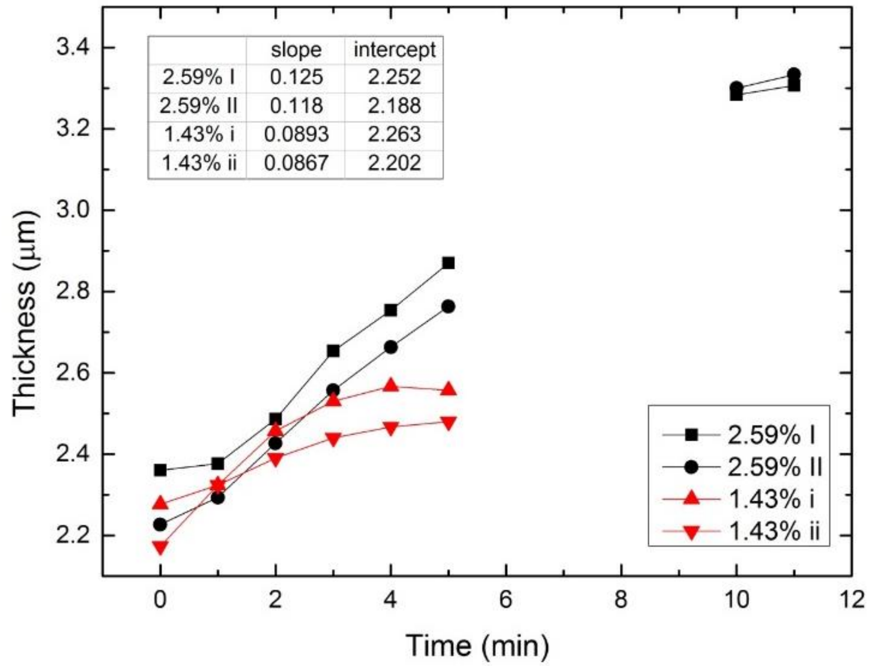

Figure 17: GeSn thin film etched mesa height (with initial photoresist thickness) as a function of etching time.

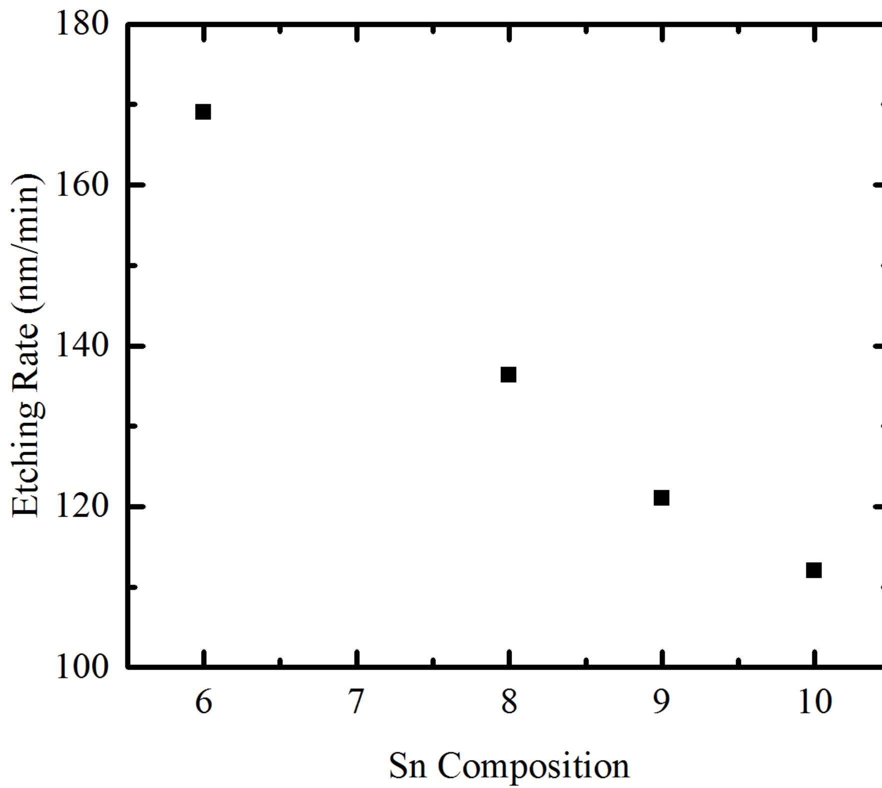

Figure 18: $Ge/Ge_{1-x}Sn_x/Ge$ DHS etching rate in $HCl:H_2O_2:H_2O$=1:1:20 solution with various Sn composition.

Another method of etching GeSn structures is reactive ion etch (RIE). This advanced technique provides a much faster etching rate on vertical direction than lateral. The etching rate was inversely proportional to Sn composition. During the process, GeSn will be etched by both chemical and physical process. SF_6 flew through the vacuum chamber to etch the material chemically. Also, plasma form inside the chamber will etch the sample held with (radio frequency) RF power electrode. The ion will physically attack the surface along the electric field direction which is vertical. Compared to chemical wet etching, RIE will form a steeper edge, shown in Figure 19, which was preferred for some of the device design.

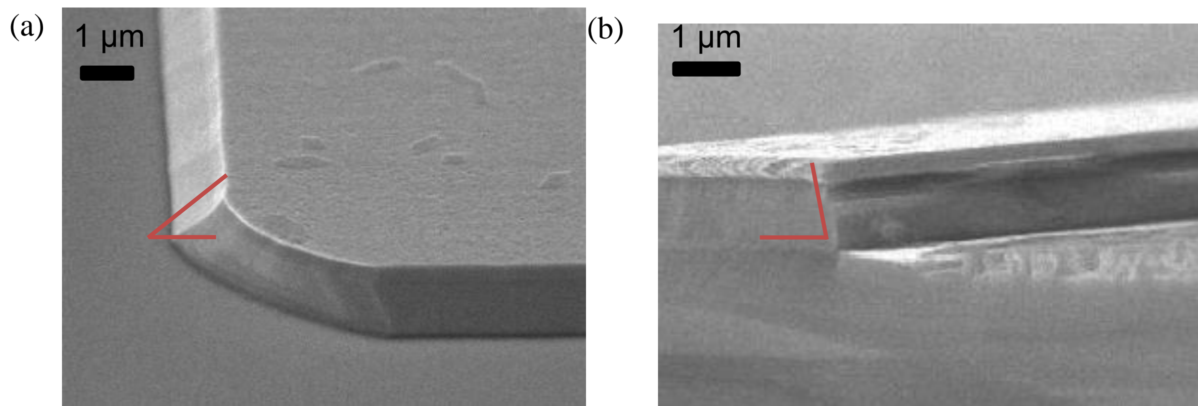

Figure 19: Scanning electron microscope (SEM) image of the etching result from (a) chemical wet etching and (b) RIE.

First Negative Photolithography

First negative photolithography was performed to form the first metal contacts. Different from the positive photolithography that used to define the mesa, negative photolithography will reverse the pattern. The photoresist configuration needs to be reversed to have some undercut from the edge for better liftoff, show in Figure 20. In this way, metal deposit on the sample will not connect together due to the undercut. Therefore, it was easier for liftoff process, shown in Figure 20. Image reverse process needs to have a post baking and flood exposure before

developing. After the first exposure, the photoresist will show the defined patterns. The post bake at a higher temperature changes the property of the photoresist. A flood exposure was used to switch the photoresist properties between exposed and unexposed area. After developing, the features were therefore formed reversely from the photo-mask, shown in Figure 21.

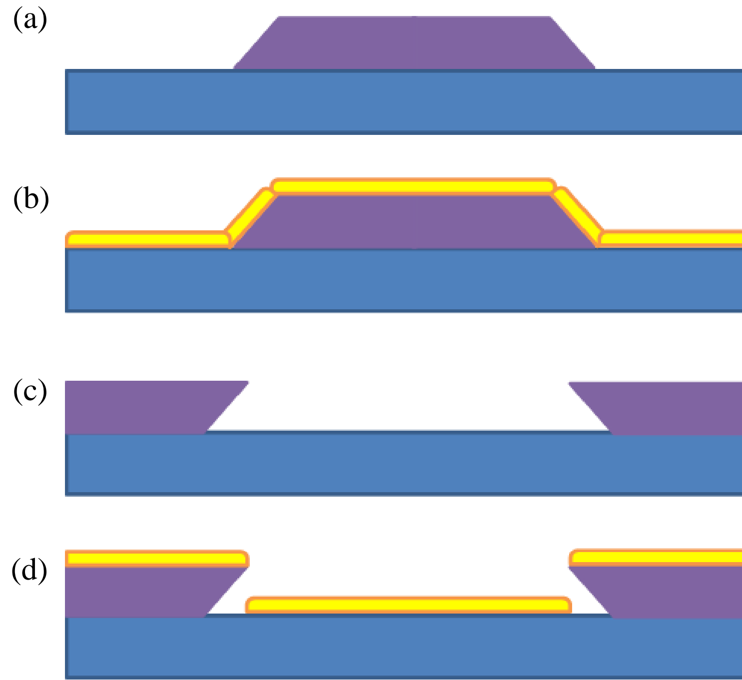

Figure 20: (a) Positive photoresist, (b) metal deposited on positive photoresist, (c) negative photoresist, and (d) metal deposited on negative photoresist.

Another descum was followed after photolithography. Because of the oxygen plasma, sample surface may have been oxidized. Therefore, it was necessary to perform a chemical etching process for the possible oxide on the surface. This was completed by dipping the sample into the buffer oxide etch (BOE) solvent. The hydrogen fluoride (HF) in the solvent will effectively etch germanium oxide and leave the bare Ge exposed.

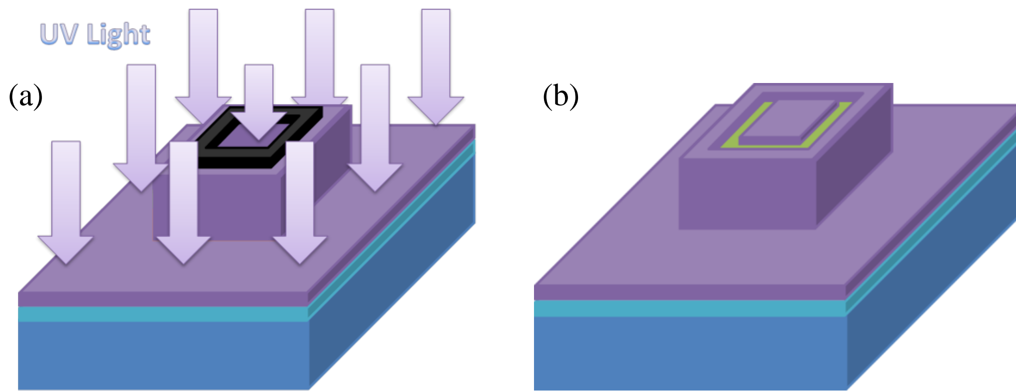

Figure 21: Schematic diagram of negative photolithography (left) and after development (right)

Metal Deposition

Thermal evaporation was used for metal deposition. In a vacuum chamber, metal was added high current and heated up to evaporation temperature. Cr and Au were used to form the metal contacts. A 10 nm Cr was used for an Ohmic contact with Ge. Then a 200 nm Au was deposited for better electrical conductivity.

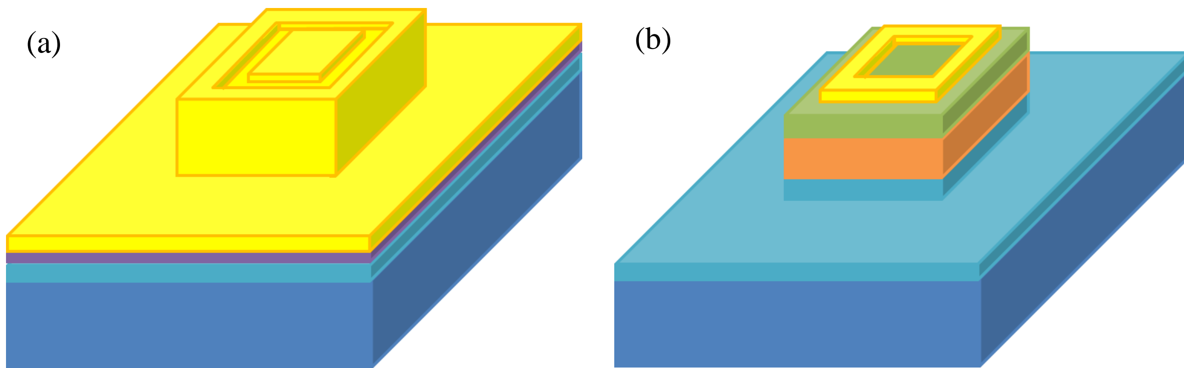

Figure 22: Schematic diagram of (left) metal deposition and (right) liftoff result.

Liftoff and Second Metal Deposition and Contact

Right after the metal deposition, the liftoff was performed by soaking the sample in acetone for 10 minutes. Use the pipets to gently blow acetone onto the liftoff surface if the pealing metal remains. Sonication should be used with caution in the persisting metal pieces.

After the extra metal peeling off, the fresh acetone and IPA were used to clean the sample. After the first metal contact formed, shown in Figure 22, the second metal contact was deposited using the similar process with another negative photolithography, metal deposition and liftoff.

LED device was therefore fabricated with co-plane contacts, shown in Figure 23. The 1 cm by 1 cm square sample have the LED devices with different side dimensions: 500 μm, 750 μm, 1000 μm, 1500 μm, and 2000 μm.

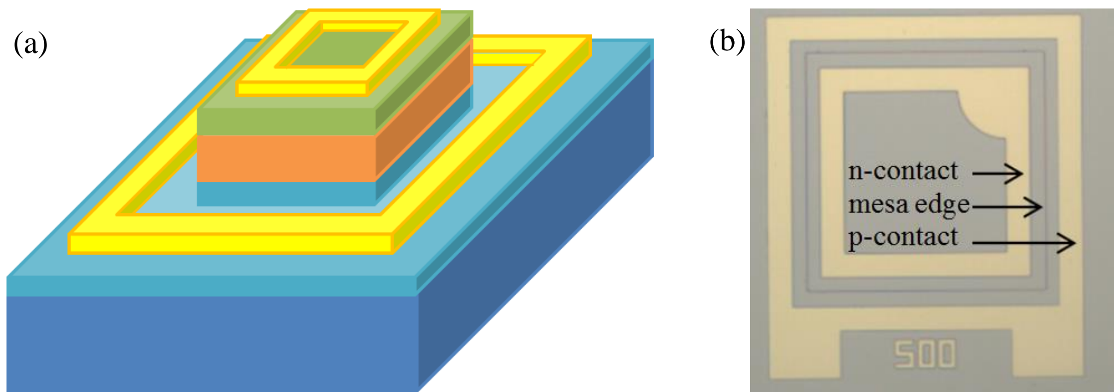

Figure 23: (a) Schematic diagram of fabricated LED device, and (b) optical image of top view.

Device Characterization

As the device fabrication completed, LED devices were characterized. For LED, I-V measurement could not only provide a quick test if the device was functioning properly, but also indicates the dominating mechanism for the current. EL could use to observe the emission spectrum and further information. Optical power was measured using power detector to estimate its power level and the emission efficiency.

First of all, with given devices, I-V curve was measured comparing with various mesa sizes, shown in Figure 24. The behavior showed the larger the mesa had less rectifying. One potential reason is from increasing surface recombination on larger areas. Large area made current spreading out through the layers, causing lower resistance. Smaller devices had crowding

current through the limit area so the current density is relatively larger than large devices. The leakage current was contributed from two components: surface leakage current and bulk leakage current. The relation can be described in [42]

$$I_0^{Total} = J_0^{Surface} \cdot Perimeter + J_0^{Bulk} \cdot Area$$

where $I_0^{Total}$is the total leakage current, $J_0^{Surface}$is the surface leakage current density, and I_0^{Bulk} is the bulk leakage current density. The derivative of the total leakage current respect to device area is the bulk leakage current density. Then the surface leakage could be calculated by subtracting total leakage current by bulk leakage current [43]. It was calculated 55% of the total leakage current from 2 mm side device was contributed by the surface leakage current. Therefore, surface leakage exists and affects the diode current behavior.

Since the emission intensity is proportional to the current density, the smallest device, 500 μm by 500 μm size, was chosen with the clearest rectification. The dark I-V measurement and a clear rectifying behavior were observed on both 6% Sn and 8% Sn $Ge_{1-x}Sn_x$ samples, shown in Figure 25. Also, as the Sn composition increase from 6% to 8%, the current increased, this is due to higher mobility from the higher Sn sample. The resistivity was therefore reduced when more Sn was cooperated. Figure 26 shows the temperature dependent I-V characteristics. Five parts could be identified in the different voltage region.

In Figure 26, all forward currents with higher voltage converge together. This is primarily due to the series resistance, and it is temperature-independent. The series resistance was extracted to be 15 Ω for 8% Sn LED device.

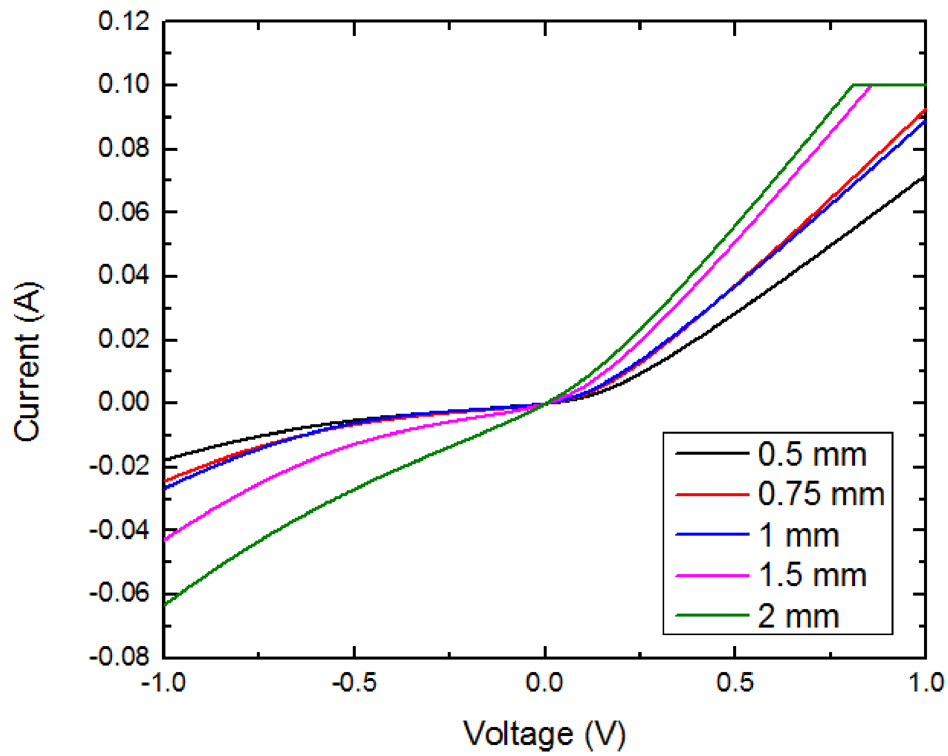

Figure 24: I-V measurement with various mesa sizes

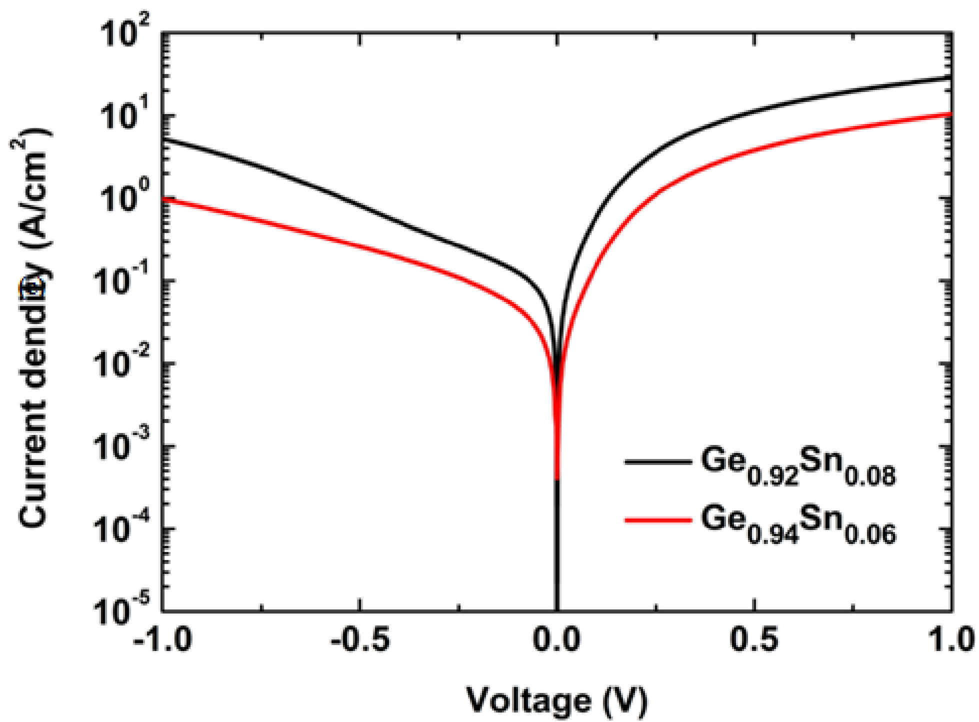

Figure 25: I-V for 6% Sn and 8% Sn devices with 500 μm mesa at room temperature [17].

The forward current under low voltage (less than 0.5 V) has a small variation with temperature changing. A data fitting is shown in Figure 27, where an ideality factor n=1.93 was extracted. By fitting the diode current equation

$$J = J_0 \left[\exp\left(\frac{qV}{nkT}\right) - 1\right] \quad \text{(Equation 1)}$$

where J is the current, J_0 is the diode saturation current, q is the absolute value of electron charge, V is the bias voltage, n is the ideal factor, k is the Boltzmann's constant, and T is the temperature. An ideality factor close to two of the fitting curve in means recombination current dominated the device instead of diffusion current. Current mechanisms is shown in Figure 28.

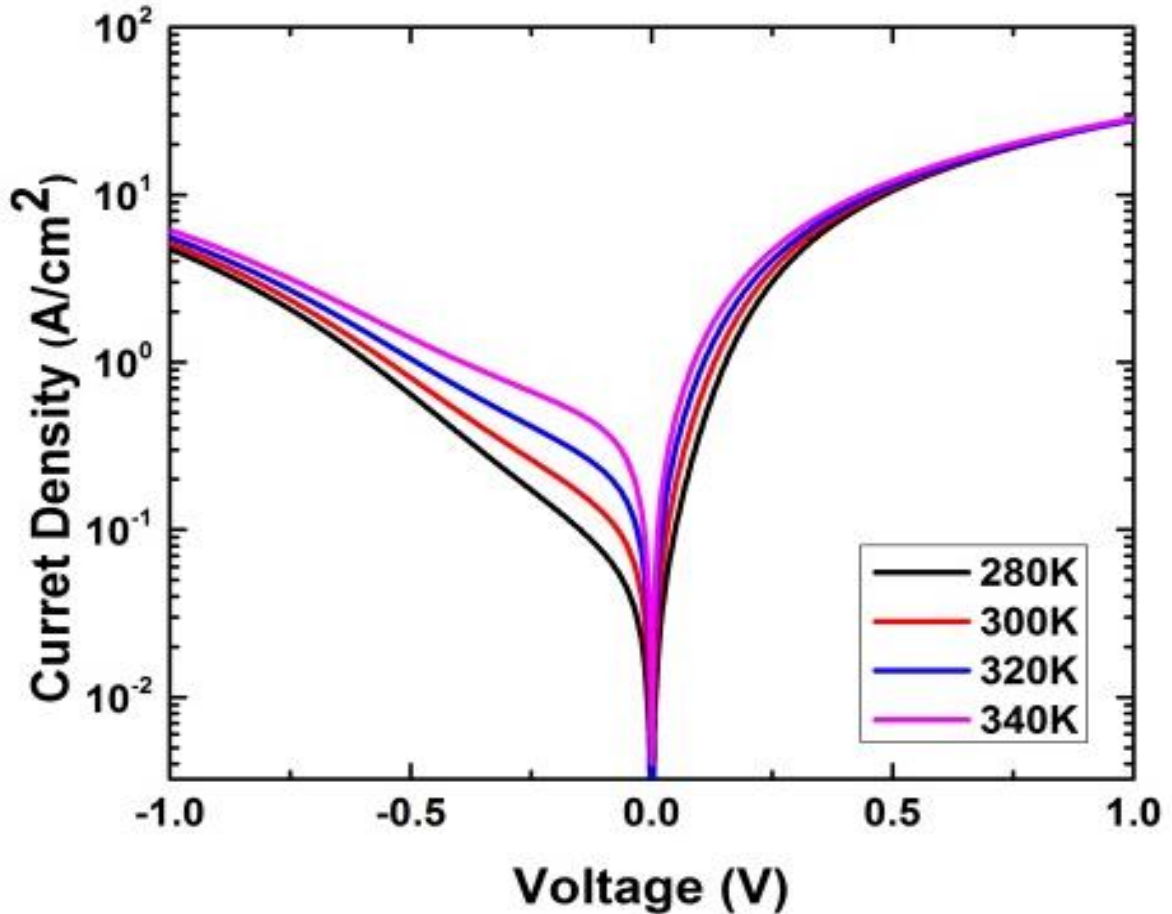

Figure 26: Temperature dependent I-V for 8% Sn device with 500 μm mesa.

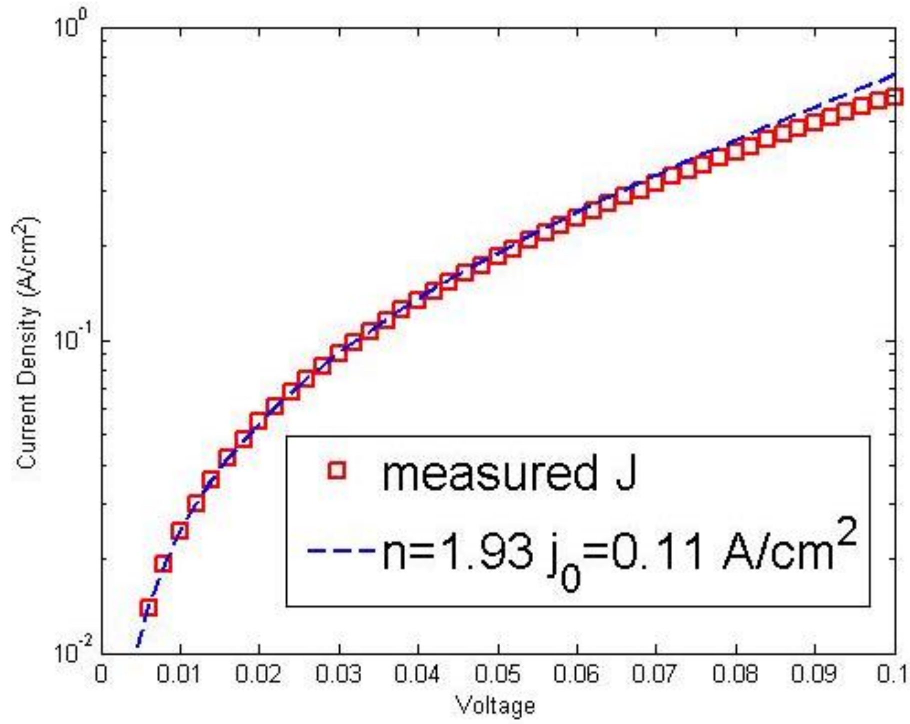

Figure 27: Fitting forward current for 8% Sn devices with 500 μm mesa.

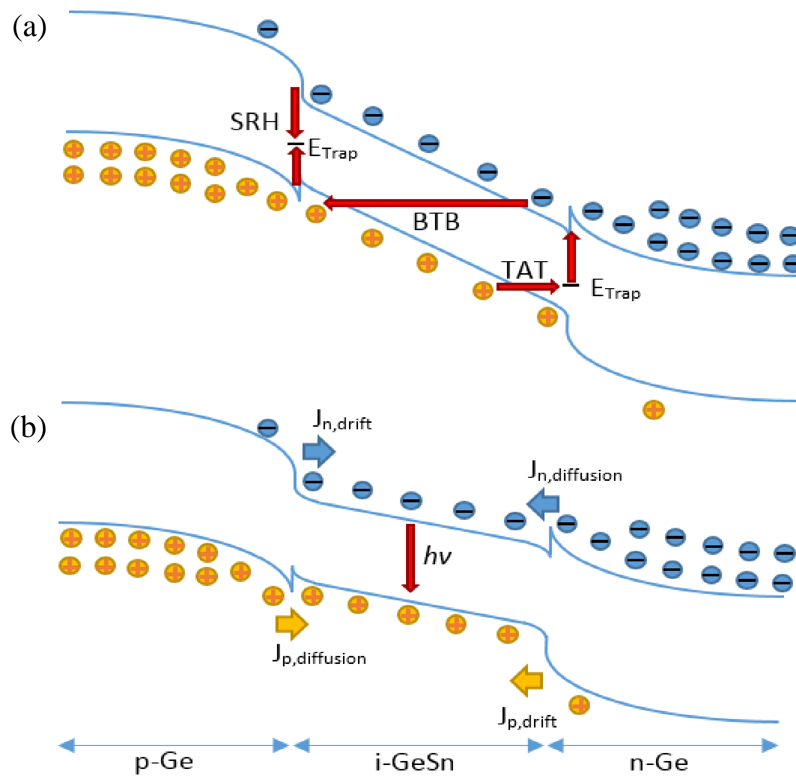

Figure 28: Schematic diagram of current mechanism in p-i-n diode (a) BTB, TAT, and Shockley-Read-Hall recombination, and (b) diffusion, drift current, and radiative recombination.

For the current under small reverse bias (-0.7 V<V<0 V), diffusion current ($J_{diffusion}$) and recombination (J_r) are dominated and has a large variation with temperature changing since J_{diff} and J_r are proportional to n_i^2 and n_i respectively, where n_i is the intrinsic carrier concentration, which is proportional to $T^{3/2}$.

For reverse current under large reverse bias (V<-0.7 V). This region the current is dominating with tunneling current. Two main mechanisms contribute to this type of current: trap-assist tunneling (TAT) and band to band tunneling (BTB) that is relatively independent of temperature. The TAT is the carrier tunneling through the trap level and related to the trap density and trap energy level. The BTB depends only on band gap and has a small variation with temperature changing. Also, with higher reverse bias BTB dominates the current behavior.

I-V measurement could provide the primary information of the quality for the LED devices from the extraction information from the data. And the improvement could be made base on the measurement results.

EL is the illumination of light from semiconductor under electrical injection. Different from PL, EL has two carrier injections, electrons and holes from either side of a diode. The emission spectrum is one of the key properties of the LED device.

The setup of EL, shown in Figure 29 includes current source and connections, optical path, spectrometer and photodetector, and noise filter. The electrical connection was composed by a function generator providing a 377 Hz, 50% duty cycle square wave with a positive offset and a 5 V peak to peak amplitude. The square wave was carried by the BNC to BNC coaxial cable connected to the probe station. The positive connection was pressed onto p-contact of the device and negative connection on n-contact. Whenever the device was applied the forward bias, optical fiber was then held above the device to collect the light emission from the device top surface. Collected light was guided to a focal CaF_2 lens to collimate the beam. Another focal lens

was used to focus the light at the entrance slit of the spectrometer. Light in spectrometer will be reflected to a grating filtering the spectrum into a single wavelength and send this monochromatic light to photodetector. The signal from the photodetector was then sent to the lock-in amplifier providing a reference signal from the pulse voltage source so the noise with different frequency will be blocked. A high signal to noise ratio signal was then recorded using the PC. The PC then sent the instruction to spectrometer for another grating position. The next wavelength light intensity was read with the same method. In the end, when all the wavelengths were scanned and all the intensity information was recorded, the emission spectrum was collected under the EL setup.

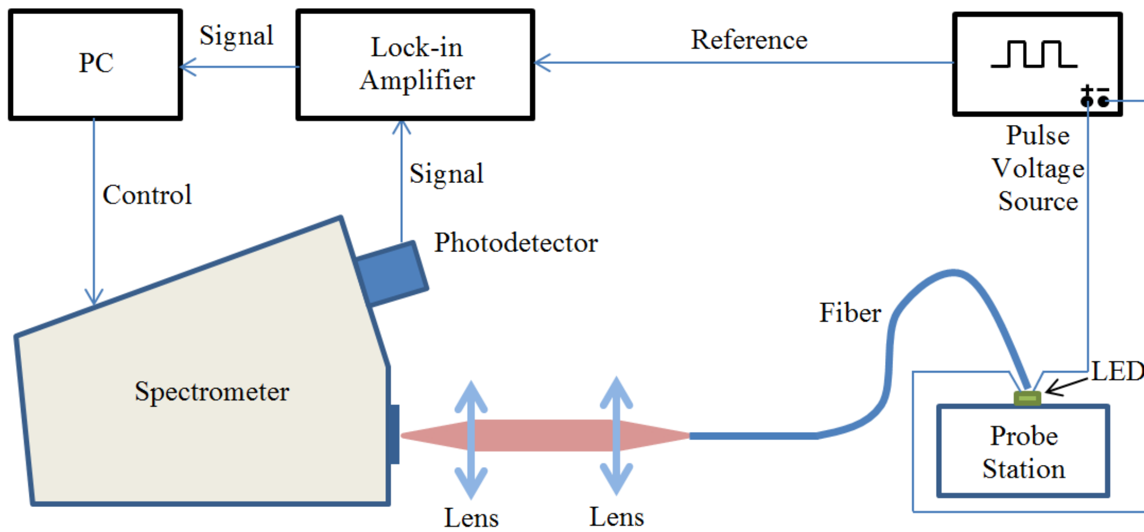

Figure 29: Schematic diagram drawing of EL measurement setup.

EL spectrum with different current injection was tested using changing voltage offsets. Figure 30 and Figure 31 show the spectra of changing the current density level. In this case, thermoelectric cooler was used to keep the device temperature at 20 ˚C. Emission peak position corresponds to the bang gap in GeSn layer. For emission peak position, 0.645 eV and 0.601 eV was observed for 6% and 8% Sn device respectively. EL of 9% and 10% Sn sample were also

measured with the emission peak positions of 0.538 eV and 0.528 eV respectively, Figure 32. The highest emission peak wavelength of 2348 nm (0.528 eV) was observed for 10% Sn LED.

In EL, the carriers are injected by adding electrical field onto device causing electrons and holes movement. Similar to PL, where carriers are introduced by the photon illumination, the carriers flowing between the band gap and radiative recombination happened when the electrons and holes have the same momentum. For a direct band gap material, the minimum of the conduction band have the same momentum with the maximum of the valence band. Radiative recombination will cause a light emission with the photon energy near the band gap. Compared to the PL result, the 6% and 8% GeSn n-i-p structure have the same emission spectrum profile, Figure 33.

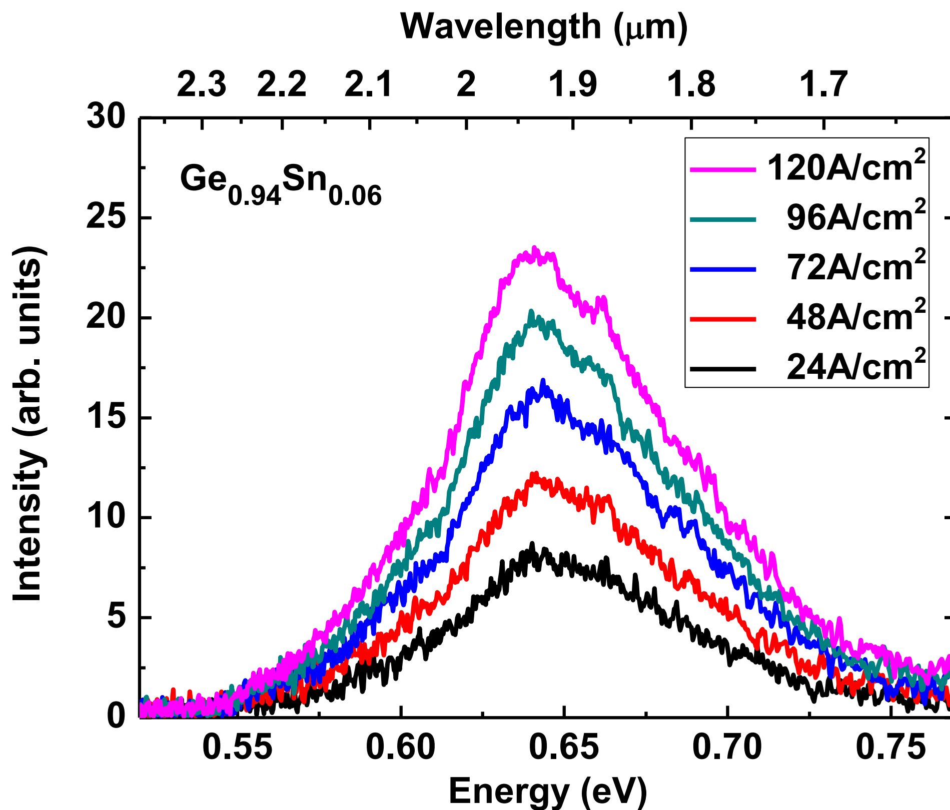

Figure 30: EL spectra with various current injection 6% Sn 1st Generation LED [17].

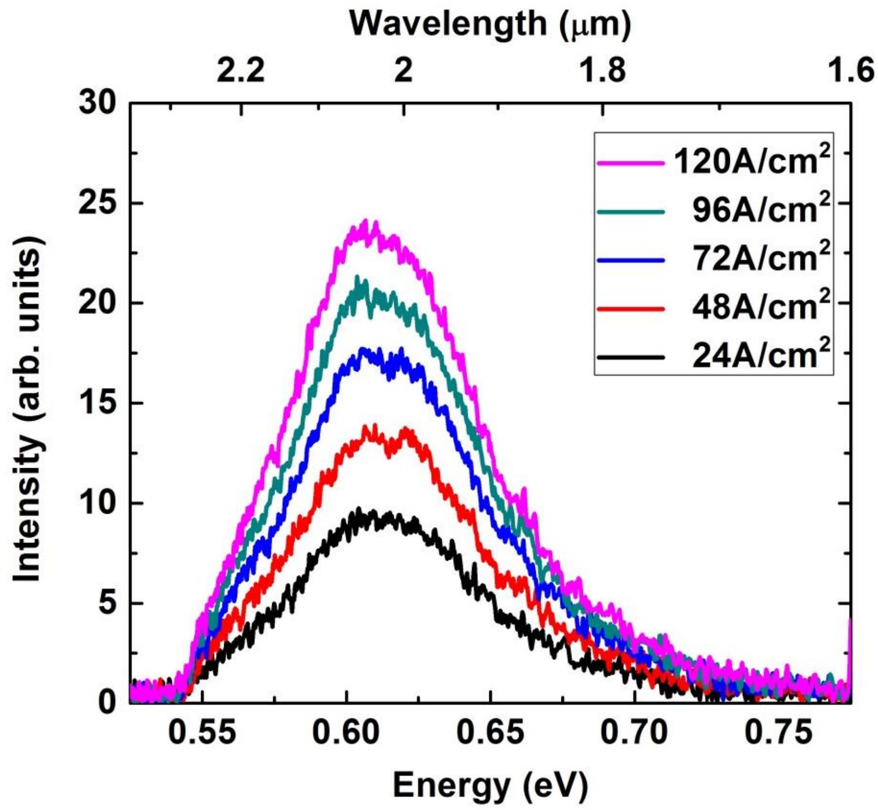

Figure 31: EL spectra with various current injection (a) 6% Sn; (b) 8% Sn composition [17].

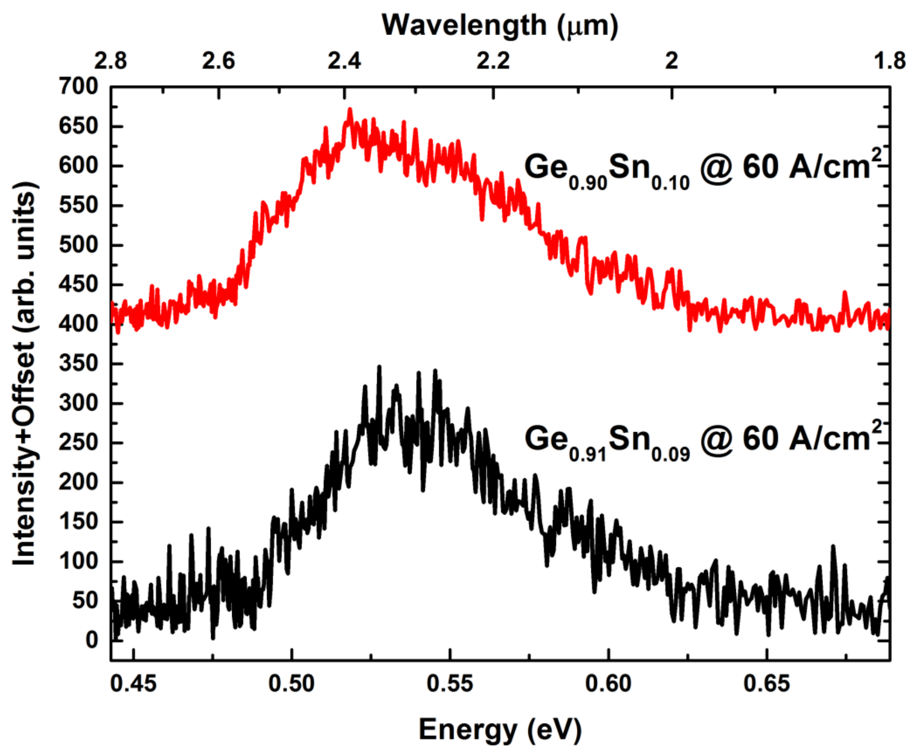

Figure 32: EL spectra of 9% and 10% Sn LEDs.

The emission intensity is described as follows [44]. Photon exited carrier and electrical injected carriers are used the density of state can be calculated as

$$\rho(\mathrm{E}) = \frac{1}{2\pi^2}\left(\frac{2m_r^*}{\hbar^2}\right)^{\frac{3}{2}}\sqrt{E - E_g} \quad \text{(Equation 2)}$$

where m_r^* is the effective mass, $\hbar$ is the plank constant, E is the energy, and E_g is the band gap. From the Boltzmann distribution, the carrier is distributed by

$$\mathrm{f(E)} = e^{-E/kT} \quad \text{(Equation 3)}$$

where k is the Boltzmann constant, T is the temperature. The emission intensity is proportional to the product of density of state and the distribution of carriers. As a result, the relation between emission intensity and energy is

$$\mathrm{I(E)} \propto \sqrt{E - E_g}\,e^{-E/kT} \quad \text{(Equation 4)}$$

For room temperature EL, the peak position of a theoretical LED emission spectrum is

$$\mathrm{E}_{peak} = \mathrm{E}_g + \frac{1}{2}kT \quad \text{(Equation 5)}$$

Temperature would affect the emission peak position. Therefore, temperature controller is used to keep the sample from joule heating.

Optical power is one of the characteristics for light-emitting devices. The result can be used for calculating the efficiency of the device. Using the ratio between optical power output and the power consumed by the resistance, we could estimate the efficiency of the light emission. Thermal electrical (TE) cooler was used to control the temperature of the device, shown in Figure 34. 20 ˚C was maintained for 10 min before every measurement. Optical power is shown in Figure 35. The current became linear after 60 mA with the current increasing. Thermal heating was a key factor of the error source since the power meter measure all the wavelength ranging from 0.1 μm to 10 μm. Thermal heating in mid and far infrared may also

counted into the optical power. Pulse measurement is expected to perform in the future to eliminate most of the heating effect.

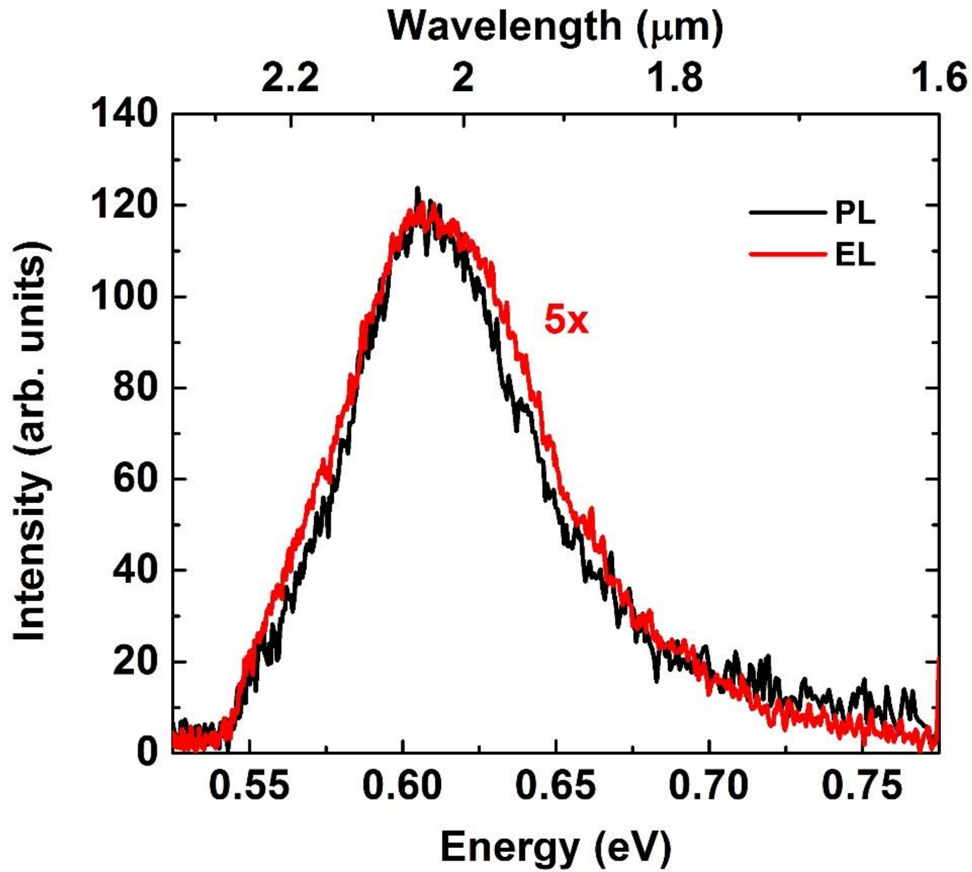

Figure 33: Spectra between PL and EL of 8% Sn sample.

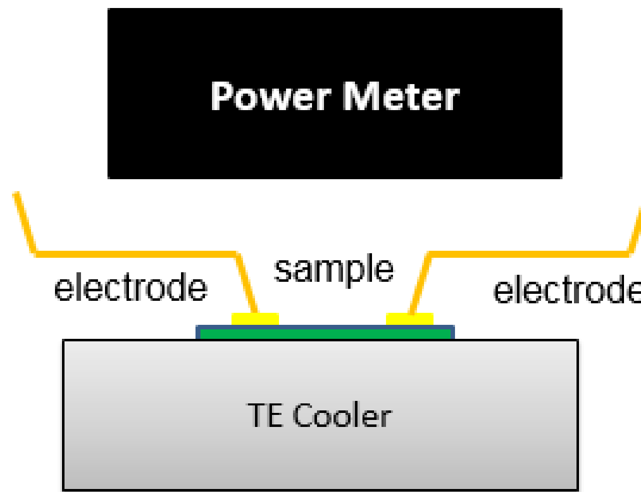

Figure 34: Schematic diagram of optical power measurement.

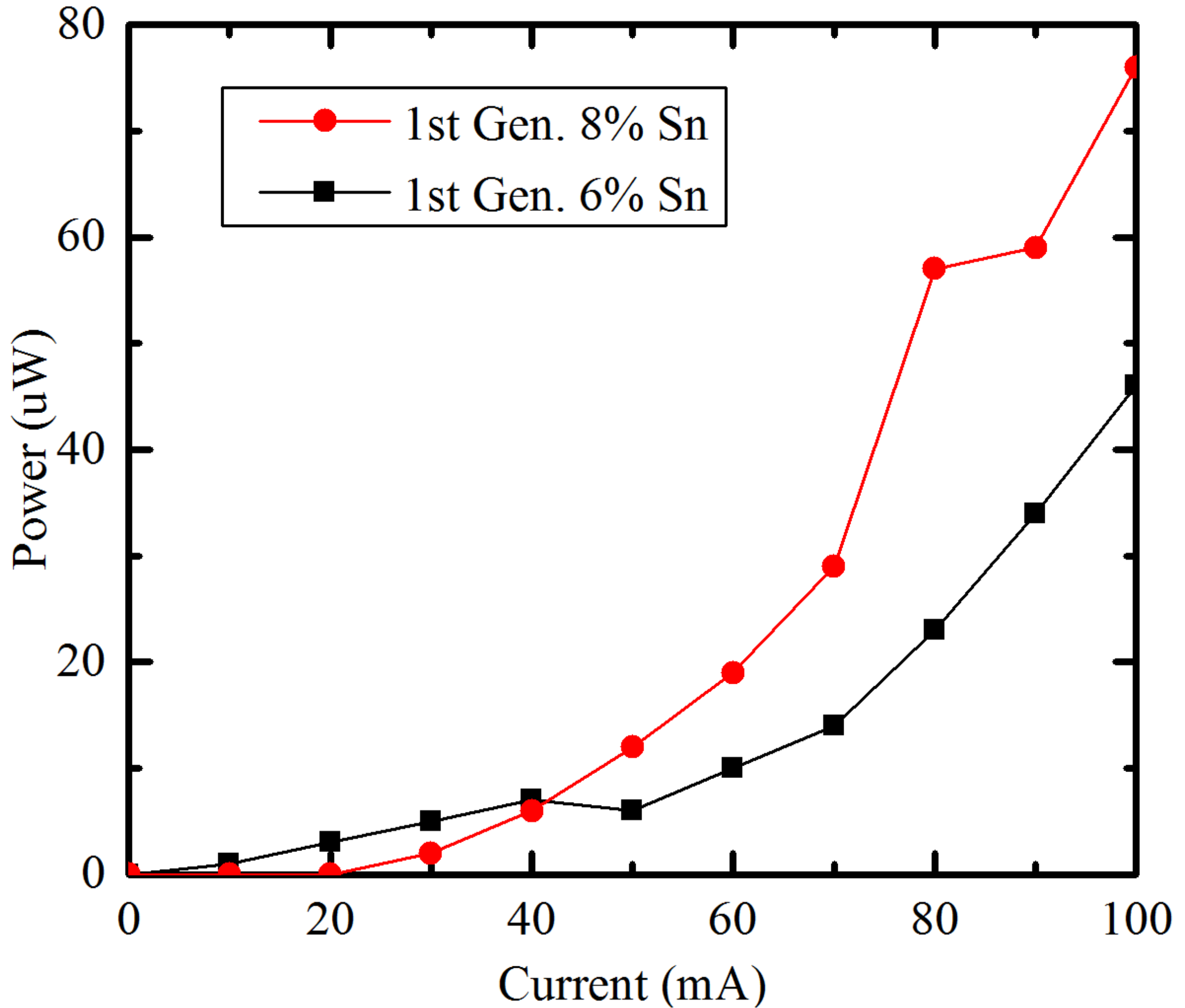

Figure 35: Optical power of 6% and 8% 1st generation LED

3.3 Second Generation Device

A new generation LED was designed for large metal pads for wire bonding. The device could be used for temperature dependent EL measurement in a cryostat. Wire bonding is preferred to enable bonding all devices into the cryostat and switch the device externally instead of only use probes for only one device for one measurement. The mesa was therefore changed to a round shape with a minimum diameter of 100 μm shown in Figure 36. Contacts were connected to larger pads deposited on an oxide layer.

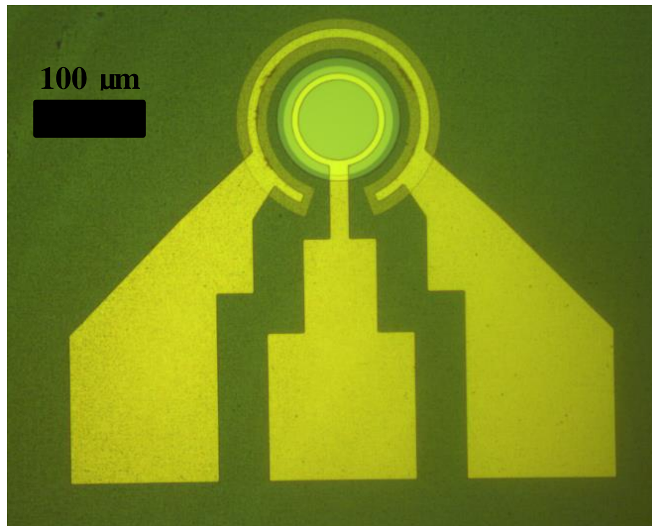

Figure 36: Optical top image of second generation LED.

To achieve this structure, an oxide deposition and oxide etching should be added between mesa etching and first negative photolithography process. Plasma enhanced CVD (PECVD) is a common method for thin film deposition. PECVD was used to deposit 100 nm SiO_2 on the sample. SiH_4 and N_2O were used for the SiO_2 formation and controlling the He for a better gas flow. Sample was set on a radio frequency power electrode in a vacuum chamber. While flowing the gas, the RF power will create the plasma above the sample for the oxide deposition. The plasma will not only create more radicals from the precursor and but also use electric field above the sample to generate a firm ion bombardment. As a result, reaction will therefore be more efficient and the deposited film will have a good quality.

Right after the oxide deposition, a negative photolithography process was used to define opening windows for the metal contacts. Descum was also followed after photolithography. To remove the oxide from the defined window, chemical wet etch was used with BOE solution using the concentration with BOE:H_2O=5:1. The BOE solution contains NH_4F and HF as the reactant to etch the oxide layer. As the oxide was opened, the negative photolithography could perform and the metal contacts could be deposited thereafter.

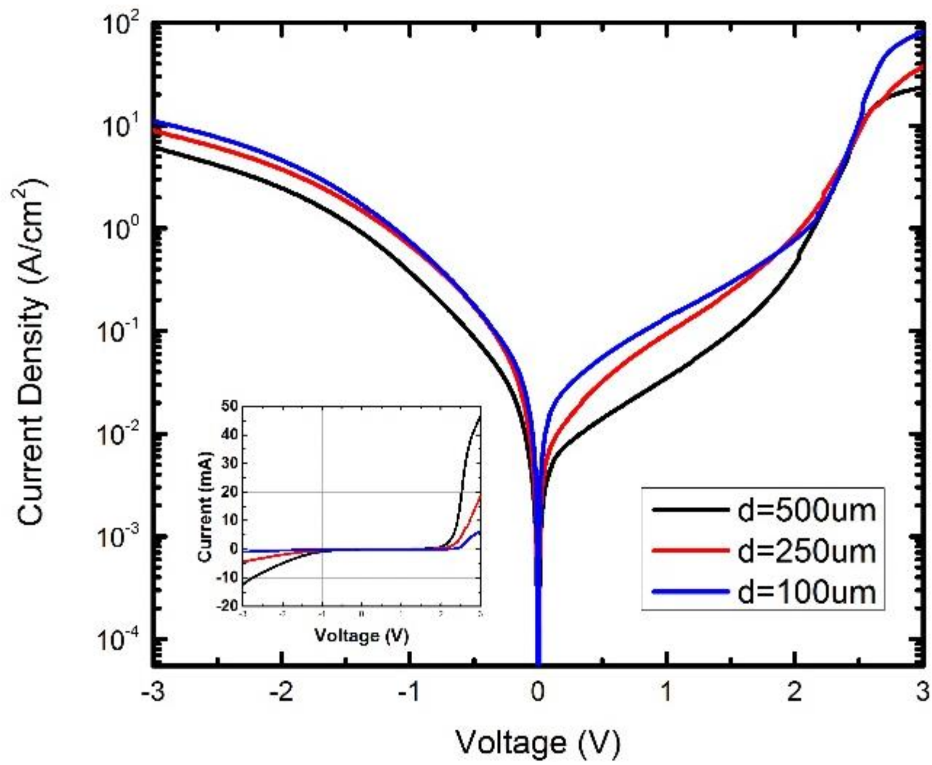

Figure 37: IV for 2nd generation 6% Sn LED.

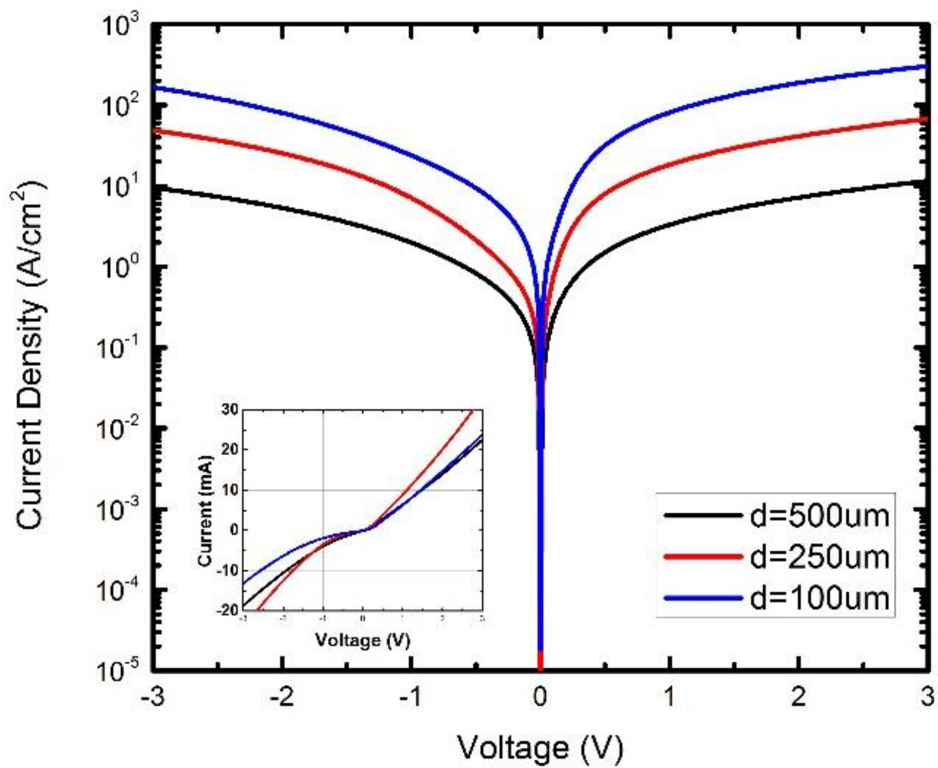

Figure 38: IV for 2nd generation 8% Sn LED.

For the EL, devices behaved normally and agreed with the first generation devices, Figure 39 and Figure 40, compared to Figure 30 and Figure 31. A higher current injection is shown here with higher reading compared to previous device results. Rising current density will significantly increase the optical output from the EL. A small tail on 6% Sn was observed. This was because of Ge layer. Previous device did not have such high current density. So the small "tail" could not be monitored. On wafer EL was characterized under the 20˚C with the TE cooler. However, a thermal effect from the high current injection resulted in a slight red shift for the peak positions. Optical power was then measured using power detector shown in Figure 41. The optical power turned out linearly after 60 mA.

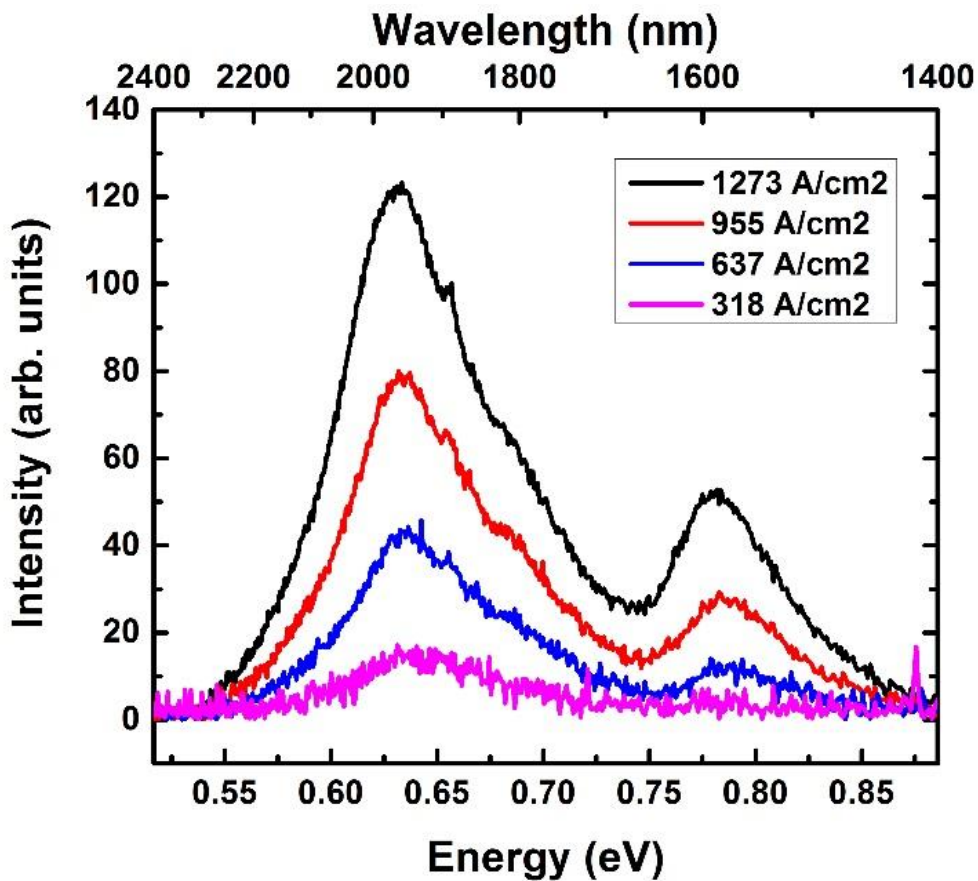

Figure 39: EL spectra of 6% Sn 2nd generation LED.

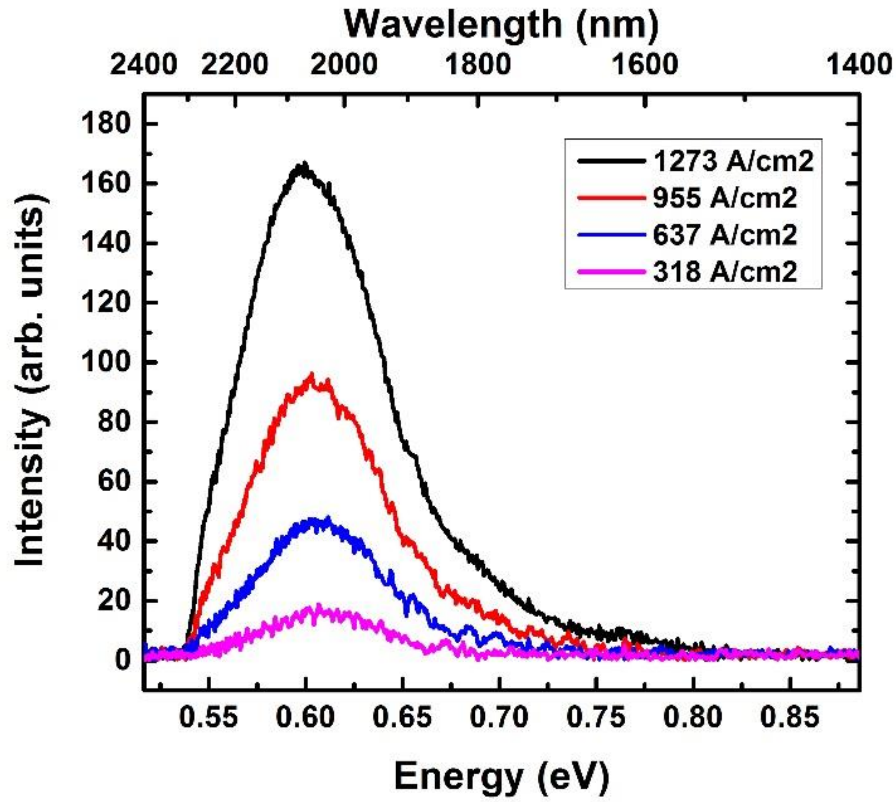

Figure 40: EL spectra of 8% Sn 2nd generation LED.

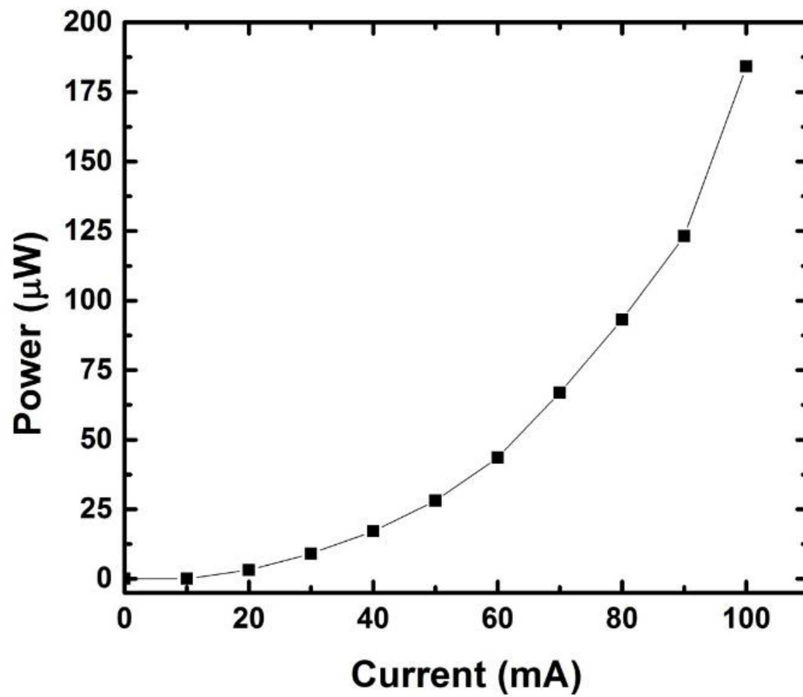

Figure 41: DC optical power for 8% Sn 2nd generation LED.

Wire bonding was performed using Au wire connecting the devices to a 24 pin chip carrier. For a fabricated sample with dimension of 1 cm^2, a dicing process was performed to cut the sample into a smaller size to fit the chip carrier holder. Thermal conductive epoxy with curing was used for the adhesion between the sample and carrier holder. Au wire was then bonded using the ball bonding method under thermal heating and ultrasonic. A bonded sample is shown in Figure 42. This bonded sample would be continued characterizing in the future work.

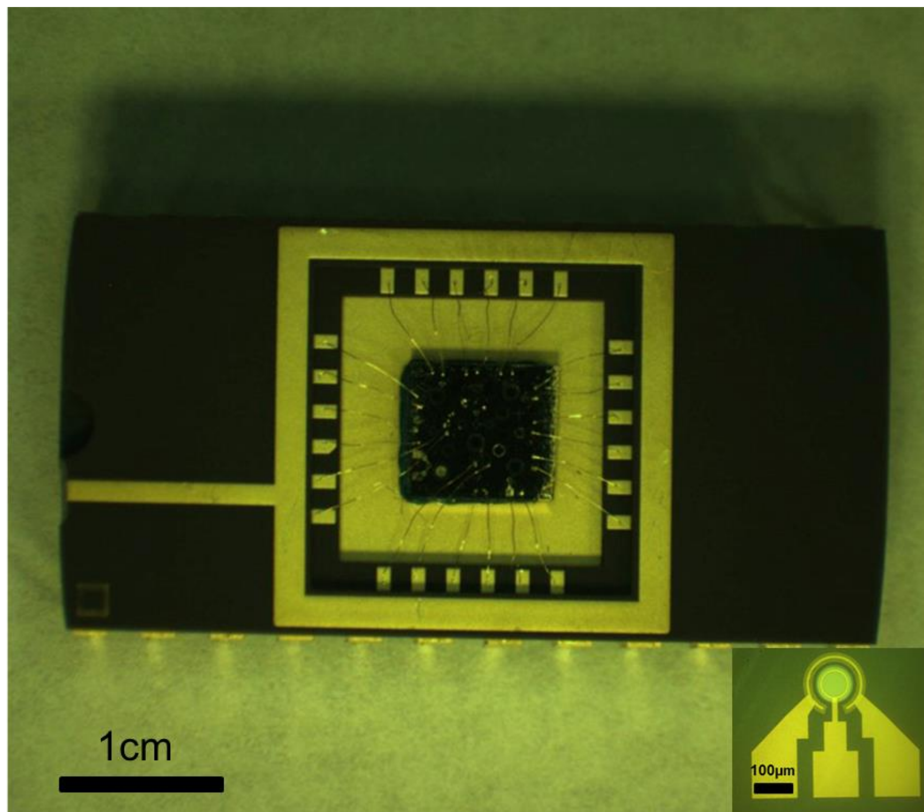

Figure 42: Optical image of bonded sample, top view.

3.4 Third Generation Device

The third generation device was fabricated aiming at the high optical power output. It was suspected that current crowding may take place in the first generation LED devices. The output might not sufficient enough. Current will only flow from the edge of the sample so that most of the area in the center was not in the path of flowing current. In order to solve this

problem, we optimized the contact design with a net structure. As a result, the current flowing from the device will be uniformly distributed. The fabrication process was very to the first generation device. Yet the liftoff for the n-contact should be handled carefully in order to have a good turnout for small features.

IV was measured using the probe station, the rectify behavior was observed. And compare to the first generation device, the current was higher due to the current uniformly distributed. EL measurement was observed with decreased signal intensity. This could be the effect of current spreading and therefore decrease the current density. Even though the working area of the material was increased, the current density drop more than the improvement from it.

EL from the third generation device was compared with the first generation in Figure 43. As a result, emission peak remains the same, but the emission intensity drops.

All generation optical power were eventually collected and compared in Figure 44.

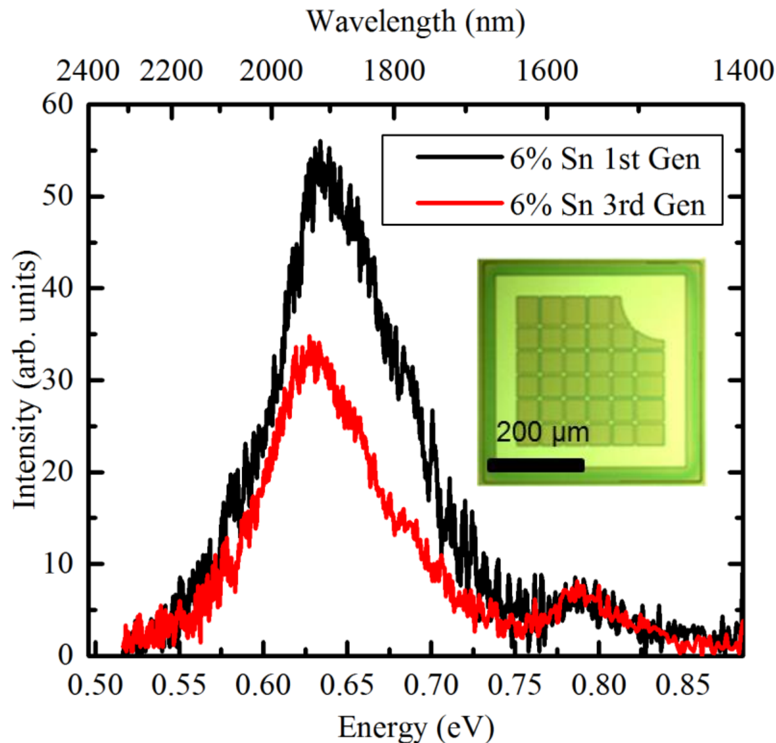

Figure 43: EL spectra from 6% Sn LED with 1st and 3rd generations.

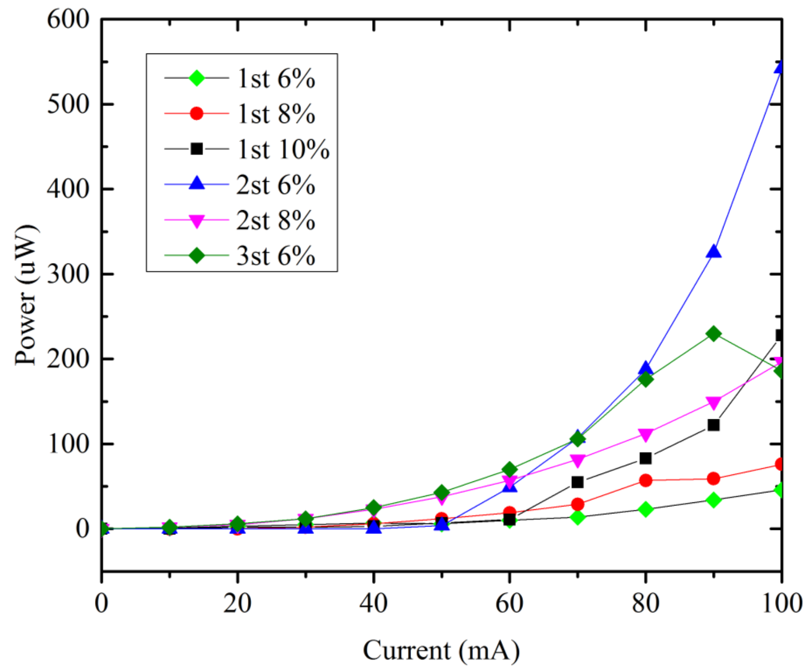

Figure 44: DC optical power for all fabricated LED devices.

Chapter 4: Edge-Emitting LEDs

4.1 Introduction

In this chapter, DHS was fabricated into edge-emitting device. Edge-emitting LED was the first attempt for this goal with an optical confinement for the light. Edge-emitting LED emits light from the side facet of the device. Together with DHS, the device will have both electrical confinement for the carriers and the optical confinement for the light. For the optical confinement, the air/GeSn/air sandwich structure will form a difference in index of refraction, shown in Figure 45. Therefore, light propagation in the cavity will be mostly confined within the material, shown in Figure 46. Also, if we cleave the sample vertically from the strips to form flat facets from both sides. These two flat side walls will work as optical mirrors that reflect the light in the material. In this case, and optical cavity is formed.

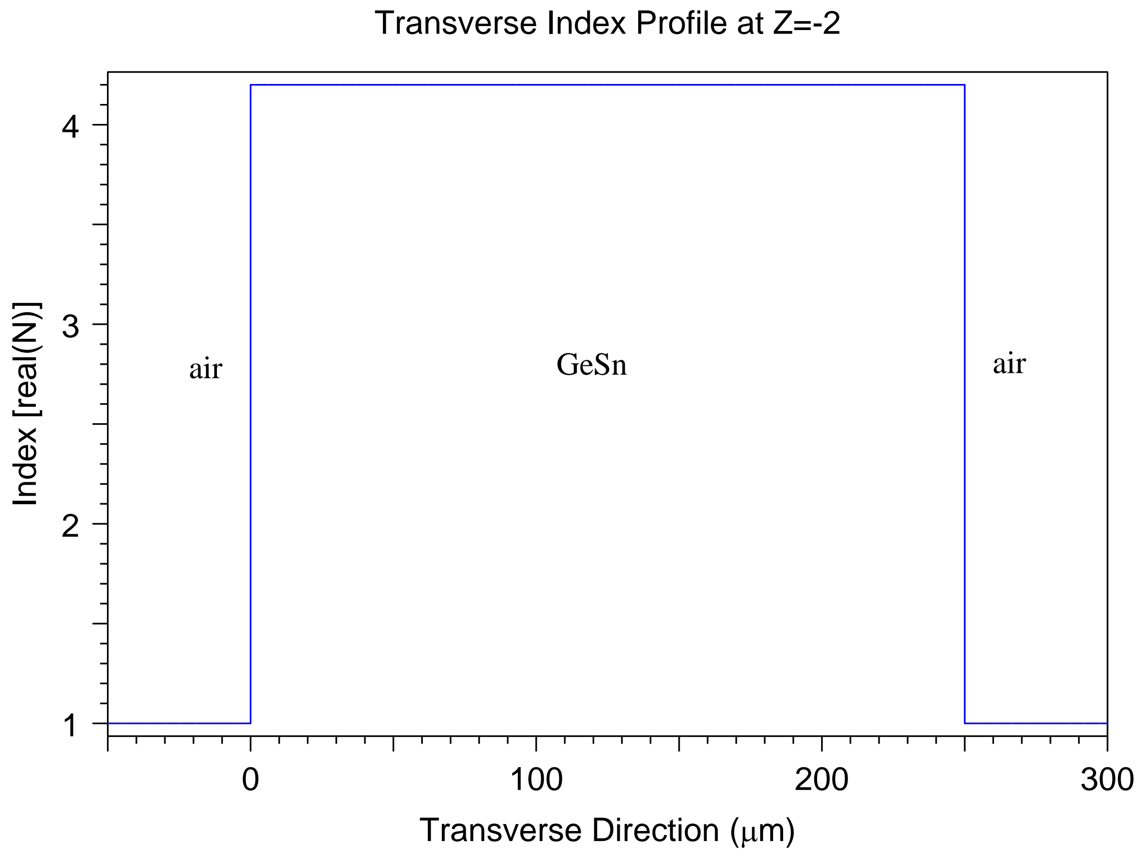

Figure 45: Refractive index of GeSn layer along the ridge.

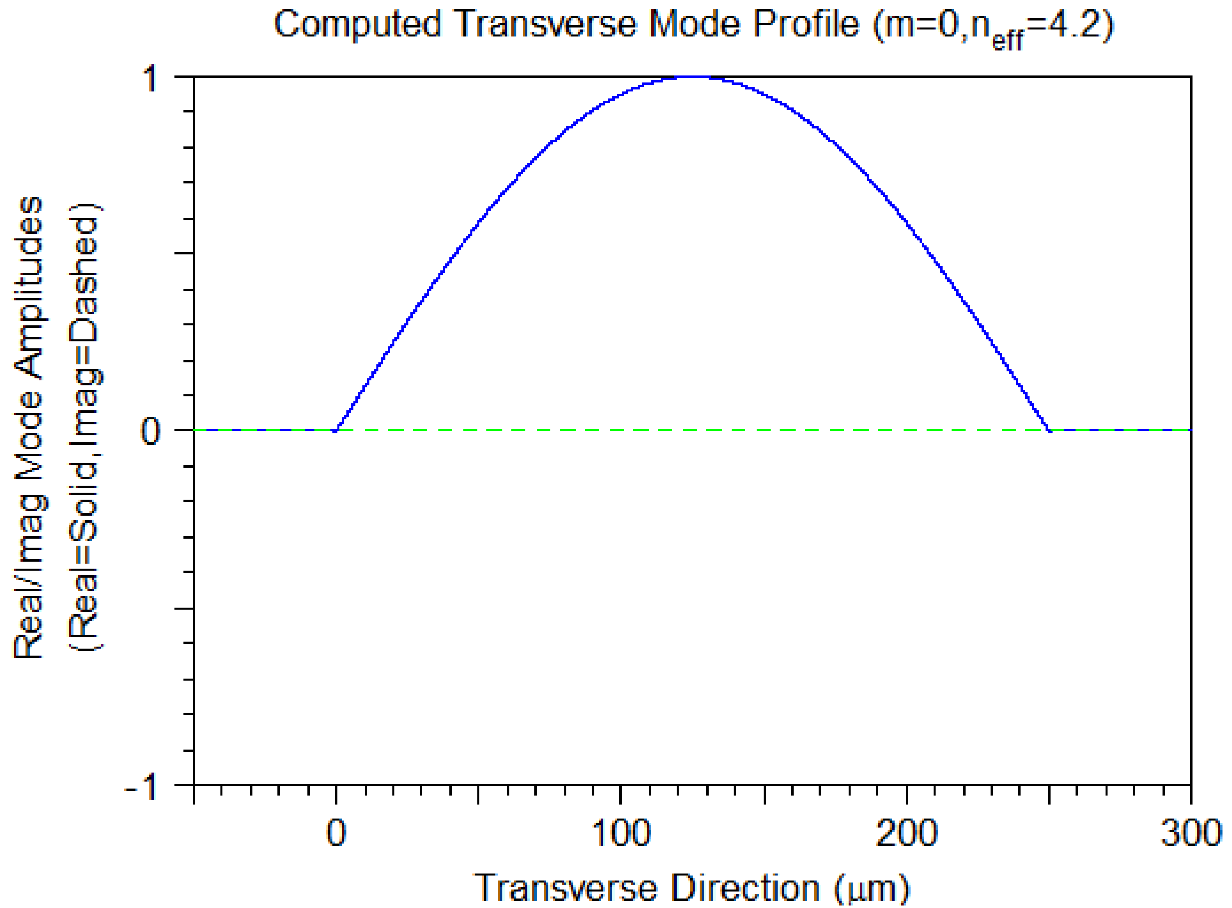

Figure 46: Calculated light profile for GeSn layer.

4.2 Device Fabrication

The fabrication of this device was similar to the surface emitter. Starting with the same DHS structure used for the surface-emitting LED, the fabrication process is shown in Figure 47. The device was formed as stripes mesa. A steep side wall was desired for a good light confinement. Therefore, RIE was used for this purpose. The sample was etched from the Ge cap layer down to Si substrate, leaving DHS isolated as a strip dimension. After the mesa was formed, a 100 nm SiO_2 layer was deposited directly by PECVD to eliminate the dangling bond from the side wall so that the surface recombination was reduced. Once the SiO_2 passive layer was deposited, a negative photolithography was performed to define the opening window for the

metal contacts. Descum was performed after photolithography for eliminating the undeveloped photoresist remaining in the opening area. The BOE solution was used to etch the passive layer to opening. Once the contact window were opened, metal deposition was performed for the top contacts. A 10 nm Cr and 200 nm Au were deposited on top as n-contact and a liftoff was performed. Thereafter, the sample was processed under lapping machine to thinner the Si substrate down to 90 μm. A p-type metal contact was deposited directly back on the Si substrate using thermal evaporation with 500 nm Al.

To make the flat surface from the cleaving facets, it would require the Si substrate naturally break along its crystal orientation. A 200 mm Si wafer had the thickness of 750 μm, which made it so difficult to cleave for silicon with a flat cleaving facet. Also, to reduce the series resistance of the edge-emitting LED device, the thickness of the Si substrate should be reduced. Therefore, a lapping process to thinner the substrate would help us not only get atomic flat cleaved surface, but it will reduce the series resistance on Si substrate. The lapping process was a physical process that would reduce the substrate thickness, shown in Figure 48. Sample was set on a glass substrate downwards for lapping. 15 μm Alumina powder was used for making the slurry to make the abrasive between the sample and the ion plate. The grooved iron plate rotates with a controlled speed and cause the sample surface physically scratched by the abrasive and its thickness was therefore reduced.

After lapping, the back surface was deposited Al for the p-contact using metal deposition. To form the final device, the long strip of mesas will be cleaved into short strips (200 μm). Atomic level flatness should be achieved and checked using SEM. Shown in Figure 49, the edge-emitting LEDs were cleaved with the cavity length of 250 μm and with the ridge width of 20 μm, 40 μm, 60 μm, 80 μm, and 100 μm.

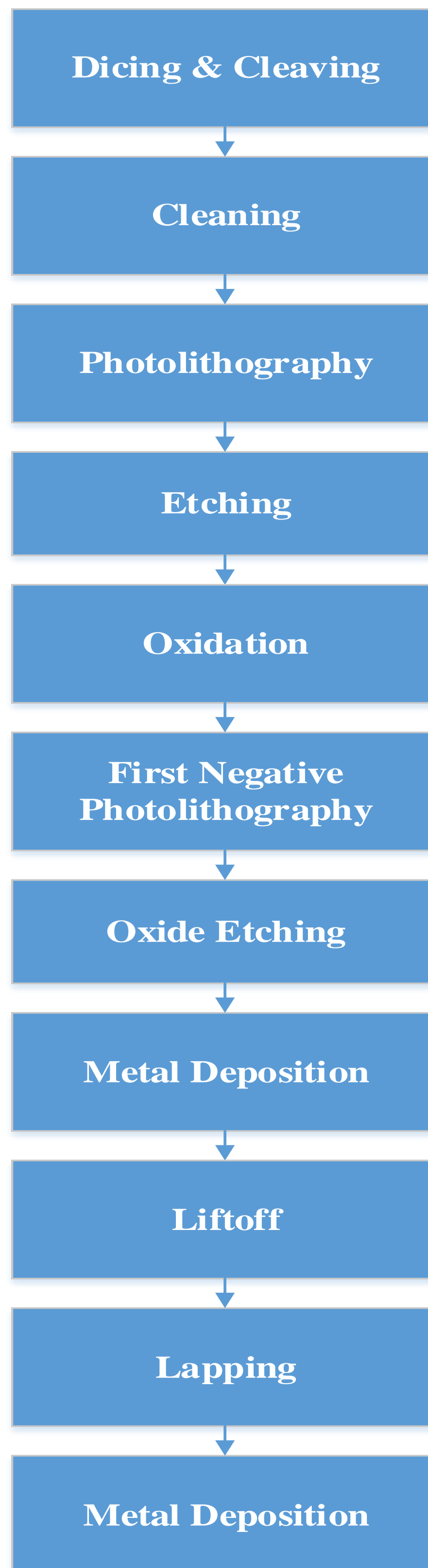

Figure 47: Process flow of edge-emitting LED fabrication.

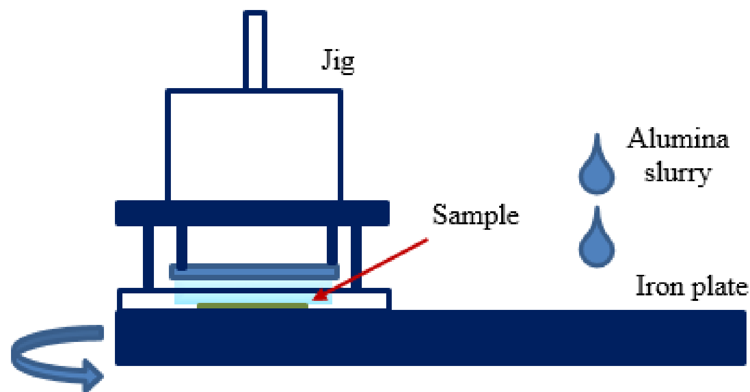

Figure 48: Schematic diagram of lapping process

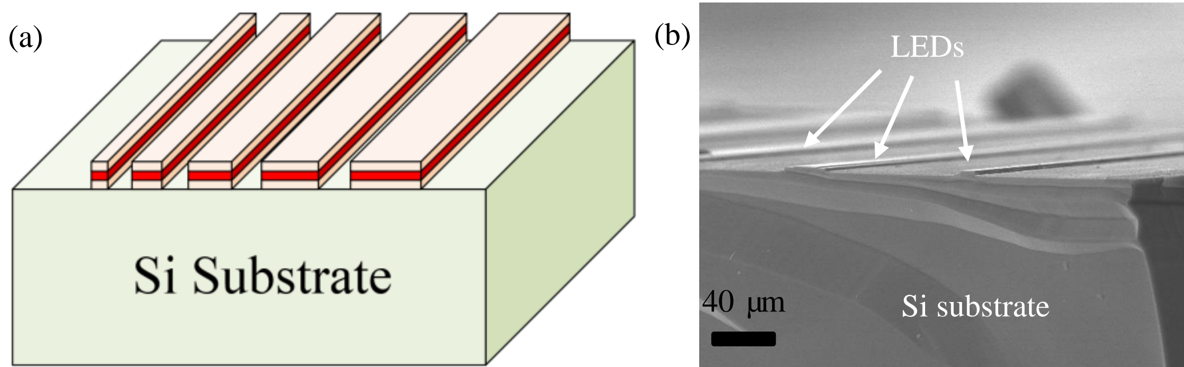

Figure 49: (a) Schematic diagram of cleaved n-i-p edge-emitting LED, and (b) SEM image.

4.3 Device Characterization

IV measurement was measured under voltage applying between the n-type Ge cap layer and p-type Si substrate. The IV behavior is shown in Figure 50 and 51. The ideal structure was the Si substrate to be highly doped. However, the p-i-n structure was grown on a low doped substrate. Therefore, Si substrate had a relatively high resistivity. In addition, aluminum contact will form a Schottky barrier with Si and cause the rectifying effect. This rectifying effect was dominating the IV curve as two diodes back to back connecting. In this case, the IV curve was affected by the Schottky diode and the p-i-n junction.

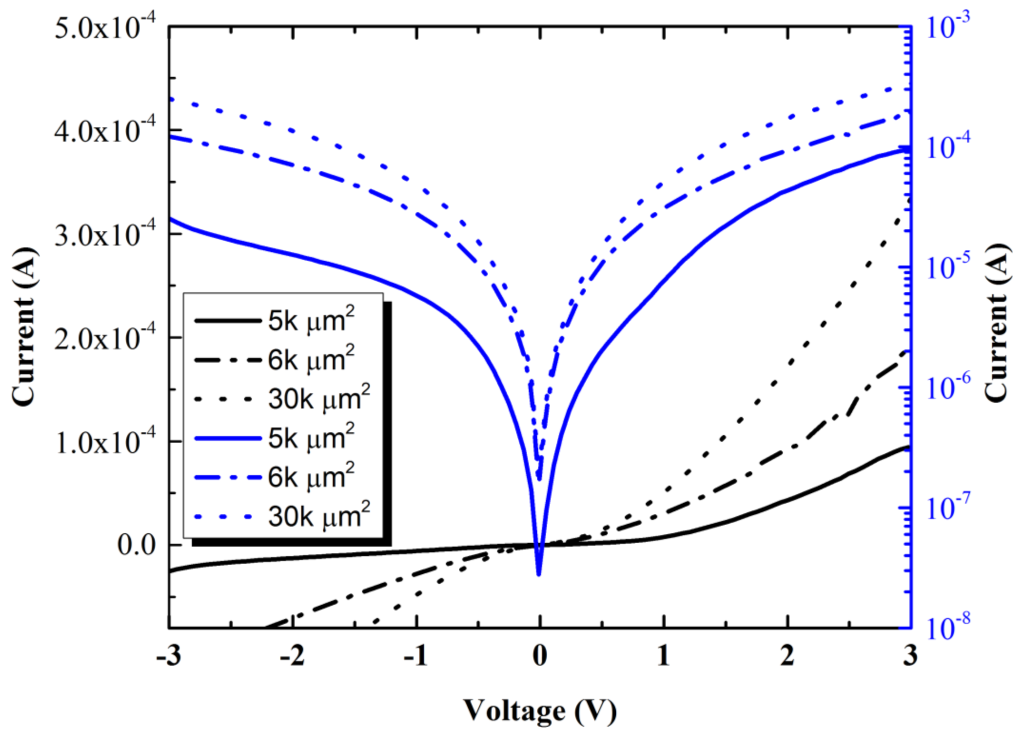

Figure 50: I-V for 6% Sn edge-emitting LED.

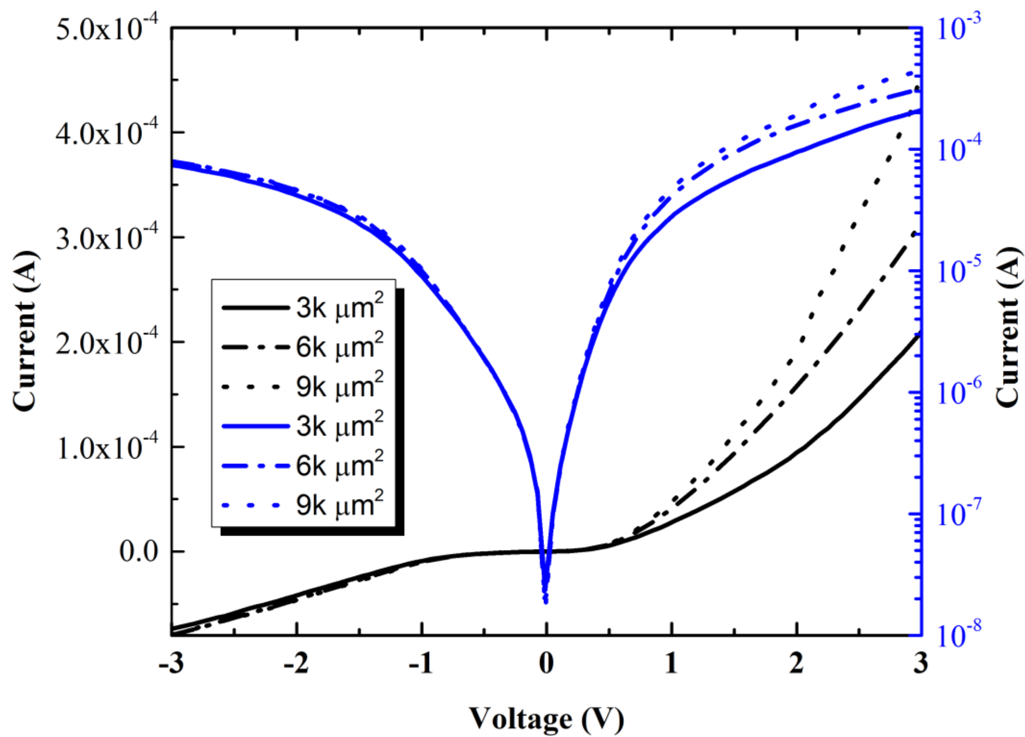

Figure 51: I-V for 8% Sn edge-emitting LED.

The EL spectra was measured for 6% and 8% Sn edge-emitting LEDs. The spectra were different from the surface-emitting LED. Several reasons may contribute to the disagreement. First of all, for high current injection, the DHS could not confine all the carriers. The light emission may resulte from other regions than only the GeSn layer. Second, the low doped Si substrate may form the Schottky barrier. Due to the reverse bias on Schottky diode, the series resistance becomes larger for LED device. When applying large current injection, joule heating will increase the device temperature. The thermoelectric cooler did not provide enough power to keep the sample at the room temperature. As the same time, heating will cause the contact degradation so the device performance was not unstable. Furthermore, optical power could not be accurately measured since the black body radiation. A primary results are shown in Figure 52 and Figure 53, further confirmation was preferred to confirm these results.

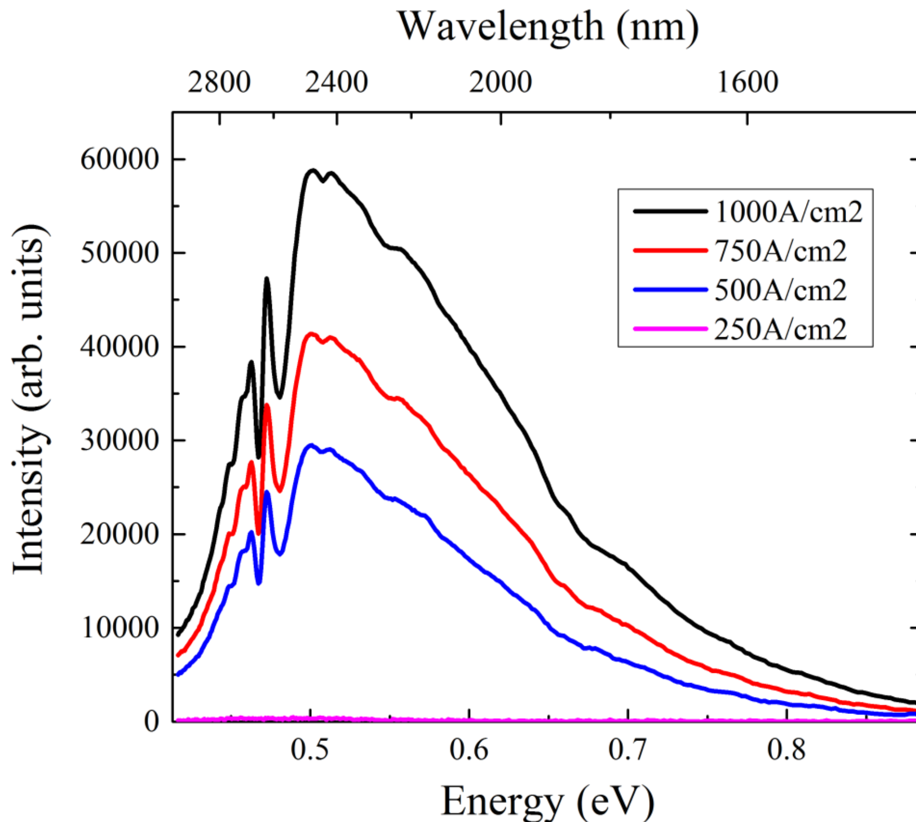

Figure 52: EL spectra of 6% Sn edge-emitting LED.

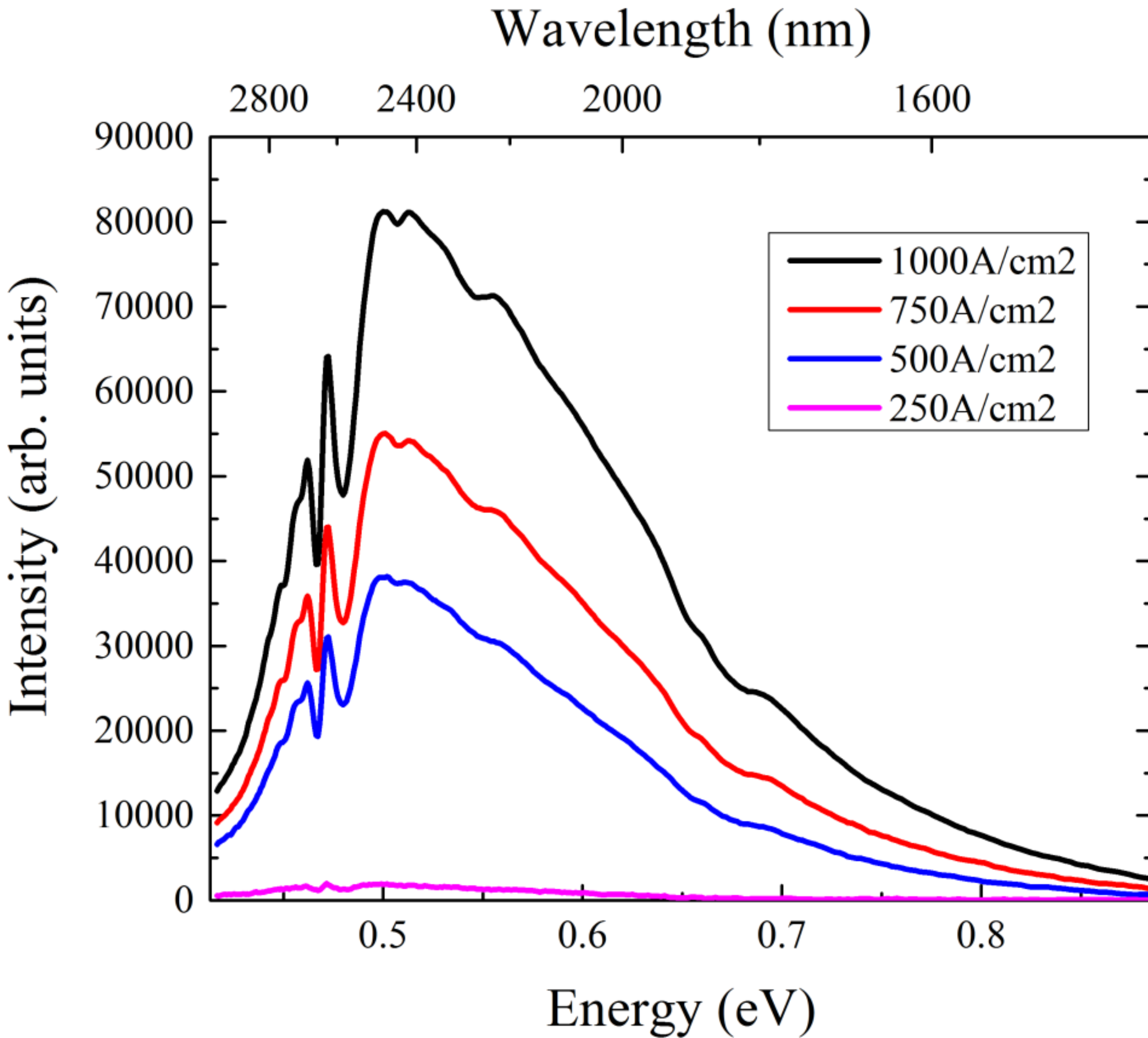

Figure 53: EL spectra of 8% Sn edge-emitting LED.

Due to the resonance of the light in the cavity, some of the EL spectrum indicates some emission spikes which could be the potential modes with poor performance, shown in Figure 54. Since the cleave facets did not turn out perfectly flat, this mode result remains unstable. The insert is the energy of the selected peak values for marked positions which shows a linear trend. Further investigation should proceed to confirm and understand this result.

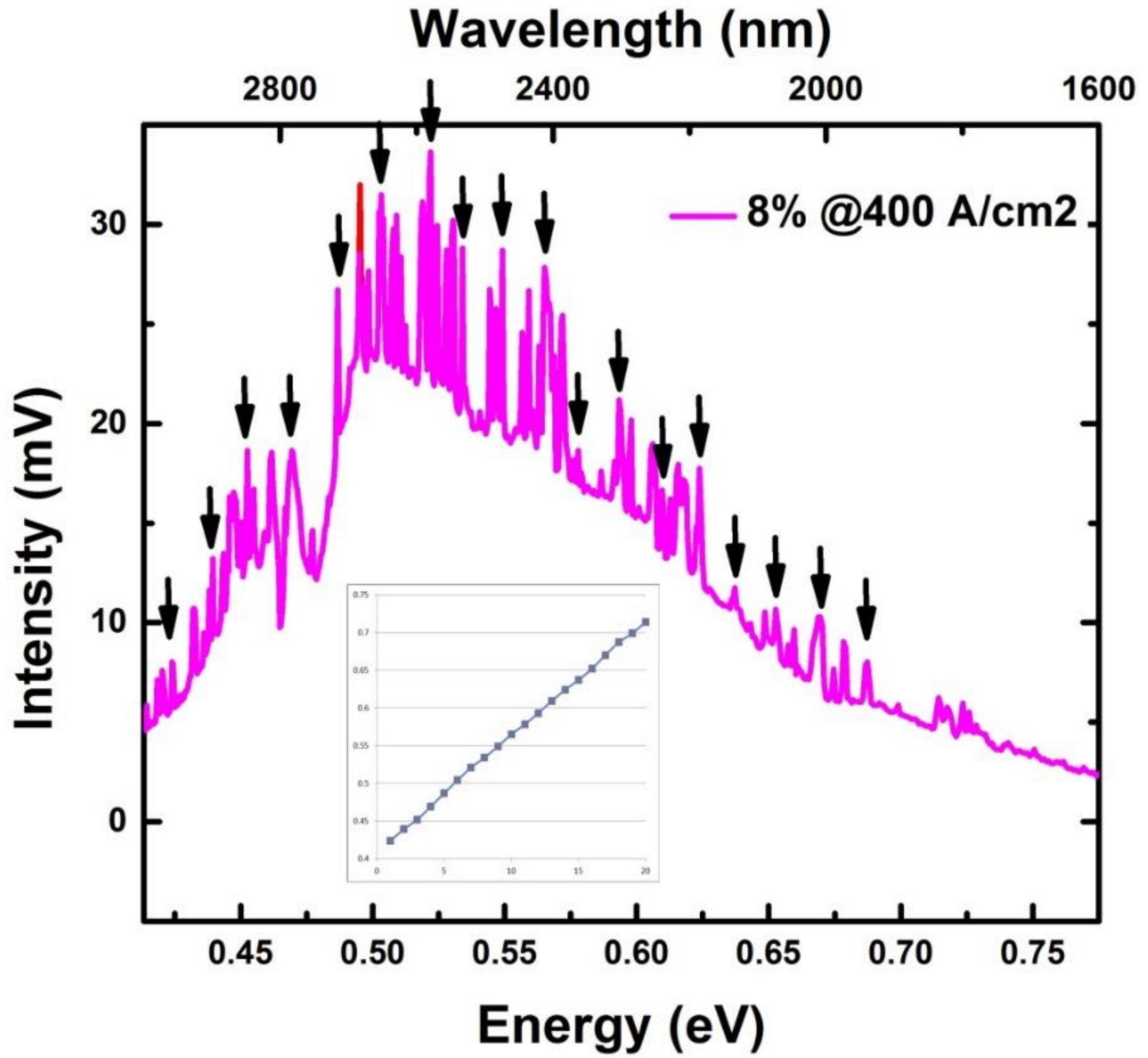

Figure 54: EL spectra for 8% Sn edge-emitting LED with spike peaks.

Chapter 5: Light-Detection

5.1 Introduction

GeSn based photodetector is discussed in this chapter. GeSn photodetector can cover from near to mid infrared range due to the material band gap. Also, it can be monolithically grown and fabricated on Si substrate. These merits make GeSn photodetector competitive compared to Ge and InGaAs. Carriers will be generated from the photon injection when photon energy is larger than the band gap. Therefore, response spectrum could therefore reflect the band gap. Simple structure devices like photoconductor and photodiode operate with reverse bias. Photon generated the carriers were collected from electrodes, detected as photo current.

5.2 Device Fabrication

Photoconductor detector

The photoconductor sample structure was a Ge buffered GeSn thin film grown on Si substrate using ASM Epsilon® reduce pressure CVD (RPCVD). GeSn film with Sn composition of 0.9, 3.2, and 7 percent were grown for this study. Films thickness and doping concentration are given in Table II.

Sn%	GeSn Film Thickness (nm)	Ge Buffer Thickness (nm)
0.9	327	763
3.2	76	684
7	240	755

Table II: Information of GeSn photoconductor layer structure.

The photoconductors were fabricated using reactive ion etch to form mesa and then two metal contacts were deposited on GeSn mesa and Ge buffer layer. Metal contacts with 10 nm Cr and 200 nm Au was formed by thermal evaporator. The device structure is shown in Figure 55.

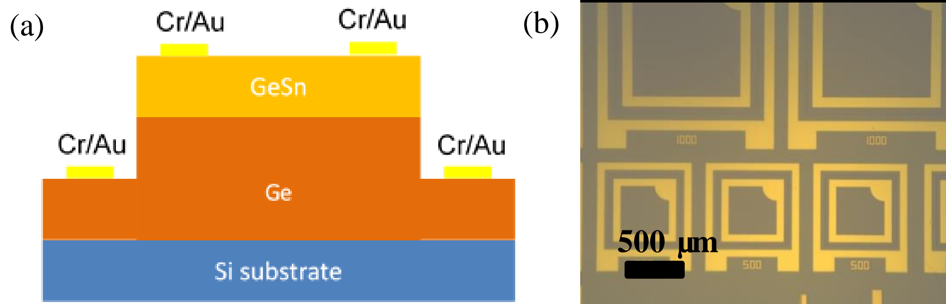

Figure 55: (a) Schematic diagram of photoconductor, and (b) optical image of top view.

Photodiode

Photodiodes were used from the 1st generation LEDs with mesa size of 2 mm by 2 mm.

5.3 Device Characterization

Photoconductor

Electrical properties were characterized by I-V measurement. Generally, for photoconductor, it should be a pure conductor without polarity. From IV characteristics of the fabricated devices, shown in Figure 56, the photoconductors behaved linearly in either forward or reverse bias, but had different resistances between the two bias conditions. This may mainly due to the heterojuction formed between Ge and GeSn layer. Since the unintentionally doped Ge and GeSn were both p-type, holes were the majority carriers contributing to the current. When two p-type material align, the valence band will form a barrier that could affect the holes transportation. When the forward bias added, holes will pass through the barrier with little resistance. However, when the current flowing in the negative direction, holes will be stopped by the offset in the valence band. Therefore, resistance is raised. The resistance was analyzed by comparing the difference of resistance between forward and reverse bias shown in Figure 57.

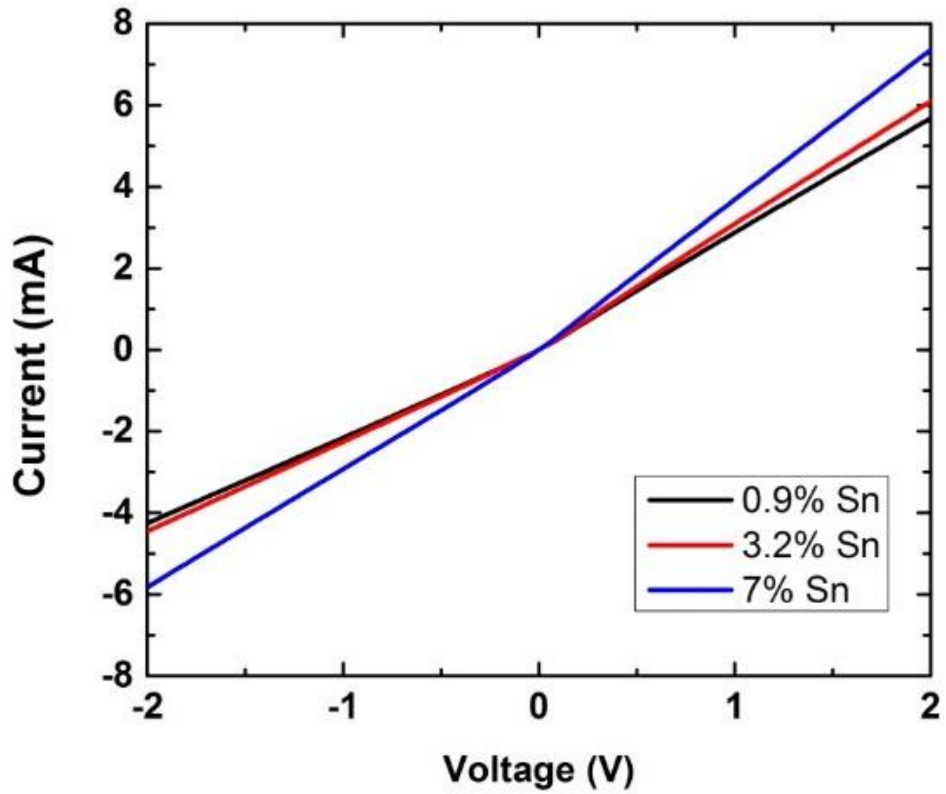

Figure 56: I-V for photoconductors with different Sn composition (2 mm mesa).

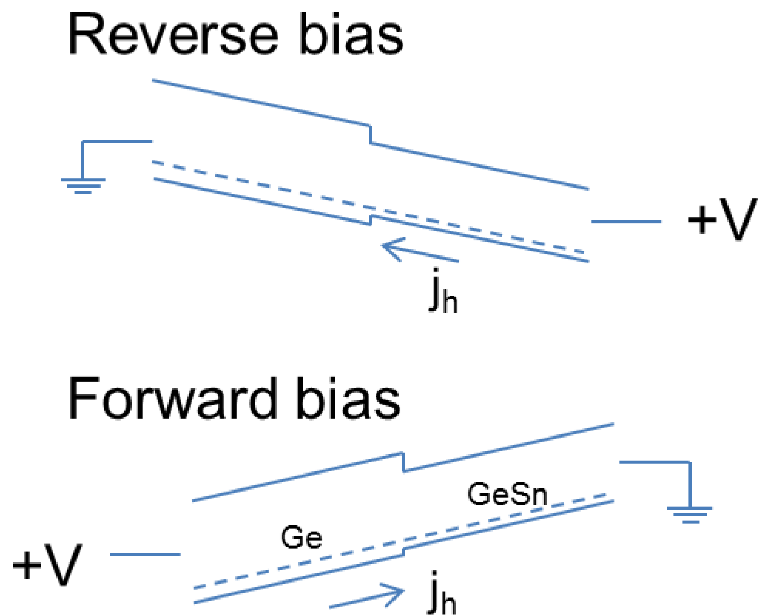

Figure 57: Band diagram of photoconductor operating under different electrical field direction.

Optical measurement was measured by using tungsten light source through Fourier transform infrared spectroscopy (FTIR) shining onto the sample. The sample was biased with a constant current. The current variation was then measured as the spectral response. Spectral response among photoconductors with various mesa sizes was measured, shown in Figure 58. The normalized position was the Ge buffer layer absorption. Compared to Ge absorption (<1550 nm), the mesa size improved the absorption area. Larger absorption was expected for device with larger area. Also, as Sn composition increased, the cutoff edge shift to the higher wavelength resulting a decrease of the band gap, shown in Figure 59.

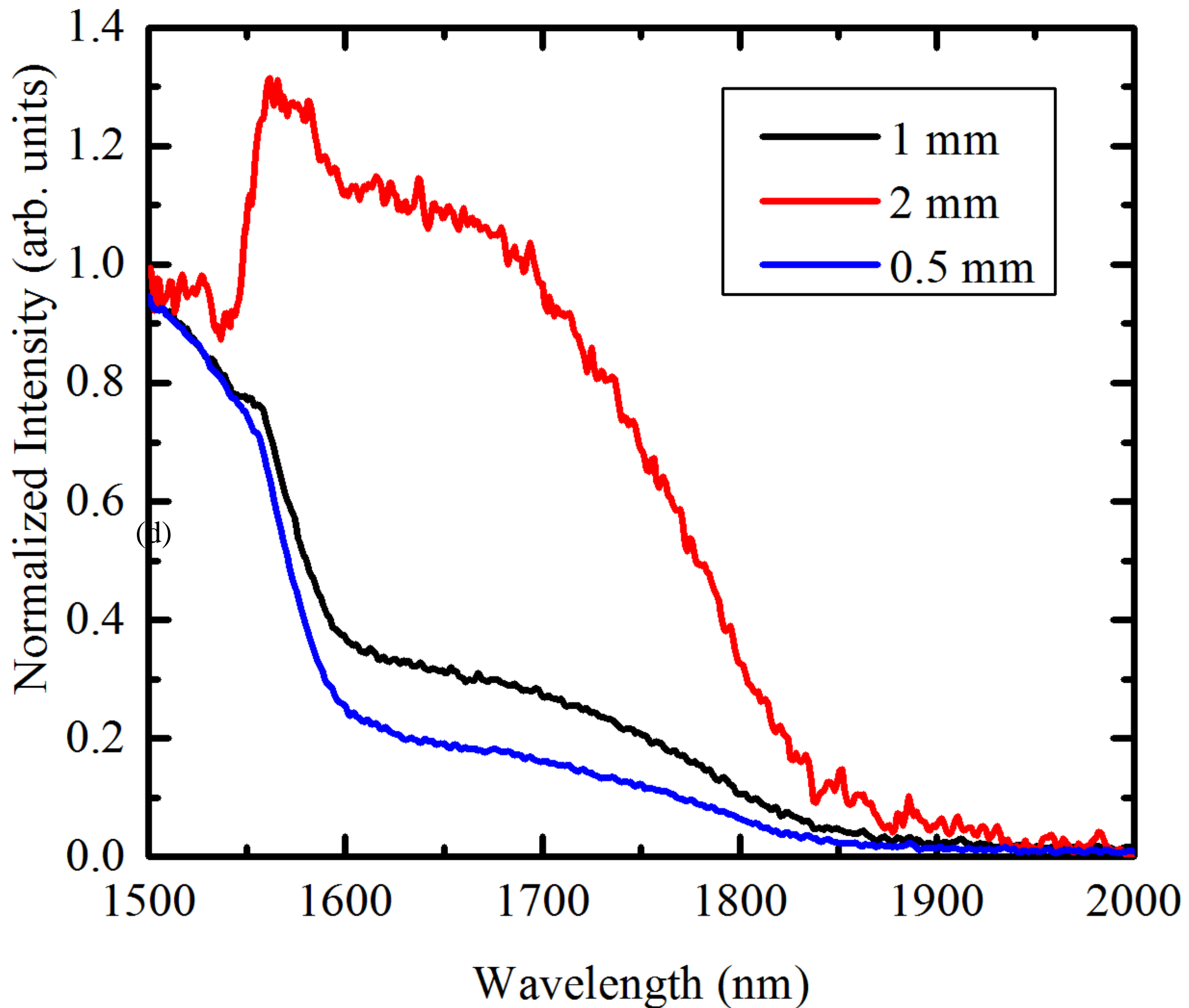

Figure 58: Spectral response of photoconductor with different Sn composition with different mesa size (length= 1 mm, 2 mm, and 0.5 mm).

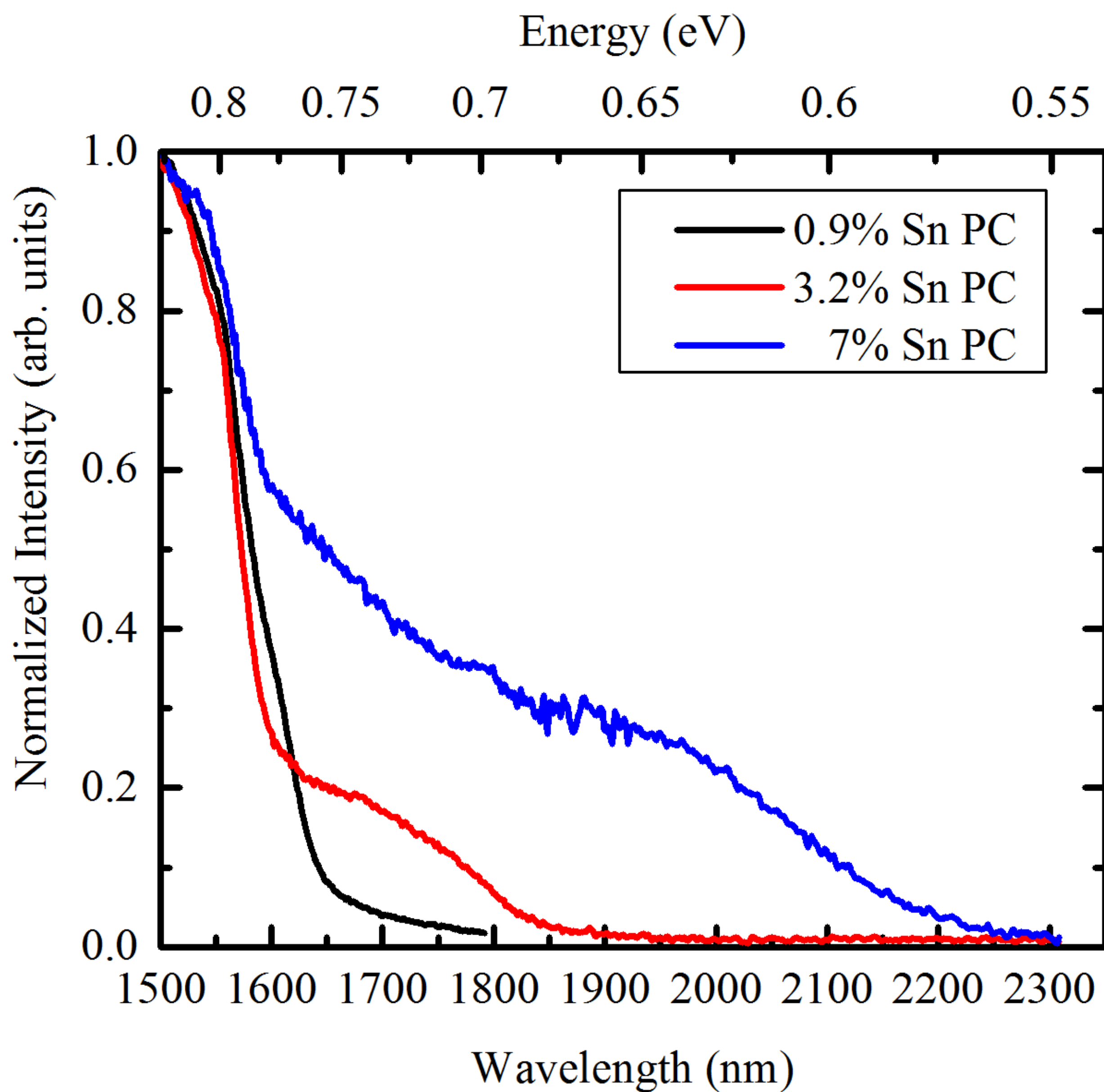

Figure 59: Spectral response for photoconductors with different Sn compositions.

The temperature dependent spectral response was followed using 7% Sn sample, shown in Figure 60. Device was under forward bias. Due to the thermally excited carriers in room temperature, response curve under room temperature (300 K) has larger noise level than at lower temperatures. The material band gap will shrink, resulting the response curve cutoff shifting towards smaller wavelength.

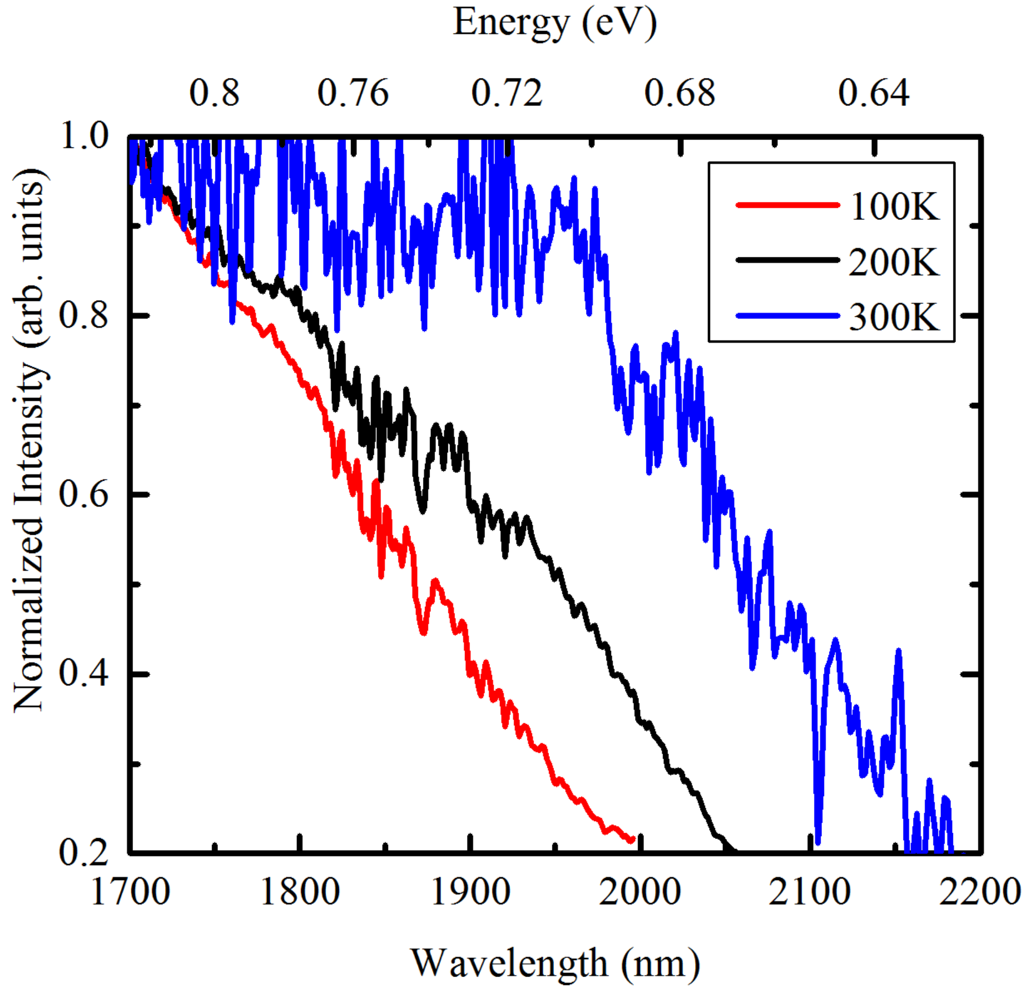

Figure 60: Temperature dependent spectral response for 7% Sn photoconductor.

Photodiode

A p-i-n diode operating in reverse bias could also work as photodetector. Therefore, 1st generation surface-emitting LEDs were used to characterize as photodetectors. The diode behavior was measured under reverse bias condition. The bias voltage will make the intrinsic GeSn layer to be fully depleted. Whenever the material collects photon and generates carriers, the carriers will be swept towards two electrodes by the electrical field to form photo current. Due to the intrinsic layer of the GeSn layer, carrier generated from the photon injection could be collected by the electrode. This could help us determine the direct band gap for the GeSn

material. 6% and 8% Sn composition p-i-n LED were reversely biased. Spectral response was measured. In this result, the cutoff edges were around 1940 nm and 2040 nm for 6% and 8% Sn samples, respectively, shown in Figure 61, which matches the emission peak of the LED device.

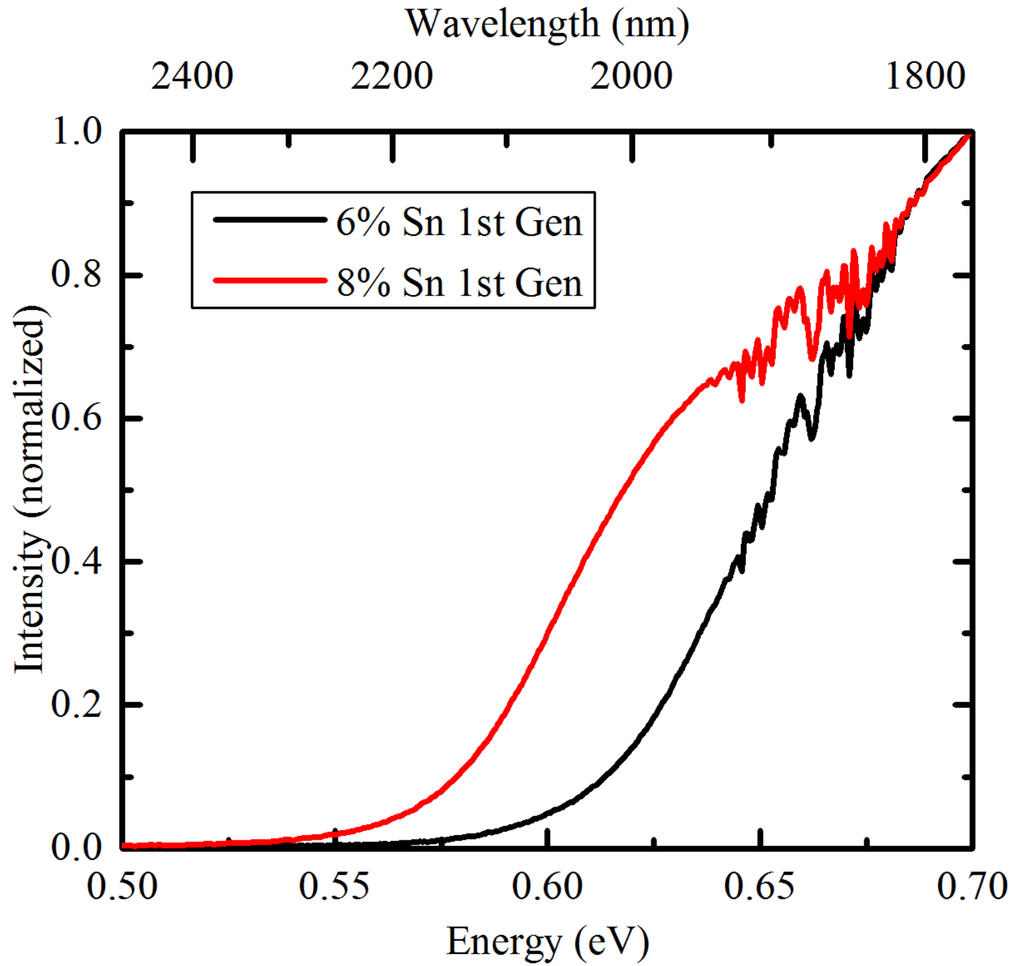

Figure 61: Spectral response for p-i-n photodiode with different Sn composition.

Chapter 6: Conclusion and Future Work

CVD grown GeSn p-i-n DHS structure has been characterized using XRD and PL. The peak position of the XRD rocking curve confirmed the Sn composition in GeSn layer. Compress strain was formed due to the lattice mismatch between Ge buffer and GeSn layer. Room temperature PL intensity showed the structure has the emission peak positions of 1940 nm and 2040 nm under photon injection corresponding to the band gap of 0.639eV and 0.608eV for GeSn layer with respectively 6% and 8% Sn. Thereafter, the grown samples had been fabricated into LED devices characterized at room temperature. From IV measurement, rectify behavior showed the device was working properly as a diode. EL spectrum at room temperature matches the profile of PL spectrum. This agreement indicates the emission spectra were generated by either light injection or electrical injection. GeSn active layer played a major role in the light emission. Peak positions reflect the band gap energy of the GeSn layer. The result agreed with the band gap for given Sn composition. Increasing Sn composition in GeSn layer would result in a band gap shrinking.

GeSn LED devices were fabricated into developed design for improving performance. Second generation devices would serve for high current injection. Also, it has the capacity for later cryogenic characterization. Optical power and emission intensity were observed using EL and optical power measurement. The noticeable heating effect was affected to the optical power measurement. TE cooler was able to control the temperature at a certain level. Third generation devices serve the purpose of improving optical power by uniform the current uniformity of the device. However, due to the current spreading through the device, the current intensity was dropped. Consequence, emission intensity and optical power were therefore lower than the first generation device. GeSn edge-emitting device were demonstrated which needs further investigation.

GeSn based optoelectronics could also serve for photo detection. Photoconductor with Sn composition of 0.9%, 3.2%, and 7% were fabricated. Due to the band offset of the hertrojunction between Ge and GeSn, resistance for forward and reverse bias were different. Spectral response had clear cutoffs from the band energy position indicating the material's direct band gap level.

GeSn material has the strong potential for the optoelectronic devices for Si photonics. LED, photoconductor, and photodiode were fabricated and characterized. Light emission and detection were demonstrated and the band gap agreed throughout the experiments. In this case, EL spectrum did not show a clear direct and indirect band gap emission peak since they were overlapped and difficult to identify only at room temperature.

To demonstrate a photonic device with direct band gap for GeSn material, further investigation is needed. Several approaches could resolve this issue: relax GeSn film, incorporate higher Sn composition, and temperature dependent EL.

All of the devices fabricated here have compressive strain which could result the indirect band gap material. Large lattice constant buffer layer could be deposited first to relax or stretch the layer. However, this requires a high perfection in the material growth and caution structure design which needs more efforts of development.

For LED device, we could also cool the device down and observe its EL behavior under different temperature. Due to the indirect and direct band gap transition mechanism, raising temperature will help to observe the direct band gap emission, while a lower temperature would dominate the indirect band gap emission. Therefore, low temperature EL is preferred to separate the direct band gap transition from indirect band gap transition.

Finally, by simply increasing the current injection several orders higher would make the direct band gap transition dominating. Pulse current with high injection is preferred to eliminate the temperature effect.

In summary, the material and device characteristics demonstrate the great potential and versatility of the GeSn material for optoelectronics devices.

References

[1] D. Liang and J. E. Bowers, “Recent progress in lasers on silicon,” *Nat. Photonics*, vol. 4, no. 8, pp. 511–517, Jul. 2010.

[2] and K. P. Richard A. Soref, Joachim Schmidtchen, “Large single-mode rib waveguides in GeSi-Si and Si-on-SiO2,” *IEEE J. Quantum Electron.*, vol. 27, no. 8, pp. 1971–1974, 1991.

[3] S. Assefa, S. Shank, W. Green, M. Khater, E. Kiewra, C. Reinholm, S. Kamlapurkar, C. Schow, F. Horst, H. Pan, T. Topuria, P. Rice, D. M. Gill, J. Rosenberg, and T. Barwicz, “IBM Press Release , December 10 , 2012 IBM Press Release , December 10 , 2012,” in *IEEE International Electron Devices Meeting*, 2012.

[4] R. Soref, “Silicon-based optoelectronics,” *Proc. IEEE*, vol. 81, no. 12, pp. 1687–1993, 1993.

[5] Y. Vlasov, “Silicon integrated nanophotonics: road from scientific explorations to practical applications,” in *plenary talk CLEO, United States*, 2012.

[6] S. McNab, N. Moll, and Y. Vlasov, “Ultra-low loss photonic integrated circuit with membrane-type photonic crystal waveguides.,” *Opt. Express*, vol. 11, no. 22, pp. 2927–2939, 2003.

[7] B. Jalali and S. Fathpour, “Silicon photonics,” *J. Light. Technol.*, vol. 24, no. 12, pp. 4600–4615, Dec. 2004.

[8] M. A. Popov ć, T. Barwicz, M. R. Watts, P. T. Rakich, L. Socci, E. P. Ippen, F. X. Kärtner, and H. I. Smith, “Multistage high-order microring-resonator add-drop filters,” *Opt. Lett.*, vol. 31, no. 17, pp. 2571–2573, 2006.

[9] L. Liao, D. Samara-Rubio, M. Morse, A. Liu, and D. Hodge, “High speed silicon Mach-Zehnder modulator.,” *Opt. Express*, vol. 13, no. 8, pp. 3129–3135, 2005.

[10] V. Raghunathan, R. Shori, O. M. Stafsudd, and B. Jalali, “Nonlinear absorption in silicon and the prospects of mid-infrared silicon Raman lasers,” *Phys. Status Solidi Appl. Mater. Sci.*, vol. 203, no. 5, 2006.

[11] R. Soref, “Silicon-based silicon–germanium–tin heterostructure photonics,” *Philos. Trans. R. Soc. A Math. Phys. Eng. Sci.*, vol. 372, no. 2012, p. 20130113, 2014.

[12] R. Chen, S. Gupta, Y.-C. Huang, Y. Huo, C. W. Rudy, E. Sanchez, Y. Kim, T. I. Kamins, K. C. Saraswat, and J. S. Harris, “Demonstration of a Ge/GeSn/Ge quantum-well microdisk resonator on silicon: enabling high-quality Ge(Sn) materials for micro- and nanophotonics.,” *Nano Lett.*, vol. 14, no. 1, pp. 37–43, Jan. 2014.

[13] S. Gupta, V. Moroz, L. Smith, Q. Lu, and K. Saraswat, "7-nm FinFET CMOS Design Enabled by Stress Engineering Using Si, Ge, and Sn," *IEEE Trans. Electron Devices*, vol. 61, no. 5, pp. 1222–1230, 2014.

[14] M. Liu, G. Han, Y. Liu, and C. Zhang, "Undoped Ge0.92Sn0.08 Quantum Well PMOSFETs on (001), (011) and (111) Substrates with In Situ Si2H6 Passivation: High Hole Mobility and Dependence of Performance on Orientation," *2014 Symp. VLSI Technol. Dig. Tech. Pap.*, no. 001, pp. 6–7, 2014.

[15] G. Han, S. Su, C. Zhan, and Q. Zhou, "High-mobility germanium-tin (GeSn) p-channel MOSFETs featuring metallic source/drain and sub-370 C process modules," *Electron Devices Meet. (IEDM), 2011 IEEE Int.*, no. 2010, pp. 402–404, 2011.

[16] S. A. Ghetmiri, W. Du, J. Margetis, A. Mosleh, L. Cousar, B. R. Conley, L. Domulevicz, A. Nazzal, G. Sun, R. a. Soref, J. Tolle, B. Li, H. a. Naseem, and S.-Q. Yu, "Direct-bandgap GeSn grown on silicon with 2230 nm photoluminescence," *Appl. Phys. Lett.*, vol. 105, no. 15, p. 151109, Oct. 2014.

[17] W. Du, Y. Zhou, S. a. Ghetmiri, A. Mosleh, B. R. Conley, A. Nazzal, R. a. Soref, G. Sun, J. Tolle, J. Margetis, H. a. Naseem, and S.-Q. Yu, "Room-temperature electroluminescence from Ge/Ge1-xSnx/Ge diodes on Si substrates," *Appl. Phys. Lett.*, vol. 104, no. 24, p. 241110, Jun. 2014.

[18] H. H. Tseng, K. Y. Wu, H. Li, V. Mashanov, H. H. Cheng, G. Sun, and R. a. Soref, "Mid-infrared electroluminescence from a Ge/Ge0.922Sn0.078/Ge double heterostructure p-i-n diode on a Si substrate," *Appl. Phys. Lett.*, vol. 102, no. 18, p. 182106, 2013.

[19] F. Breu, S. Guggenbichler, and J. Wollmann, "Investigation of Light Absorption and Emission in Ge and GeSn Films Grown on Si Substrates," 2008.

[20] R. Roucka, J. Mathews, R. T. Beeler, J. Tolle, J. Kouvetakis, and J. Menéndez, "Direct gap electroluminescence from Si/Ge1−ySny p-i-n heterostructure diodes," *Appl. Phys. Lett.*, vol. 98, no. 6, p. 061109, 2011.

[21] X. Sun, J. Liu, L. C. Kimerling, and J. Michel, "Room-temperature direct bandgap electroluminesence from Ge-on-Si light-emitting diodes.," *Opt. Lett.*, vol. 34, no. 8, pp. 1198–200, Apr. 2009.

[22] M. Oehme, J. Werner, M. Gollhofer, M. Schmid, M. Kaschel, E. Kasper, and J. Schulze, "Room-temperature electroluminescence from GeSn light-emitting pin diodes on Si," *IEEE Photonics Technol. Lett.*, vol. 23, no. 23, pp. 1751–1753, Dec. 2011.

[23] J. P. Gupta, N. Bhargava, S. Kim, T. Adam, and J. Kolodzey, "Infrared electroluminescence from GeSn heterojunction diodes grown by molecular beam epitaxy," *Appl. Phys. Lett.*, vol. 102, no. 25, p. 251117, 2013.

[24] E. Kasper and M. Kittler, "Light from germanium tin heterostructures on silicon," *SPIE Proc.*, vol. 2006594, no. March 2012, 2013.

[25] M. Oehme, K. Kostecki, T. Arguirov, G. Mussler, K. Ye, M. Gollhofer, M. Schmid, M. Kaschel, R. A. Korner, M. Kittler, D. Buca, E. Kasper, and J. Schulze, "GeSn Heterojunction LEDs on Si Substrates," *IEEE Photonics Technol. Lett.*, vol. 26, no. 2, pp. 187–189, 2014.

[26] B. R. Conley, A. Mosleh, S. A. Ghetmiri, W. Du, R. a Soref, G. Sun, J. Margetis, J. Tolle, H. a Naseem, and S.-Q. Yu, "Temperature dependent spectral response and detectivity of GeSn photoconductors on silicon for short wave infrared detection.," *Opt. Express*, vol. 22, no. 13, pp. 15639–52, Jun. 2014.

[27] M. Oehme, K. Kostecki, K. Ye, and S. Bechler, "GeSn-on-Si normal incidence photodetectors with bandwidths more than 40 GHz," *Opt. Express*, vol. 22, no. 1, pp. 6400–6405, 2014.

[28] D. Zhang, C. Xue, B. Cheng, S. Su, Z. Liu, X. Zhang, G. Zhang, C. Li, and Q. Wang, "High-responsivity GeSn short-wave infrared p-i-n photodetectors," *Appl. Phys. Lett.*, vol. 102, no. 14, p. 141111, 2013.

[29] B. Cheng, D. Zhang, S. Su, and X. Zhang, "GeSn near infrared photodetectors," *Asia …*, no. 001, pp. 5–7, 2013.

[30] S. Su, B. Cheng, C. Xue, W. Wang, and Q. Cao, "GeSn pin photodetector for all telecommunication bands detection," *Opt. …*, vol. 19, no. 7, pp. 6400–5, Mar. 2011.

[31] J. Werner, M. Oehme, M. Schmid, M. Kaschel, a. Schirmer, E. Kasper, and J. Schulze, "Germanium-tin p-i-n photodetectors integrated on silicon grown by molecular beam epitaxy," *Appl. Phys. Lett.*, vol. 98, no. 6, p. 061108, 2011.

[32] a Gassenq, F. Gencarelli, J. Van Campenhout, Y. Shimura, R. Loo, G. Narcy, B. Vincent, and G. Roelkens, "GeSn/Ge heterostructure short-wave infrared photodetectors on silicon.," *Opt. Express*, vol. 20, no. 25, pp. 27297–303, Dec. 2012.

[33] J. Mathews, R. Roucka, J. Xie, S.-Q. Yu, J. Menéndez, and J. Kouvetakis, "Extended performance GeSn/Si(100) p-i-n photodetectors for full spectral range telecommunication applications," *Appl. Phys. Lett.*, vol. 95, no. 13, p. 133506, 2009.

[34] N. Gayraud, Ł. W. Kornaszewski, J. M. Stone, J. C. Knight, D. T. Reid, D. P. Hand, and W. N. MacPherson, "Mid-infrared gas sensing using a photonic bandgap fiber," *Appl. Opt.*, vol. 47, no. 9, p. 1269, Mar. 2008.

[35] P. Werle, F. Slemr, K. Maurer, R. Kormann, R. Mücke, and B. Jänker, "Near- and mid-infrared laser-optical sensors for gas analysis," *Opt. Lasers Eng.*, vol. 37, no. 2–3, pp. 101–114, Feb. 2002.

[36] R. Soref, “The past, present, and future of silicon photonics,” *Sel. Top. Quantum Electron. IEEE J.*, vol. 12, no. 6, pp. 1678–1687, 2006.

[37] W. M. Green, M. J. Rooks, L. Sekaric, and Y. a. Vlasov, “Ultra-compact, low RF power, 10 Gb/s silicon Mach-Zehnder modulator,” *Opt. Express*, vol. 15, no. 25, p. 17106, 2007.

[38] R. E. Camacho-Aguilera, Y. Cai, N. Patel, J. T. Bessette, M. Romagnoli, L. C. Kimerling, and J. Michel, “An electrically pumped germanium laser.,” *Opt. Express*, vol. 20, no. 10, pp. 11316–20, May 2012.

[39] A. W. Fang, H. Park, O. Cohen, R. Jones, M. J. Paniccia, and J. E. Bowers, “Electrically pumped hybrid AlGaInAs-silicon evanescent laser,” *Opt. Express*, vol. 14, no. 20, p. 9203, 2006.

[40] P. Moontragoon, Z. Ikonić, and P. Harrison, “Band structure calculations of Si–Ge–Sn alloys: achieving direct band gap materials,” *Semicond. Sci. Technol.*, vol. 22, no. 7, pp. 742–748, Jul. 2007.

[41] S. A. Ghetmiri, W. Du, B. R. Conley, A. Mosleh, A. Nazzal, G. Sun, R. a. Soref, J. Margetis, J. Tolle, H. a. Naseem, and S.-Q. Yu, “Shortwave-infrared photoluminescence from Ge1−xSnx thin films on silicon,” *J. Vac. Sci. Technol. B, Nanotechnol. Microelectron. Mater. Process. Meas. Phenom.*, vol. 32, no. 6, p. 060601, Nov. 2014.

[42] L. M. Giovane, H.-C. Luan, A. M. Agarwal, and L. C. Kimerling, “Correlation between leakage current density and threading dislocation density in SiGe p-i-n diodes grown on relaxed graded buffer layers,” *Appl. Phys. Lett.*, vol. 78, no. 4, p. 541, 2001.

[43] L. M. Giovane, H.-C. Luan, A. M. Agarwal, and L. C. Kimerling, “Correlation between leakage current density and threading dislocation density in SiGe p-i-n diodes grown on relaxed graded buffer layers,” *Appl. Phys. Lett.*, vol. 78, no. 4, p. 541, 2001.

[44] E. F. Schubert, *Light-Emitting Diodes - 2nd Edition*. Cambridge University Press, 2006.

Appendix A: Description of Research for Popular Publication

Low Cost Light-emitting Devices Enables High Speed Communication to Home

Communication is necessary for almost every individual nowadays. Electronic devices have enabled people share and exchange information worldwide within a blink. There are dramatic needs to develop cost-effective, fast data transfer devices for communications. Especially, people are demanding higher speed communication for their living place. Google has launched the first project of 1 Gb/s internet for households using fiber based communication. One major bottleneck for the current fiber communication is the photonic integrated circuits. Si photonics for integrated circuits is almost mature for commercial purpose except the efficient light-emitting devices. In such circumference, efficient light-emitting devices on Si could solve this issue.

Recent researches have proved that a new member of Si phonics material, named germanium tin (GeSn), to be an excellent candidate for the purpose. The material could be easily grown on Si since the element, germanium and tin, are under the same group column with Si in periodic table. As a result, low cost and robust optoelectronic devices on Si would enable PIC applications in a cheaper and better manner.

Current research has reached to develop such devices to be commercially available. Dr. Shui-Qing Yu and Mr. Yiyin Zhou in University of Arkansas believe that they have found their path. Low cost LEDs have been demonstrated at room temperature with variety to emission band. The material was grown by commercial available RPCVD on 8-inch wafers. The conventional fabrication process was used to form bipolar n-i-p devices. The LED emission

spectrum was ranged from near to mid infrared with different Sn composition. The LED was bonded into standard chip carrier enables low temperature characterization.

Having a robust fabrication process, their next goal is to improve the device efficiency. Efficiency is significant for the LED. Eventually, they are going to approach GeSn based laser for Si photonics applications, which is the ultimate solution for the communication technology.

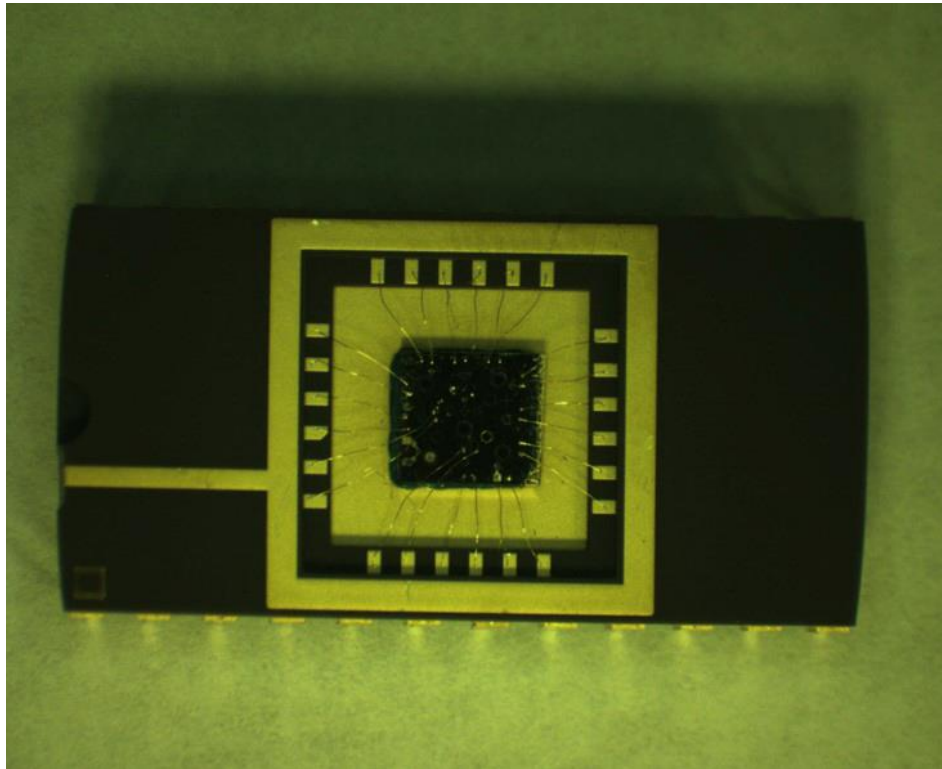

Figure 62: Optical Image for LEDs bonded on a chip carrier.

Appendix B: Executive Summary of Newly Created Intellectual Property

The following list of new intellectual property items were created in the course of this research project and should be considered from both a patent and commercialization perspective.

1. Ge/GeSn/Ge DHS p-i-n diode on Si
2. A fabrication process for GeSn based LEDs

Appendix C: Potential Patent and Commercialization Aspects of Listed Intellectual Property Items

C.1 Patentability of Intellectual Property (Could Each Item be Patented)

The two items listed were considered first from the perspective of whether or not the item could be patented.

1. The new Ge/GeSn/Ge p-i-n LED can be patented. With the new material GeSn as active layer, surface emitting LED could be fabricated at low cost.
2. The method of fabricating GeSn LED can be patented. The process is low cost with high yield for GeSn LED fabrication.

C.2 Commercialization Prospects (Should Each Item Be Patented)

The two items listed were then considered from the perspective of whether or not the item should be patented.

1. The Ge/GeSn/Ge p-i-n LED could be fabricated as low cost LED for near and mid infrared applications. However, the device was not optimized with enough efficiency for commercialization. Therefore, the design is too simple and is not worth to be patented.
2. The fabrication process is a low cost, robust process which could deliver large volume of LED devices. However, due to the device performance is not fully investigated, further development is needed. Therefore, the process is not worth to be patented.

C.3 Possible Prior Disclosure of IP

The following items were discussed in a public forum or have published information that could impact the patentability of the listed IP.

1. This design has been openly disclosed at IEEE Photonic Conference, San Diego, 2014.
2. This fabrication process has been openly disclosed at IEEE Photonic Conference, San Diego, 2014.

Appendix D: Broader Impact of Research

D.1 Applicability of Research Methods to Other Problems

The basic philosophy of this thesis research is applicable for other light-emitting device study. From material to device characterization, the method systematically studied the material as well as device quality for a semiconductor with both indirect and direct band gap transition.

D.2 Impact of Research Results on U.S. and Global Society

This work has first demonstrated the 10% Sn electroluminescence from GeSn based LED. The direct band gap transition was confirmed. This work has paved the path of GeSn based optoelectronic devices for Si photonics application. And the impact could further reach to the development for GeSn based laser on Si, which could largely reduce the cost of photonic integration on Si. Eventually, the optoelectronic IC may dominate the market.

D.3 Impact of Research Results on the Environment

As long as the optoelectronic IC dominate the electronic devices. The energy consumption of data transmission would decreased in a considerable amount.

Appendix E: Microsoft Project for MS MicroEP Degree Plan

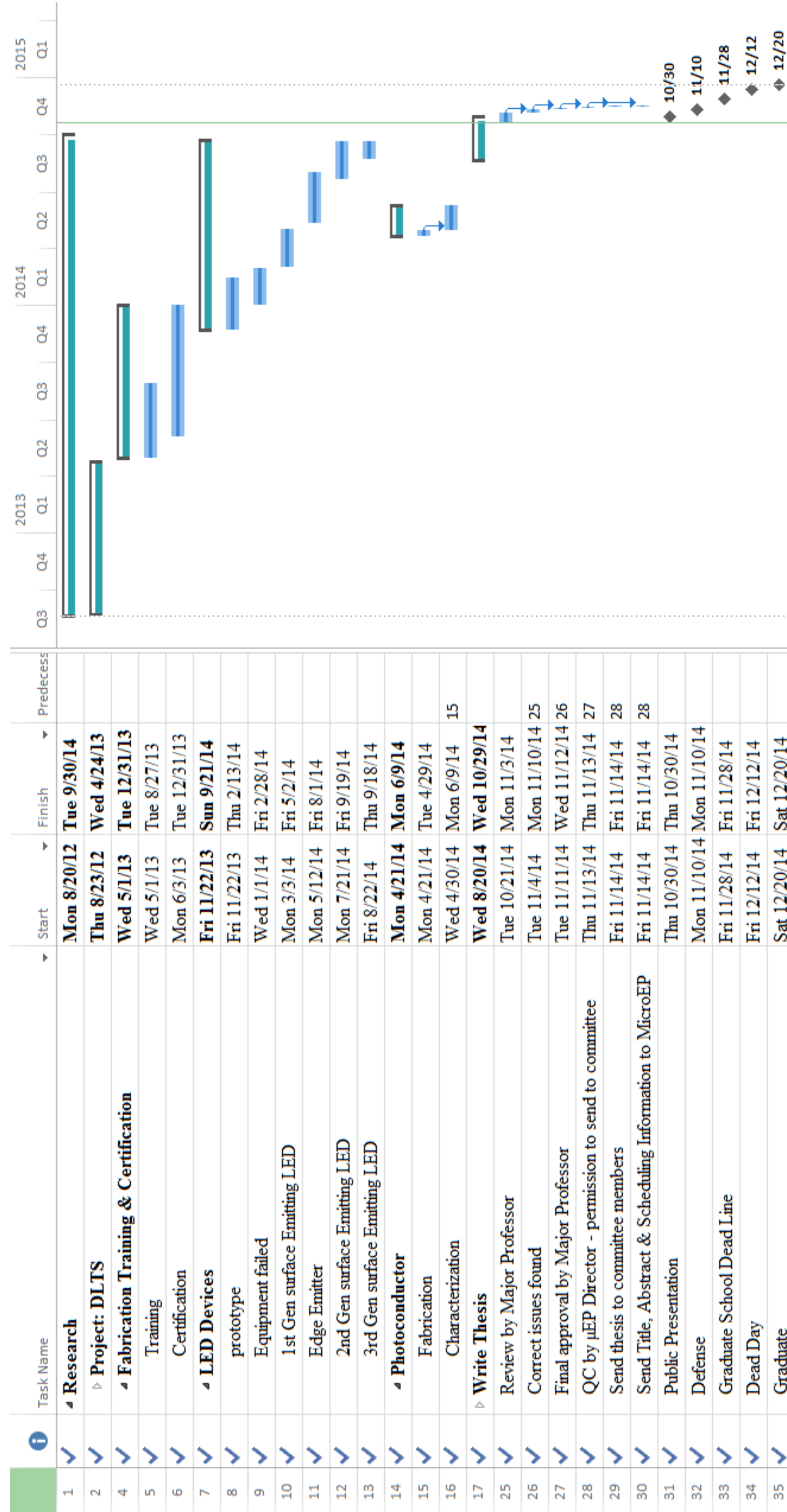

#	Task Name	Start	Finish	Predecessors
1	**Research**	**Mon 8/20/12**	**Tue 9/30/14**	
2	**Project: DLTS**	**Thu 8/23/12**	**Wed 4/24/13**	
4	**Fabrication Training & Certification**	**Wed 5/1/13**	**Tue 12/31/13**	
5	Training	Wed 5/1/13	Tue 8/27/13	
6	Certification	Mon 6/3/13	Tue 12/31/13	
7	**LED Devices**	**Fri 11/22/13**	**Sun 9/21/14**	
8	prototype	Fri 11/22/13	Thu 2/13/14	
9	Equipment failed	Wed 1/1/14	Fri 2/28/14	
10	1st Gen surface Emitting LED	Mon 3/3/14	Fri 5/2/14	
11	Edge Emitter	Mon 5/12/14	Fri 8/1/14	
12	2nd Gen surface Emitting LED	Mon 7/21/14	Fri 9/19/14	
13	3rd Gen surface Emitting LED	Fri 8/22/14	Thu 9/18/14	
14	**Photoconductor**	**Mon 4/21/14**	**Mon 6/9/14**	
15	Fabrication	Mon 4/21/14	Tue 4/29/14	
16	Characterization	Wed 4/30/14	Mon 6/9/14	15
17	**Write Thesis**	**Wed 8/20/14**	**Wed 10/29/14**	
25	Review by Major Professor	Tue 10/21/14	Mon 11/3/14	
26	Correct issues found	Tue 11/4/14	Mon 11/10/14	25
27	Final approval by Major Professor	Tue 11/11/14	Wed 11/12/14	26
28	QC by µEP Director - permission to send to committee	Thu 11/13/14	Thu 11/13/14	27
29	Send thesis to committee members	Fri 11/14/14	Fri 11/14/14	28
30	Send Title, Abstract & Scheduling Information to MicroEP	Fri 11/14/14	Fri 11/14/14	28
31	Public Presentation	Thu 10/30/14	Thu 10/30/14	
32	Defense	Mon 11/10/14	Mon 11/10/14	
33	Graduate School Dead Line	Fri 11/28/14	Fri 11/28/14	
34	Dead Day	Fri 12/12/14	Fri 12/12/14	
35	Graduate	Sat 12/20/14	Sat 12/20/14	

Appendix F: Identification of All Software Used in Research and Thesis Generation

Computer #1:
    Model Number: Lenovo Y400
    Serial Number: YB00433081
    Location: personal labtop
    Owner: Yiyin Zhou
Software #1:
    Name: Microsoft Office 2013
    Purchased by: Yiyin Zhou
Software #2:
    Name: OriginPro 9.1
    Purchased by: Yiyin Zhou
Software #3:
    Name: Microsoft Project 2010
    Purchased by: MSDN Academy Alliance through Engineering
Software #4:
    Name: Lumerical Mode Solution
    Purchased by: IEEE Photonics Conference, Workshop on Si Photonics

Computer #2:
    Model Number: Dell Vostro A860
    Serial Number: 52M6XK1
    Location: ENRC #2933
    Owner: Dr. Shui-Qing Yu
Software #1:
    Name: Omnic
    Purchased by: Dr. Shui-Qing Yu

Computer #3:
    Computer Name: ELEG-R3920W01
    Location: ENRC #2933
    Owner: Dr. Shui-Qing Yu
Software #1:
    Name: RSoft Photonic CAD Suite
    Purchased by: Dr. Shui-Qing Yu
Software #2:
    Name: MATLAB
    Purchased by: Dr. Shui-Qing Yu

Appendix G: All Publications Published, Submitted and Planned

G.1. Journals:

[1]. W. Du, **Y. Zhou**, S.A. Ghetmiri, A. Mosleh, B.R. Conley, A. Nazzal, R.A. Soref, G. Sun, J. Tolle, J. Margetis, H.A. Naseem, and S.-Q. Yu, "Room-temperature electroluminescence from Ge/Ge1-xSnx/Ge double heterostructure LEDs on Si substrates via CVD," *Appl. Phys. Lett.*, vol. 104, pp. 241110 (2014)

G.2. Conferences:

[1]. **Y. Zhou**, W.Du, S.A. Ghetmiri, A. Mosleh, A. Nazzal, R.A Soref, G. Sun, J. Margetis, J. Tolle, H.A. Naseem, and S.-Q. Yu, "Room-temperature electroluminescence from Ge/Ge0.92Sn0.08/Ge double heterostructure LED on Si," *IEEE Photonics Conference*, San Diego (2014).

[2]. **Y. Zhou**, S.A. Ghetmiri, A. Mosleh, B.R. Conley, H.A. Naseem, S.-Q. Yu, "Room temperature electroluminescence of Ge/Ge1-xSnx/Ge p-i-n double heterojunction light-emitting diodes", *Arkansas ASSET II NSF EPSCoR project review meeting*, Little Rock, AR (2014).

[3]. B.R. Conley, **Y. Zhou**, A. Mosleh, S.A. Ghetmiri, W. Du, R.A Soref, G. Sun, J. Margetis, J. Tolle, H.A. Naseem, and S.-Q. Yu, "Infrared spectral response of a GeSn p-i-n photodiode on Si", *the 11th International Conference on Group IV Photonics*, Paris (2014).

[4]. B.R. Conley, A. Mosleh, S.A. Ghetmiri, **Y. Zhou**, H. Naseem and S.-Q. Yu, "Characterization of GeSn for Si-based optoelectronic devices", *Arkansas ASSET II NSF EPSCoR project review meeting*, Little Rock, AR (2013)

Appendix H: First Generation Surface Emitting LED Fabrication Traveler

Traveler, NIP Surface Emitting LED

01422
01423
CTR1005

Fab Lot # CTR1001

Start Date:
Due Date:
Mask Set: PHOTODETECTOR Mask
Purpose: Surface Emitting LED process with small surface area (PHOTODETECTOR Mask)
Lot#: C(Conventional surface emitting LED), Top emitting, RIE eching, 1(first attempt), 001(Round number)

Lot #	Wafer #	Growth #	Description
01422	ASM1005-NIP-Z90A13	CVD	1 cm^2 9% (50 nm)Ge/(200 nm)Ge0.92Sn0.08 /(700 nm)Ge/Si
01423	ASM1006-NIP-Z100A13	CVD	1 cm^2 10% (50 nm)Ge/(200 nm)Ge0.92Sn0.06 /(700 nm)Ge/Si

OP/LINK	DESCRIPTION	PARAMETER	ESTIMATED TIME
0	Sample Pre-clean		0.5 hour
2	Photolithography	PHOTODETECTOR Mask, Mesa	1 hour
3	Wet Etch		1 hour
4	Photoresist Remove		0.5 hour
5	Photolithography	Oxide Opening	2 hour
6	Oxide Etch		0.5 hour
7	Metal Deposition	Metal contacts	2 hour
8	Lift off		hour
9	Photolithography	Oxide Opening	2 hour
10	Oxide Etch		0.5 hour
11	Metal Deposition	Metal contacts	2 hour
12	Lift off		hour
			Total: 13 hours

SAMPLE PRECLEAN				
Date/ Time		**Solvent Clean** ☐ Solvent bench ☐ Sonicator	☐ Acetone sonication for5 min ☐ IPA sonication for5 min ☐ IPA rinse ☐ Nitrogen dry	

PHOTOLITHOGRAPHY				
Date/ Time	2.1 2.2	**Preparation** ☐ Wet bench ☐ Hot plate **PR Apply** ☐ Spinner (right)	☐ Prepare MF CD-26 ☐ Set hot plate Temp. @ **100°C** wait for 10 min ☐ Thermometer Verify Temperature @ ________ ☐ Check Recipe 4 4000 rpm 30sec ☐ Small chuck ☐ Clean the side and bottom ☐ HMDS ☐ Apply AZ4110 ☐ Run recipe 4 ☐ Bottom & side cleaning after using	
	2.3	**Soft baking** ☐ Hot plate	☐ 100 °C / 120s	
	2.4	☐ MJB 3 Mask Aligner	☐ Light Intensity: ____________ ☐ PHOTODETECTOR Mask/ Mesa ☐ Exposure time used(7s @LI=6.4): ___________ ☐ Develop 30s	
	2.5	☐ **Post baking** ☐ Hot plate	☐ 105 °C /2min30sec	
	2.6	**Descum** ☐ Asher	☐ Recipe: **1 minute** run time Power: 100 Watts O_2 Gas Flow: 200 sccm	

	2.7	☐ **DEKTAK**	PR thickness~1.55um Thickness with PR: Dummy 1: ____________________________(um) Dummy 2: ____________________________(um) Dummy 3: ____________________________(um) Dummy 4: ____________________________(um) 01422: ____________________________(um) 01423: ____________________________(um) 01419: ____________________________(um)	
WET ETCHING				
Date/ Time	3.1	**Preparatiion** ☐ Acid bench	Prepare Solution HCL:H2O2:H2O=1:1:20 Set for 30 min	
	3.2	**Etching**	Target Thickness: 0. 5 um +PR Time:____3min____________ Thickness:______________ Rate:___________________ Time:_____2min___________ Thickness:_______________ Rate:___________________ Time:________________ Thickness:_______________ Rate:___________________ Time:________________ Thickness:_______________ Rate:___________________ Time:________________ Thickness:_______________ Rate:___________________ Time:________________ Thickness:_______________ Rate:___________________	Rate: 100 nm/min

Photoresist Removal				
Date/ Time	4.1	**Solvent Clean** ☐ Solvent bench	☐ PRS 1000 for 10min ☐ DI Water Rinse ☐ Nitrogen dry	
	4.2	**Descum** ☐ Asher	☐ Recipe: **1 minute** run time Power: 100 Watts O_2 Gas Flow: 200 sccm	200W 10min if PR stays
	4.3	**Etch depth** ☐ Dektak	Target 500 nm Thickness without PR: 01422: ______________________________(nm) 01423: ______________________________(nm)	

Neg. Photolithography 1				
Date/ Time	5.1 5.2	**Preparation** ☐ Solvent bench ☐ Hot plate **PR Apply** ☐ Spinner	☐ Prepare MF CD-26 ☐ Set hot plate @95°C&105°C for 10 min ☐ Thermometer Verify Temperature @ ________ ☐ Check Recipe 4 4000 rpm ☐ Small chuck ☐ Clean the side and bottom ☐ HMDS ☐ Apply AZ 5214 ☐ Run recipe 4 ☐ Bottom & side cleaning after using	
	5.3	**Soft baking** ☐ Hot plate ☐ Dektak	☐ 95°C / 60sec Thickness of resist:______________ (Target 2.2μm) ☐ Remove Edge bead	
	5.4	☐ MJB 3 Mask Aligner	☐ Light Intensity: ____________ ☐ Photodetector Mask/ Inner Contact ☐ Exposure time used(6s for LI 6.4): ___________	
	5.5	☐ **POST BAKING** ☐ Hot plate	☐ 105 °C /2min30sec	

	5.6	☐ MJB 3 Mask Aligner	☐ Flood exposure ☐ Exposure time used: _______________	30s@6.4
	5.7	**Develop** ☐ Solvent bench	MF CD 26 developer Temperature: _________ °C Volume: _____________mL Develop time(40s) LOT0001: ____________________________(sec) Check Figure	
	5.8	**Descum** ☐ Asher	☐ Recipe: **1min** run time Power: 100 Watts O_2 Gas Flow: 200 sccm	
Oxide Etch				
Date/Time	6.1 6.2	**Native oxide etching** ☐ Acid Bench	BOE Reference Volume:200ml Temperature: _________ °C Water rinse first Time: 10 sec	

METAL DEPOSITION 2

Date/ Time	7	**Edward 306T** ☐ Pumping down ☐ Cr deposition ☐ Au deposition	 Pump down time:_____________ min Base pressure:_______________ Torr Reference value **Cr : 10 nm @ 0.1 nm /sec** Start current: _________________mA Midway Deposition rate: _____________________ nm/sec Pressure: _____________________Torr End current: __________________mA Thickness: _____________________ nm Reference value **Au : 200 nm @ 0.5 nm /sec** Start current:_________________mA Midway Deposition rate: _____________________ nm/sec Pressure_____________________Torr End current__________________mA Thickness:_____________________ nm	

LIFT OFF				
Date/ Time	8	**Solvent Clean** ☐ Solvent bench ☐ Sonicator	☐ Acetone blow out (NO SONICATION) ☐ Rinse ☐ Nitrogen dry	

Neg. Photolithography 2				
Date/ Time	9.1 9.2	**Preparation** ☐ Solvent bench ☐ Hot plate **PR Apply** ☐ Spinner	☐ Prepare MF CD-26 ☐ Set hot plate @95°C&105°C for 10 min ☐ Thermometer Verify Temperature @ _______ ☐ Check Recipe 4 4000 rpm ☐ Small chuck ☐ Clean the side and bottom ☐ HMDS ☐ Apply AZ 5214 ☐ Run recipe 4 ☐ Bottom & side cleaning after using	
	9.3	**Soft baking** ☐ Hot plate ☐ Dektak	☐ 95°C / 60 sec Thickness of resist:_____________ (Target 2.2µm) ☐ Remove Edge bead	

	9.4	☐ MJB 3 Mask Aligner	☐ Light Intensity: ___________ ☐ Photodetector Mask/ Outer contact ☐ Exposure time used(6 s for LI 6.4): __________	
	9.5	☐ **POST BAKING** ☐ Hot plate	☐ 105 °C /2min30sec	
	9.6	☐ MJB 3 Mask Aligner	☐ Flood exposure ☐ Exposure time used: ______________	30s@6.4
	9.7	**Develop** ☐ Solvent bench	MF CD 26 developer Temperature: _________ °C Volume: _____________mL Develop time(40s) LOT0001: ____________________________(sec) Check Figure	
	9.8	**Descum** ☐ Asher	☐ Recipe: **1min** run time Power: 100 Watts O_2 Gas Flow: 200 sccm	
Oxide Etch				
Date/ Time	10.1 10.2	**SiO2 cleaning** ☐ Acid Bench ☐ Microscope	BOE Reference Volume:200ml Temperature: _________ °C Water rinse first Time: 15 sec Was the opened SiO2 area etched? ☐ Yes ☐ If no, rinse water, then etch and check again	

METAL DEPOSITION 2

<table>
<tr><td>Date/ Time</td><td>11</td><td>Edward 306T
□ Pumping down

□ Cr deposition

□ Au deposition</td><td>
Pump down time:_____________ min
Base pressure:_______________ Torr
Reference value <u>Cr : 10 nm @ 0.1 nm /sec</u>
Start current: _________________mA
Midway Deposition rate:
_____________________ nm/sec
Pressure: _____________________Torr
End current: __________________mA
Thickness: _____________________ nm

Reference value <u>Au : 200 nm @ 0.5 nm /sec</u>
Start current:_________________mA
Midway Deposition rate:
_____________________ nm/sec
Pressure_____________________Torr
End current__________________mA
Thickness:_____________________ nm</td><td></td></tr>
</table>

<table>
<tr><td colspan="5">LIFT OFF</td></tr>
<tr><td>Date/ Time</td><td>12</td><td>Solvent Clean
□ Solvent bench
□ Sonicator</td><td>☐ Acetone blow out (NO SONICATION)
☐ Rinse ☐ Nitrogen dry</td><td></td></tr>
</table>

Completed on:
Performed by: